UNIVERSITY OF OXFORD

Adjustment of an oceanic circumpolar current on different timescales

Kate Maurer-Song

Wadham College

University of Oxford

A thesis presented for the degree of

Doctor of Philosophy

Trinity 2023

할머니, 할아버지. 요새 한국 어 배울 시간 있어요.

Acknowledgements

My supervisors–David Marshall and James Maddison–warrant the biggest thanks for their guidance and support over the last four and five years respectively. Julian Mak provided help with the technical aspects of GEOMETRIC. Jorge Garcia-Franco's support with day-to-day DPhil worries and WhatsApp stickers was invaluable.

I would also like to thank Bina Maurer, Kay Song, Alex Glenn, Alice Ahearn, Emma Elley, Luka Nedic, and Thomas Li for their friendship (especially during the lockdowns). I also owe a lot of good times and my mental health to Wadham Chapel Choir, the Oxford Brookes Climbing Wall, Animal Crossing, and Fortnite. And while he may not know it, the existence of this thesis was made much smoother thanks to Awsten Knight. It may not seem directly related, but thank you to my mom for making me practice violin, piano, and tennis each for an hour every day.

Aaron Graham's presence in my life greatly improved my time at Oxford. His help with the frequency domain also didn't hurt.

Finally, I'd like to thank Charlemagne, Lilith, Stoffel, Milk, Possum, and May–my pet rats–for listening to chit chat, appreciating snacks, and providing fluffy company. Misha also provided supported through high school to the fourth year of my DPhil. Misha, Lilith, and Possum are greatly missed.

Abstract

The Antarctic Circumpolar Current (ACC) disproportionately and increasingly affects global anthropogenic climate change. Making observations in this region has been historically difficult so models play a vital role. Even though these models are often times highly idealised circumpolar channel configurations, they are used to understand processes and as test beds for the dynamics of this region. For instance, the equilibrated volume transport of this region is relatively insensitive to changes in the mean surface wind stress forcing: this is known as eddy saturation and is a key feature of ACC dynamics. Another active area of research centres around methods of eddy parameterisation. Eddy parameterisation is used to represent the effects of the mesoscale eddy field in coarser resolution models, such as those used for climate projections. GEOMETRIC is one such parameterisation that succeeds in capturing some unique aspects of circumpolar flow, such as eddy saturation.

This thesis investigates the response of a circumpolar current to wind stress perturbations across a variety of timescales. A hierarchy of models–from a dynamical system to an eddy resolving three-dimensional model–is used to understand the physical mechanisms behind the adjustment. In much of the literature, eddy saturation applies only to equilibrated transport and is controlled by baroclinic instability. However, it is known that relative to barotropic processes, baroclinic processes do not react rapidly to temporal wind stress changes, hence, the understanding of circumpolar current adjustment is not complete. This thesis details the responses across models in multiple dimensions and forcing frequency and concludes that both barotropic and baroclinic mechanisms affect the circumpolar response to wind stress changes. GEOMETRIC is used throughout this thesis and extends prior work completed on its ability to successfully capture eddy saturation. An array of models with growing complexity is used to "build up" the physics of a circumpolar current with each step of the hierarchy. In a dynamical system and two-dimensional model, resonant frequencies associated with baroclinic adjustment are identified. Three-dimensional models, both parameterised and eddying, suggest both barotropic and baroclinic mechanisms are at play in controlling the ACC. Furthermore, this thesis tests GEOMETRIC's ability to go beyond equilibrated timescales of circumpolar channel flow.

Table of Contents

List of Figures

List of Tables

1 | Introduction

Twenty to forty million years ago, modern day South America and Australia separated from the Antarctic continent, creating the Southern Ocean. This led to deep water cooling, glacial ice formation, and the isolation of the Antarctic continent, all of which continue to affect the present day climate (Livermore et al., 2005; Munday et al., 2015). With the anthropogenic changes of the modern day it is crucial to increase our understanding of the Southern Ocean and its main dynamical feature–the Antarctic Circumpolar Current (ACC). The ACC connects the three main ocean basins (Atlantic, Pacific, and Indian), thus serving as a global ocean telecommunication system. To add to this system, the ACC has a direct link to the atmosphere via exposed outcropping isopycnals at the sea surface towards the Antarctic continent. The Southern Ocean is therefore a major component of the global oceanic-atmospheric exchange of tracers–both anthropogenic and naturally occurring. For that reason, improving our understanding of the ACC's response to external forces will contribute to the global understanding of anthropogenic climate change. This thesis aims to characterise the response of an oceanic circumpolar current to external wind forces on a variety of timescales, with particular interest in better understanding the mechanisms associated with transient and equilibrated flow. These findings can be applied to the physics of the Antarctic Circumpolar Current.

1.1 Motivation

The Southern Ocean is historically difficult to observe directly. While observations have improved within the last half century, models are often used in the place of complete and reliable observations in order to understand the dynamics of the ACC (Rintoul et al., 2001; Park et al., 2019; Fox-Kemper et al., 2019). Models are particularly advantageous in understanding the change of the Southern Ocean when subject to external forces. For example, models can characterise the response of the Southern Ocean to changes in wind stress forcing over time. At least with the current sets of observational data, understanding the dynamical changes to the same degree is not feasible.

The Southern Ocean is largely driven by intense westerly winds. There is evidence suggesting that these winds are strengthening and potentially shifting southwards (Meredith et al., 2019). While some coarse resolution models predict that ACC transport and overturning is sensitive to wind stress changes, high resolution models widely refute this sensitivity claim (Rintoul et al., 2008). Analysis of high resolution models suggests that transport and overturning are insensitive to wind stress changes. This is known as "eddy saturation" and "eddy compensation" respectively, and both are not refuted by observational data (Morrison and Hogg, 2013). In a nutshell, high resolution eddy resolving models suggest that northward Ekman transport increases due to increasing winds, but is counteracted by a southward eddy overturning cell, which essentially cancels out any transport or overturning changes (Youngs et al., 2017). As the Southern Ocean has a disproportionate effect on the Earth's climate, understanding the degree of insensitivity of ACC transport is crucial to our understanding of anthropogenic climate change.

Eddy saturation is usually modelled and analysed over equilibrated timescales (Munday et al., 2013; Mak et al., 2017). In fact, the standard definition of eddy saturation is the relative insensitivity of equilibrium thermal wind transport to the mean wind stress forcing (Straub, 1993). In plain English, the transport of the ACC does not change with wind stress magnitude over very long time periods. This time period can be on the order of thousands of years in some model cases (Allison et al., 2011). As is the case with atmospheric storm tracks, it is theorised that eddy saturation is a result of the growth and decay of baroclinicity and the growth and decay of the mesoscale eddy field (Ambaum and Novak, 2014). This can also be thought of as the balance between wind driven and baroclinic eddy transport (Sinha and Abernathey, 2016). It is also noted that these baroclinic processes associated with equilibrated eddy saturation do not take place instantaneously, as it takes time for the wind stress to influence the full depth of ACC circulation (Meredith and Hogg, 2006). In Meredith and Hogg (2006), eddy saturation is defined on significantly shorter timescales (on the order of years). They argue that eddy energy increases after wind stress magnitude increases. This leads to enhanced eddy diffusivity, which compensates for the increased wind stress input on non-equilibrated timescales.

The westerlies do however change with time. For example, the Southern Annular mode–a low-frequency atmospheric variability mode which comprises the westerlies–is only increasing with anthropogenic climate change (Swart and Fyfe, 2012). This increase leads to intensifying westerlies around the Antarctic continent. Even so, there is no evidence for much change in ACC thermal wind transport over this full period of time (Chidichimo et al., 2014). In fact, data from the 1960s through 1990s suggest no change in ACC transport (Rintoul et al., 2008). While there is evidence for non-zero ACC transport variability on interannual timescales (Meredith et al., 2004), the mechanisms controlling the dynamics at these timescales are not clear in the literature (Sinha and Abernathey, 2016). In particular, the literature on eddy saturation often does not account for the interaction between barotropic and baroclinic processes in controlling the ACC.

Capturing global eddy saturation in models is a significant challenge to the field. While high resolution models are adept at yielding eddy saturation, low resolution models are often not (Munday et al., 2013). When using low resolution models, the choice of parameterisation is crucial in achieving eddy saturation

(Mak et al., 2017). GEOMETRIC is one such parameterisation that shows emergent eddy saturation on equilibrated timescales (Marshall et al., 2017; Mak et al., 2018). Even so, there is a clear gap in the literature in understanding eddy saturation in low resolution models at non-equilibrated timescales. Eddy parameterisations often rely on mathematical techniques to capture baroclinic instability (Gent and McWilliams, 1990; Gent et al., 1995). It is consequentially not obvious how parameterisations behave at non-equilibrated timescales and with time-dependent wind stress magnitudes. Accurately representing eddy saturation is important to global climate models, but it is impractically expensive to always fully resolve the mesoscale eddy field. Hence, understanding the ACC's adjustment and response to winds at a wide range of unequilibrated timescales and model resolutions is an important area of research.

1.2 Thesis aims and outline

This thesis investigates the response of the circulation and stratification in a circumpolar channel to wind stress perturbations across a wide variety of timescales. This channel is ACC-like and is tuned accordingly. It is however important to note, this thesis is mainly a theoretical study of ACC-like models, rather than a thesis based on observations and accurate bathymetry. A hierarchy of models–from highly idealised to eddy resolving–is used to understand the physical mechanisms behind the response. The specific aims of this thesis are as follows:

1. To determine the mechanisms controlling the response of the circumpolar current to wind stress changes.
2. To compare and contrast the transient behaviour across model dimensions (dynamical system, two-dimensional, three-dimensional eddy parameterising, and three-dimensional eddy resolving) and understand the similarities

and differences.

3. To analyse the effects of variable wind stress on a circumpolar current using frequency analysis techniques, which are often not used in the field.

This thesis is structured as follows:

Chapter 2 provides a literature review on the essentials of Southern Ocean dynamics. This chapter begins with an overview on the large-scale dynamics in this region. This discussion focuses on how ACC transport is driven, overturning circulation, and the mesoscale eddy field. Eddy saturation is next introduced, with special attention given to the mathematics and the timescales. Climate implications and observational data and methods are also presented, but less rigour is needed in the context of this thesis. As this thesis provides a hierarchy of models, the literature on the techniques of modelling eddy saturation is discussed in detail, both in terms of eddy resolving and eddy parameterised configurations. Specifically, the Gent-McWilliams scheme (GM) and GEOMETRIC are presented in mathematical detail.

Chapter 3 focuses on the Massachusetts Institute of Technology general circulation model (MITgcm) and the methods behind the analysis. Both three-dimensional models are configured in MITgcm. Frequently used diagnostics (such as ACC transport) are discussed along with non-obvious analysis methods. Frequency analysis is often not used in the field, hence providing some mathematical detail is necessary to understand the analysis in this thesis.

Chapter 4 is dedicated to the first model in the hierarchy–the dynamical system. This model is parameterised by GEOMETRIC and in the steady state is eddy saturated. This model extends the work in Maddison et al. (2023).

In particular, the work on oscillatory wind stress is expanded upon. This model is solved both analytically (after linearisation) and numerically (with a multistep method), and both methods give reassuringly similar results. Results are discussed in both the time domain and the frequency domain, and an inherent resonant timescale is determined both through experimental results and analytically. This timescale of oscillation is then extended and given for a generalised density profile that varies with depth. The results from the dynamical system are attributed to baroclinic processes.

Chapter 5 details the next step in the hierarchy–the two-dimensional model. This model extends the configuration given in Mak et al. (2017) by allowing the wind stress to vary with time. Again, this model is parameterised by GEOMETRIC, but a standard GM case is also presented for comparison. Results widely agree with the results from the dynamical system. Again, baroclinic processes dominate in this configuration.

Chapter 6 investigates a low resolution eddy parameterised (GEOMETRIC) ACC-like channel. This configuration is similar to the configuration in Mak et al. (2018) but with the inclusion of the time-variable wind stress. The results in this chapter show evidence for both barotropic and baroclinic mechanisms. As in the lower dimensional models, there is an inherent oscillatory timescale associated with GEOMETRIC. This chapter also introduces an eddy resolving three-dimensional model. This model is an ACC-like channel with bathymetry at $\frac{1}{10}^{\circ}$ resolution. Wind perturbations are applied and analysed. Like in the parameterised configuration, there is evidence for both barotropic and baroclinic mechanisms. However, there are clear differences between the eddy parameterised and eddy resolving results. All models in the hierarchy are discussed together.

2 | Background

2.1 The Southern Ocean and its dynamics

The Southern Ocean is a complex system, driven by wind forced Ekman flows, mesoscale eddies, flow-topography interaction, air-sea-ice buoyancy exchange, interior dianeutral and diapycnal mixing, and shelf-slope processes (Naveira Garabato et al., 2014). The Southern Ocean's main dynamical feature–the Antarctic Circumpolar Current (ACC)–is a $25,000$ km long series of currents encircling the Antarctic continent. This region is a largely zonally unblocked band of open water, the geometry of which directly contributes to the unique dynamics and behaviour of the Southern Ocean (Toggweiler and Bjornsson, 2000).

Drake Passage is located between the tip of Chile and the Antarctic South Shetland Islands. This is the choke point of the Southern Ocean, as well as the nexus between the Pacific and Atlantic ocean basins. Drake Passage is an approximately 800 km wide and $3,400$ m deep (averaged) opening with a submerged ridge. This narrow opening constrains both the path and strength of the ACC and its bathymetry greatly influences deep water mixing (Meredith et al., 2011). Crucially, ACC volume transport is often measured at this point (Rintoul et al., 2001). Drake Passage is the most heavily monitored region of the ACC due to the practicality of its location. Drake Passage is the narrowest region of the ACC, so the full meridional extent is most easily monitored. Additionally, this is north of the most inhabited region of Antarctica. There are also no complications associated with subpolar or subtropical flows, as there are northern and southern boundaries (Meredith et al., 2011). As a result, there are many long-term monitoring projects for Drake Passage. Hydrographic data garnered during the International Southern Ocean Studies (ISOS) in the 1970s and 1980s derived a value for ACC transport in this region of 134 ± 15 Sv (where 1 Sv $= 10^6$ m^3) (Xu et al., 2020). While this figure and its standard deviation have been updated since, this is not far off from the current accepted value of 137 ± 7 Sv. ACC transport is discussed in more detail in later sections, but this highlights the importance of Drake Passage.

Because Drake Passage is zonally unblocked, there are no net east-west pressure gradients to balance the effects of Earth's rotation. In open regions there is no continental topography to support zonal pressure gradients, whereas in regions with continental obstructions, surface water can instead gather around continents. This means that warm upper ocean water cannot easily flow into or across the channel. This inhibits a mean meridional geostrophic flow, keeping Antarctica relatively isolated from the warmer surface waters from the equator, as poleward geostrophic transport can only occur at depth (Rintoul and Naveira Garabato, 2013).

This dynamics of this region are primarily driven by surface wind stress forcing. The strong eastward wind over the Southern Ocean, τ_s, imparts surface momentum into the ocean. This stress is balanced by bottom form stress, as conservation of momentum requires that momentum can only be added or removed by boundary effects. Bottom form stress comes from pressure gradients across bottom topographic features, and transfers momentum to the solid Earth and supplies a westward opposing force (Munk and Palmén, 1951). While the ACC inhibits mean meridional geostrophic flow, there is, however, a southward return flow below depths of about 2000 m associated with abyssal pressure gradients (Nikurashin and Vallis, 2012). This balances the wind driven equatorward Ekman flux driven by the westerlies. In terms of flow, this implies that equatorward transport is balanced by a deep geostrophic return flow (Zika et al., 2013). This leads to a system of overturning, which is known as meridional overturning circulation, which is discussed in greater detail in Section 2.1.3.

The associated surface wind and bottom form stresses are connected by an interior stress. In equilibrium, the momentum from the surface is vertically transferred to the solid Earth via interfacial form stress (Johnson and Bryden, 1989; Marshall et al., 2017; Constantinou and Hogg, 2019). Interfacial form stress arises from horizontal pressure gradients across density surfaces, as fluids in less dense layers push against fluid in more dense layers (Olbers, 1998; Marshall et al., 2017). Interfacial form stress is also known as eddy form stress, since the vertical structure of the eddy field is associated with the undulating neutral surfaces. (Poulsen et al., 2018). The mesoscale eddy field thus aids in transferring momentum between adjacent density layers. The mesoscale eddy field is discussed in Section 2.1.2.

2.1.1 The Antarctic Circumpolar Current

The ACC has a baroclinic volume transport of approximately 137 ± 7 Sv, making it Earth's largest ocean current (Meredith et al., 2019). However, transport, like most desirable data about the Southern Ocean, is difficult to directly measure. Transport can be split into baroclinic and barotropic components. The baroclinic transport–or (more usefully known as) thermal wind transport–is the integral of flow relative to the bottom according to thermal wind balance (Meredith et al., 2011). This can be measured using temperature and salinity profiles. When subject to wind stress changes, the thermal wind transport in the ACC is believed to be relatively insensitive to wind stress changes. This insensitivity is known as eddy saturation and is discussed at length in Section 2.1.4. Barotropic transport is measured from the "near bottom" velocity (Peña-Molino et al., 2014). Practically, this is the flow at the bottom multiplied by the depth of the water. Observations of the flow towards the seafloor are scarce and its strength is debated. Barotropic transport may account for up to 25% of total ACC volume transport, but this is an area of active research (Peña-Molino et al., 2014).

Beneath the surface Ekman layer, ACC dynamics are primarily driven by thermal wind balance so that,

$$\frac{\partial u_g}{\partial z} = \frac{g}{\rho_0 f}\frac{\partial \rho}{\partial y}, \tag{2.1}$$

$$\frac{\partial v_g}{\partial z} = -\frac{g}{\rho_0 f}\frac{\partial \rho}{\partial x}, \tag{2.2}$$

where (u_g, v_g) is the horizontal geostrophic velocity, g is the acceleration due to gravity, f is the Coriolis parameter, ρ_0 is a reference density, and ρ is the density (Vallis, 2006; Allison et al., 2010). Integrating thermal wind balance across the ACC leads to an expression for ACC thermal wind transport,

$$T_{ACC} \approx \frac{g}{\rho_0 |f_{ACC}|}\int_{-H}^{0} z(\rho_n - \rho_s)\mathrm{d}z, \tag{2.3}$$

which assumes $u = 0$ at $z = -H$, where H is the depth and $z = 0$ is the ocean surface. Here, the Coriolis parameter and reference density are constants, taken at a typical ACC latitude. The absolute value of the Coriolis parameter is taken, as Southern Hemisphere Coriolis parameters are negative. ρ_n and ρ_s are the densities along sloping boundaries to the north and south of Drake Passage respectively.

Thermal wind transport may also be approximated as the residual between total transport and bottom transport. This definition can provide a meaningful decomposition of the influence of thermal wind shear of the transport. To define thermal wind transport in this way, first total and bottom transports must be defined. Following on from Munday et al. (2015), the total ACC Transport is defined

$$T_{\mathrm{ACC}} = \iint \hat{\bar{u}}\,\mathrm{d}y\mathrm{d}z, \tag{2.4}$$

where $\overline{u}$ is the zonally averaged flow and the hat indicates a time average. The bottom transport is given by

$$T_{\mathrm{b}} = \iint \overline{\hat{u_b}} \mathrm{d}y \mathrm{d}z \tag{2.5}$$

where $\overline{\hat{u_b}}$ is zonally and time averaged flow at the bottom level (as stipulated by each model or observational data set specifically). In words, this is the bottom flow integrated through the full column of water. Thermal wind transport is then the difference between total and bottom transport, so that

$$\begin{aligned} T_{\mathrm{tw}} &= T_{\mathrm{ACC}} - T_{\mathrm{b}}, \\ &= \iint \left(\overline{\hat{u}} - \overline{\hat{u_b}} \right) \mathrm{d}y \mathrm{d}z. \end{aligned} \tag{2.6}$$

While this provides an approximation for thermal wind transport, it is important to note that this does not hold for an ageostrophic flow.

Besides wind stress forcing, there is also some influence from buoyancy forcing on the ACC. Buoyancy forcing plays a role in setting the structure of the Southern Ocean (Howard et al., 2015). The zonal transport of the ACC is linked to stratification, as prescribed by the thermal wind relationship. Since buoyancy forcing affects stratification, there are naturally some buoyancy-linked contributions to transport. Buoyancy forcing sets the surface north-south density gradient in this region. It is assumed that density surfaces outcrop south of the ACC (towards Antarctica). This implies that ρ_s is approximately constant with depth. Therefore, buoyancy forcing plays an implicit yet crucial role in setting ACC transport via Eq.(2.3). Buoyancy forcing is also influential in overturning, as meridional overturning relies on sinking and movement of dense water masses (Morrison et al., 2011).

Howard et al. (2015) compare the effects of wind and buoyancy forcing in an ACC-like model. This re-entrant channel model is a three-layer isopycnal model forced in two ways. Firstly, zonal flow is forced by a zonal and constant wind stress. Secondly, buoyancy forcing is used to drive an overturning circulation. In comparison to a strictly wind forced configuration, a buoyancy-only forced model exhibits lower eddy kinetic energy but higher zonal volume transport. The differences between the two forcing regimes also manifest in the depth averaged flow structure. When purely forced by surface wind, a single meandering jet interacts with topography, whereas in a purely buoyancy forced configuration, two smaller and nearly zonal jets appear and have far less interaction with topography. Overall, buoyancy forcing holds greater influence in inducing meridional circulation, as it is unable to directly inject momentum into the flow.

2.1.2 The mesoscale eddy field

The oceanic mesoscale eddy field is comprised of the time dependent vortices, spirals, cascades, and fronts throughout the ocean. Oceanic eddies are typically on length scales less than $100\ \mathrm{km}$ and last on timescales of several months. Mesoscale eddies often have different properties than the surrounding mean currents. This allows for the transport of tracers such as heat, carbon, and salinity. The mesoscale eddy field is very energetic and accounts for over half of the kinetic energy within the ocean (Wunsch, 2015). Eddies are most rife where there is the most instability. This also holds true in the atmosphere, where large scale eddies on the synoptic scale are linked with weather. In the ocean, this results in intense eddying along western boundaries of ocean basins and along the Southern Ocean (Williams and Follows, 2011). While ubiquitous throughout the global ocean, this thesis only considers the mesoscale eddy field in the Southern Ocean.

In the Southern Ocean, eddies are formed through baroclinic instability, the dynamical instability of slumping density gradients. This eddying is most intense along the ACC path (Meredith, 2016). Baroclinic instability gives the eddies a reservoir of potential energy which arises from the unstable exchange of fluid parcels (Eady, 1949). This unstable exchange lowers the centre of gravity of the fluid, which in turn leads to a loss of potential energy (Vallis, 2006). The generation of baroclinic instability and the growth of eddies is a cyclic relationship in both the atmospheric and oceanic cases. The generation of eddy energy through baroclinic instability balances the erosion of mean potential energy from the eddying (Ambaum and Novak, 2014).

The accurate representation of the mesoscale eddy field requires high resolution models. Models of such high resolution are computationally expensive, so parameterisations are often used to represent the mesoscale eddy field instead. Section 2.3 discusses eddy parameterisation in greater detail. Parameterisations can lead to spurious dynamics that are not evident in high resolution models or observed data. For instance, insufficiently high resolution or parameterised models may fail to show the regional variability of the mesoscale eddy field (Patara et al., 2016).

2.1.3 Overturning Circulation

The dynamics of the Antarctic Circumpolar Current are intrinsically linked to meridional overturning circulation (MOC), which stores and transports heat, freshwater, and carbon throughout the rest of the global ocean (Marshall and Speer, 2012). The key dynamics of this overturning circulation can be described by two counter-rotating meridional cells on a global scale. The upper cell is fed by North Atlantic waters and diapycnal upwelling. At intermediate depths, this flow is balanced by upwelling in the Southern Ocean, as induced by the westerly winds. This cell forms the North Atlantic Deep Water (NADW). The lower cell consists of dense water formed around the Antarctic continent, and forms the Antarctic Bottom Water (AABW) (Nikurashin and Vallis, 2012). In comparison to the upper cell, this cell is relatively unstratified. This water crosses isopycnals and upwells throughout the abyssal ocean, spilling northward and eventually recirculating into the Southern Ocean. At this stage of the MOC, the ACC dynamics play a crucial role in setting the depth of the isopycnals (Lumpkin and Speer, 2007).

The following summarises Nikurashin and Vallis (2012) to give more detail on the role of the ACC in overturning. There are three key areas of importance: (1) the circumpolar channel, (2) the isopycnal outcrop region in the Northern Hemisphere, and (3) the basin in between. As established, the circumpolar region is driven by wind and eddy-induced dynamics. In a purely wind driven configuration, waters upwell polewards of the geographical wind stress maximum and downwell equatorwards of this maximum. This clockwise wind driven overturning cell is known as the Deacon Cell. However, the mesoscale eddy field opposes this overturning through an anticlockwise eddy induced overturning cell. The interaction of these cells leads to residual circulation. The residual MOC has reduced sensitivity to wind stress changes. This insensitivity is known as eddy compensation (Abernathey et al., 2011). Assuming that this region is nearly adiabatic, the circulation is along the isopycnals, but not necessarily zero. It is within region (1) that the isopycnal depth is set. In the intermediary basin, the isopycnals are nearly flat. Hence, meridional flow associated with overturning only takes place at the western boundary, where friction can balance planetary vorticity changes. Continental blocking then causes subduction and westward flow in the deep ocean. When this zonal flow hits the western boundary, it then transforms into meridional flow. Isopycnal slopes grow with enhanced diapycnal mixing, which opposes wind driven circulation and upwelling. Additionally, reducing the surface winds results in a shallower upper cell and a larger abyssal cell that diffusively upwells in the low- and mid-latitudes. Figure 2.1 depicts the aforementioned principles of Southern Ocean dynamics and overturning.

Eddy compensation is the hypothesised insensitivity of the MOC to wind stress changes. This phenomenon is observed in some explicitly eddying models. However, when compared to eddy saturation, idealised models show that the overturning response is more sensitive to wind stress changes. For example, Bishop et al. (2016) analyse the response of the ACC and MOC to zonal wind stress in a high-resolution coupled oceanic-atmospheric simulation to zonal wind perturbations. Here it is found that increasing the surface wind stress by 50% leads to only a 6% change in zonal transport, but a 39% change in upper cell overturning. These specific values are model dependent, but the general sensitivity trends hold. This comparative sensitivity may be due to depth integration. Eddy saturation is based upon depth integrated diagnostics which can cover any local sensitivities, whereas eddy compensation is based upon a depth-dependent metric (Poulsen et al., 2018).

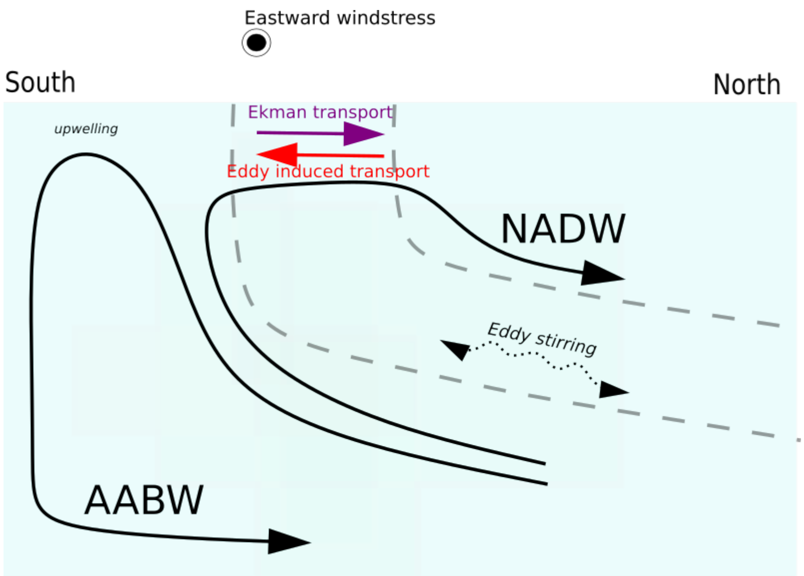

Figure 2.1: A schematic of overturning, with focus on processes in the Southern Ocean. An eastward wind stress blows across the ACC, which induces Ekman and eddy induced transport. Abbreviations are as follows: NADW- North Atlantic Deep Water; AABW- Antarctic Bottom Water.

2.1.4 Eddy saturation

Eddy saturation is the relative insensitivity of equilibrium thermal wind transport to wind stress forcing (Straub, 1993). The Southern Ocean is eddy saturated in many high resolution models and some parameterised models. While an eddy saturated Southern Ocean is still just a hypothesis, it is not contradicted by observations (Rintoul et al., 2008; Hogg et al., 2015). Since eddy saturation is directly linked to ACC transport, its physics are a key component in setting and understanding global stratification. Subsequently, eddy saturation is important in understanding climate projections, such as heat and carbon storage (Marshall et al., 2017).

When discussing eddy saturation, most literature is specifically referring to insensitivity of the thermal wind transport (Straub, 1993; Marshall et al., 2012;

Mak et al., 2017; Mak et al., 2018). This view of eddy saturation relies on the generation of eddies from baroclinic instability. Increasing the wind stress leads to increased vertical shear. Were this shear to steepen unabated, thermal wind transport would increase. However, as the shear steepens, the flow grows baroclinically unstable. This baroclinic instability results in mesoscale eddy generation, which require a reservoir of potential energy, which the increased shear provides. In other words, steepening isopycnals "feed" the mesoscale eddy field, which causes the isopycnals to slump, thus counteracting increasing thermal wind transport. This results in thermal wind transport insensitivity to increasing wind stress. The relationship between the mesoscale eddy field and thermal wind transport also applies to decreased wind stress. Decreased wind stress reduces the baroclinic instability, which in turn "starves" the mesoscale eddy field. This allows for thermal wind transport to re-approach equilibrium and maintain its insensitivity to wind stress. Baroclinic adjustment is usually studied in the context of equilibrated flow. Hence, eddy saturation refers to the insensitivity of equilibrated thermal wind (baroclinic) transport.

According to Marshall et al. (2017), eddy saturation is the product of three ingredients:

1. a zonal momentum budget,
2. a relationship between eddy form stress and eddy energy, and
3. an eddy energy budget.

Ingredient (1) balances wind stress (τ_s) against bottom form stress. The surface wind stress provides an eastward source of momentum, while the bottom form stress decelerates the abyssal flow. Bottom form stress decelerates the abyssal flow since high and low pressures form on either side of topographic barriers and Drake Passage. These two stresses are connected by eddy form stress (S), which, as discussed, is fuelled by eddies. There is additional vertical momentum transfer through residual overturning and the associated Coriolis forces. In equilibrium, this leads to a momentum balance equation,

$$\tau_s = S - \rho\,|f|\,\psi, \tag{2.7}$$

where ρ is density, f is the Coriolis parameter, and ψ is the streamfunction for residual overturning. This ingredient is depicted in Fig. 2.2

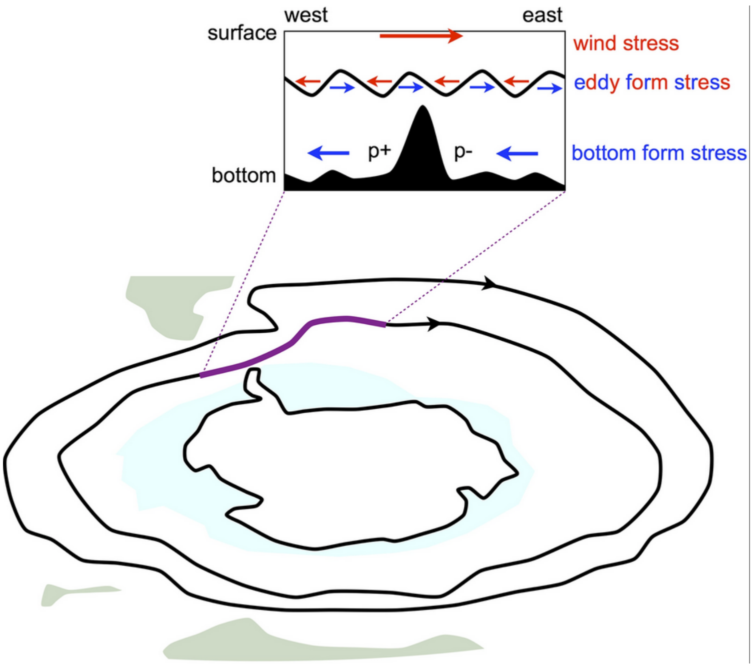

Figure 2.2: Figure 1 from Marshall et al. (2017) showing the hypothesised zonal momentum balance of the ACC. Eastward surface wind stress (red arrow in insert) and bottom form stress (blue arrows) balance each other. Bottom form stress is associated with high and low pressure (p^+ and p^-) that forms on either side of bathymetric obstacles. Eddy form stress transfers momentum downwards when fluids in buoyant layers push against fluid in deeper dense layers. This is depicted by alternative red and blue arrows pointing in opposite directions.

Ingredient (2) gives a relationship between eddy energy and the magnitude of eddy form stress,

$$S = \alpha_1 \frac{|f|}{N} E, \tag{2.8}$$

where $|\alpha_1| \leq 1$ is a non-dimensional parameter and N is the buoyancy frequency (Marshall et al., 2012). Substituting this into the momentum balance equation (Eq.(2.7)) leads to an eddy energy equation,

$$E = \frac{1}{\alpha_1} \frac{N}{|f|} \tau_s + \frac{\rho N}{\alpha_1} \psi. \tag{2.9}$$

This states that eddy energy is set by surface wind stress and a contribution from residual overturning.

The final ingredient balances the source and the sink of eddy energy in equilibrium. In the Southern Ocean, baroclinic instability in the ACC is the dominant source of eddy energy. Assuming uniform shear and stratification for simplicity as in Marshall et al. (2017), this implies that

$$E_{source} = \alpha_2 \frac{|f|}{N} \frac{\partial u}{\partial z} \int_{-H}^{0} E \, \mathrm{d}z. \tag{2.10}$$

This means that the source of eddy energy scales with mean vertical shear ($\partial u / \partial z$), which follows from the theory of eddy energy generation from baroclinic instability. α_2 is another dimensionless constant constrained by $|\alpha_2| \leq 1$, but it is noted that when $\alpha_2 = 0.61$, the growth of eddy energy is equal to the Eady energy growth rate (Eady, 1949). Eddy energy dissipation is more complex, as there are a myriad of contributing processes. An assumption is applied and dissipation is modelled by the constant λ, the eddy energy dissipation rate, so that

$$E_{sink} = \lambda \int_{-H}^{0} E \, \mathrm{d}z. \tag{2.11}$$

In equilibrium, this leads to

$$\alpha_2 \frac{|f|}{N} \frac{\partial u}{\partial z} = \lambda. \tag{2.12}$$

At the seafloor, zonal velocity is assumed to vanish. Integrating mean velocity–$\frac{1}{2}H\frac{\partial u}{\partial z}$–across the channel yields circumpolar volume thermal wind transport:

$$T_{tw} = \lambda \frac{N}{|f|} \frac{H^2 L}{2\alpha_2}. \tag{2.13}$$

In words, the thermal wind transport scales with eddy energy dissipation while the eddy energy scales with surface wind stress, as described in Eqs.(2.9) and (2.13). In summary, these three key ingredients explain the physics of eddy saturation from first principles.

On the other hand, some studies rely on the importance of the ACC's structural adjustment in increasing the efficiency of momentum transfer. As discussed, eddy saturation can be summarised as a balance between surface wind momentum input and opposing topographic form stress. However, some postulate that topographic form stress is linked to retrograde (opposing direction of the mean flow) Rossby waves, or "standing meanders". These meanders are found above topography and enhance eddy form stress. It is also worth noting that topographic regions lead to eddy kinetic energy "hot spots", as topography leads to regions of flattened isopycnals (Kong and Jansen, 2021). Following theory on Rossby wave adjustment, this then suggests that bottom form stress adjusts faster to wind stress changes than isopycnal form stress (Bai et al., 2021). This theory on standing meanders refutes the two-dimensional theory of eddy saturation, which does not account for zonally localised dynamics (Stewart et al., 2023). However, it is unlikely that either theory–eddy transfer theory or standing meander adjustment theory–completely explains eddy saturation.

2.1.5 Timescales of eddy saturation

Pre-existing literature on eddy saturation is primarily focused on thermal wind transport. However, the level of no motion assumption is currently challenged by theory and satellite altimeter data (Donohue et al., 2016). If the bottom flow–the flow at the level of topography–is indeed non-negligible, then the barotropic component of ACC transport likely plays a greater role than it is currently theorised to in the context of eddy saturation, especially at transient timescales (Munday et al., 2013). Some works suggest that bathymetry also plays a larger role in eddy saturation than what is originally predicted (Thompson and Naveira Garabato, 2014; Youngs et al., 2017; Youngs et al., 2019). All these inconsistencies emphasise the incomplete understanding of eddy saturation, particularly at non-equilibrated timescales.

There is evidence for eddy saturation-like behaviour on much shorter timescales than equilibration. The underlying physics of these shorter adjustment timescales is most likely not solely tied to baroclinic instability. Higher frequency variability (subseasonal to interannual) within the ACC is diagnosable to an extent. It is hypothesised that seasonal variation is due to Ekman convergence. Additional data sets show monthly and sub-annual variability resulting from different external sources. On monthly timescales, there is a link between the Madden-Julian oscillation and ACC transport; sub-annually, there is additional wind driven variability. In general, transient variability is seemingly linked with the local effects of the mesoscale eddy field (Hogg and Blundell, 2006). There is some evidence pointing towards the existence of an oceanic Southern Hemisphere Annular Mode (SAM) (Meredith and Hogg, 2006). The SAM is associated with atmospheric variability in eastward wind stress over the Southern Ocean. The oceanic complement to the SAM is predominantly constrained by topography and is not zonally symmetric, thus differing from the SAM (Hughes et al., 2003). GPS (global position system) measurements and data from bottom pressure gauges give observations of seasonal changes in sea level variation (Aoki et al., 2002). Variability is highest between April and June and lowest between November and December, which suggests seasonal patterns that are tied to the existence of an ocean variability mode.

Short-timescale variability resulting from high-frequency wind stress forcing is dominated by the barotropic mode. This mode is spatially concentrated at the southern edge of the Southern Ocean (also known as the Southern mode). In wind forced only models, this barotropic response is immediately manifested during spin up as topographic form stress. Topographic form stress reacts to surface forcing without needing to wait for interfacial form stress to communicate the surface changes downwards (Howard et al., 2015). There is some suggestion that at interannual timescales, transport is controlled mostly by surface wind stress change, however the extent of this is not yet clear. Even so, wind stress variability is responsible for daily-to-interannual variance in sea-level and bottom pressure near Antarctica, as well as transport variability through Drake Passage (Rintoul and Naveira Garabato, 2013).

Understanding lower-frequency variability presents a challenge, as it is not readily diagnosable from available observations. Lower-frequency variability is also more influential in ocean and climate feedback than lower-frequency atmospheric variability. While there is a lack of observations, there is likely a link between potential and kinetic energy on low-frequency timescales. Hogg and Blundell (2006) investigate a three layer quasigeostrophic model subjected to steady wind forcing. This model allows for a realistic simulation of baroclinic instability. Kinetic and potential energy oscillate between several regimes following spin up. These regimes, labelled A, B, C, and D (see Fig. 2.3) are characterised by different patterns in kinetic and potential energy. Regime A, characterised by low kinetic and low potential energy, leads to a relatively weak zonal mean flow. Baroclinic eddies are weak in this regime as the potential energy reservoir is low. In regime B, kinetic energy remains low while potential energy grows. This regime is associated with an increase of the mean zonal flow and a dissipation in the zonal jet structure. In both regimes A and B, the energy input from wind stress rises, while potential energy absorbs the excess energy. Regime C has a peak in potential energy and a rapid kinetic energy increase. The flow now exceeds the threshold for baroclinic instability, resulting in the strongest zonal flow and the strongest eddy influence. Potential energy feeds the turbulent kinetic energy field, while drag and dissipation act as energy sinks. Finally, in regime D, there is a decrease in kinetic energy, potential energy, and the influence of eddies, even though the jet remains strong. As the potential energy depletes, so does the fuel for kinetic turbulent energy (Le Bars et al., 2016). In conclusion, Hogg and Blundell (2006) use the existence of these regimes to identify variability modes in circumpolar currents. This is consistent with the eddy-mean flow feedback framework. This cycle allows for the growth and depletion of the mesoscale eddy field on decadal timescales.

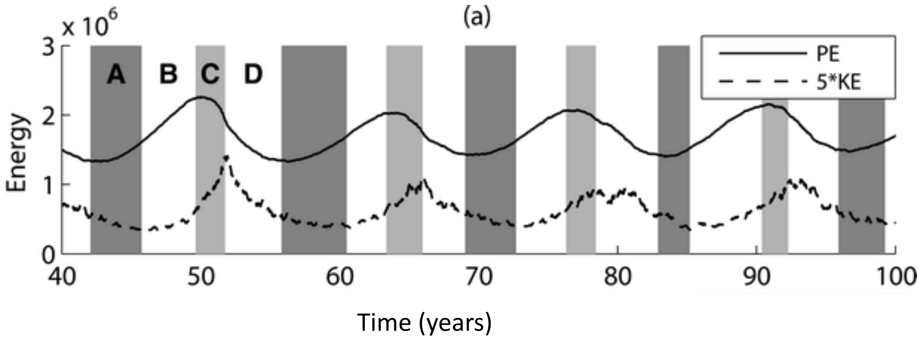

Figure 2.3: Figure 12(a) from Hogg and Blundell (2006), showing the energy regimes of the three-layer quasigeostrophic model forced by temporally steady winds. Total potential energy and kinetic energy (multiplied by 5) are shown against time. Regimes A, B, C, and D are indicated by colour gradient (A-dark grey, B-unshaded/white, C-light grey, D-unshaded/white).

In addition to a link between the growth and decay of kinetic and potential energy, there is evidence for a feedback loop between eddies and the mean flow. In Meredith and Hogg (2006), an ACC-like, three-layer, quasi-geostrophic, eddy resolving model with topography is analysed. This model is forced with a perturbed wind stress. Results indicate that there is a 2 to 3 year lag between peaks in wind stress magnitude and eddy kinetic energy peaks. Following a peak in wind stress, potential energy quickly increases and the (total) kinetic energy peak lags by 1 to 2 years. The exact timing depends on wind stress magnitude, as greater magnitudes lead to shorter lag time. In this study, eddy saturation is also discussed, as the circumpolar transport behaves with relative insensitivity to wind stress changes (with less than 5% transport change). This however does not strictly follow the definition of eddy saturation discussed in Straub (1993), Munday et al. (2013), Mak et al. (2017), and Mak et al. (2018). While it may be true that eddy saturation takes place over both short and long timescales, the physics linking these regimes is currently unclear. It is possible that the physics controlling the ACC at short and long timescales greatly differs, as there is no time for density surfaces to slump in the transient case (Youngs et al., 2017). Furthermore, there is some model evidence to suggest that ACC volume transport responds to wind stress by up to 10 Sv on the order of weeks, but decreases over the next 3 to 6 months, suggesting a delayed eddy response (Zika et al., 2013). This however, fits less with the current understanding of eddy saturation timescales. This variability is shorter term than that discussed in Meredith and Hogg (2006), but it is interesting that a delayed eddy response is suggested by both sets of results.

In Sinha and Abernathey (2016), the timescales of Southern Ocean equilibration to temporally changing winds is investigated. They hypothesise that the transient response lies between an Ekman response (high frequency) and equilibrated eddy saturation (low frequency). This work primarily focuses on the pathways between eddy kinetic energy (EKE) and available potential energy (APE) in an ACC-like channel model forced by oscillatory wind stress forcing. The experiments consist of the following seven oscillation periods: $P \in \{\frac{1}{4}, \frac{1}{2}, 1, 2, 4, 8, 16\}$ years. By analysing the EKE and APE pathways, they conclude that for oscillations of $P \leq 2$ years, the Ekman response is primarily in control. In this high frequency regime, sloping isopycnals store APE while the mesoscale eddy field is too slow to remove excess wind works. Equilibrated eddy saturation then takes over for oscillation periods of $P \geq 8$ years as the mesoscale eddy field "catches up" and is able to remove excess wind work.

The crossover region between the high and low frequencies is stated to contain the eddy diffusive transport timescale across the ACC, given by $c = \kappa_{GM}/L_y^2$, (see Section 2.2.1 for an overview of the κ_{GM} term). We note that there is an order of magnitude error in this timescale. The conversion timescale is given to be 3 years, which makes sense in the context of their work. Experimental frequencies are normalised to this conversion timescale. Frequencies higher than c are referred to as "high frequency" and frequencies lower than c are referred to as "low frequency". However, this timescale as computed with the correct conversion factors is 30 years, which is a timescale beyond the scope of their experimental setup. It would be interesting to see the behaviour of the system at this corrected timescale in the context of energetic feedbacks. While this error does not carry through to the experimental results, it does indicate that timescales of 30 years or longer may be of importance in understanding the role of baroclinicity in eddy saturation. One of the most important conclusions from this work involves the conversion from APE to EKE. The physical processes behind this conversion, baroclinic instability and frictional dissipation, possess different timescales. The mesoscale eddy field plays an integral part in this conversion, even feeding back on the conversion rate through itself.

2.1.6 Observations

Accurate observations and numerical models are relatively recent advancements in Southern Ocean research. There has historically been a lack of observed data from the Southern Ocean. The World Ocean Circulation Experiment (WOCE) took field measurements during the 1990s, providing the first circumpolar survey of the Southern Ocean since the early 1970s. Further analysis and modelling then ran until 2002 (Orsi and Whitworth, 2005). WOCE provided some of the first interior observations of this region (Gould et al., 2013). Then, from 2003, Argo profiling floats have been deployed. These floats take temperature and salinity profiles south of $40°$S to depths of 2000 m (Scripps Institution of Oceanography, accessed 2023). The floats take measurements every ten days, but are unable to take under ice measurements. More recently, southern elephant seals have been gathering temperature and salinity profiles to supplement this data. Sensors are harmlessly attached to the seals and fall off after several months of collecting data (Charrassin et al., 2008). Elephant seals are advantageous since they can swim and collect data from under the ice, unlike the Argo floats. Satellite altimeter data also provides year round views of the Southern Ocean (Rintoul and Naveira Garabato, 2013). This data records surface sea level anomalies which can be used to characterise geostrophic flow anomalies.

The Southern Ocean plays a central role in setting the global climate as it links the world's ocean basins. When compared to the Arctic, the Antarctic region's temperature has not increased as dramatically. This is due to the combined contribution of heat uptake and deep ocean mixing within the Southern Ocean. However, this does not mean that the Southern Ocean is unaffected by climate change (Meredith et al., 2019). The positive trend in the Southern Annular Mode is thought to alter the westerly winds over the ACC. Predicted changes include an intensification and a southward shift of the wind stress jet. Model predictions and observational data analysis mostly support the predicted wind intensification, but there is relatively little observed data to confidently support a southward shift. Even so, it is likely that the position and strength of the ACC will remain insensitive to wind stress changes (Donohue et al., 2016). There does exist observational data on ACC transport, but with major caveats surrounding changes in barotropic transport. Satellite measurements over the past 20 years support a statistically significant upward trend in eddy energy in response to increased wind stress magnitude, thus supporting the current theoretical understanding of eddy saturation (Munday et al., 2013).

Despite the progress made on collecting observations on the Southern Ocean, there are many processes that cannot be directly observed. For example, overturning must be inferred by inverse methods (Hogg et al., 2015). This means that many studies use model results rather than observational data. Unlike the model results primarily discussed in this chapter, Southern Ocean observations are collected over short time periods, and contain a large degree of noise. Contrasting with methods in collecting observed data, model results are often perturbed after reaching a steady state. For example, there may be a multiyear lag between wind stress anomalies and the eddy response, as well as a degree of transport sensitivity to wind stress anomalies at sub-annual timescales (Screen et al., 2009; Mazloff, 2012)

2.1.7 Climate implications

The Antarctic region disproportionately and increasingly affects global climate change. The Southern Ocean plays an important role as it acts as a communication interface between the atmosphere and global oceans, especially when it comes to heat and carbon uptake. In this region, pre-industrial era water from the deep ocean is ventilated to the post-industrial atmosphere. This upwelled pre-industrial water is very cold and devoid of dissolved carbon, hence, it is able to take up a large amount of these tracers (Frölicher et al., 2015). While climatic changes take place on a wide array of timescales–from decades to millennia–many of the anthropogenic effects lead to irreversible changes.

Human activity releases carbon dioxide (CO_2) into the atmosphere, some of which is absorbed into the ocean. This leads to ocean acidification, which is predicted to affect the Southern Ocean first and most severely (Vaughan et al., 2003; Khatiwala et al., 2013). This uptake affects marine life and ecosystems. For example, some organisms use calcium carbonate in shell and skeleton formation. However, as excess CO_2 dissolves into surface waters the pH of the ocean is lowered (acidification), which increases carbonate ion concentration. This dissolves the shells of certain organisms but leads to increased shell-building in others. This alters organism population structure and is yet another consequence of anthropogenic climate change, especially affecting the Antarctic region (Figuerola et al., 2021).

In addition to carbon storage, the Southern Ocean is key in ocean heat content change and storage. Between 1870-1995, the Southern Ocean accounted for approximately 75% of excess heat uptake (Frölicher et al., 2015). Of that excess heat, approximately 43% remained in the Southern Ocean while the rest was redistributed around the global ocean (Shi et al., 2018; Meredith et al., 2019). Heat uptake is not uniform throughout the ocean depth. The upper 2000 m is responsible for heat uptake, while the depth below this stores the excess anthropogenic heat. However, this storage is leading to a volumetric decrease of the Antarctic bottom waters, as density surfaces deepen. This then further drives warming downwards.

While the Southern Ocean is a prime location for ocean heat uptake, warming in this region is weaker than the Arctic as deep ocean mixing stalls warming (Marshall et al., 2014). The SAM also helps in maintaining the cool conditions over the Antarctic continent. These cool conditions are a consequence of the strong westerlies over the ACC. Since the 1970s, the SAM has been growing stronger, thus leading to stronger winds, especially in austral summer (Swart et al., 2015). This positive trend results from excess greenhouse gases (a constant forcing) and ozone depletion (leading to strong seasonal variability, although this depletion is no longer an issue). This in turn–and perhaps counter-intuitively–prevents rapid heating in the Antarctic continent (Swart et al., 2018). Some wind driven changes do lead to increased warming towards the north of the Southern Ocean. For example, increasing temperature trends in the seawater are driven by air-sea flux changes. This is particularly seen towards the equator, where wind changes alter the thickness and depth of the mode water layer.

The future projections of the Southern Ocean focus on the strengthening westerlies. Numerical simulations suggest that this will lead to an intensification of the eddy field. It is also suspected that there will be increased warming and increased freshwater flux from melting sea ice and increasing precipitation. Models also suggest that tracer transport (i.e., heat, carbon, nutrients) and upper-ocean circulation will be the properties most affected by the increasing winds and eddy field. Contrastingly, ACC transport and location will only have weak sensitivity to increasing wind stress (Fox-Kemper et al., 2019; Meredith et al., 2019).

2.2 Eddy parameterisation

While still an area of active research, global climate models have also drastically improved within the recent past. Coupled models such as the Coupled Model Intercomparison Project Phase 5 (CMIP5) are crucial in better understanding dynamics and making predictions about the future state of the climate and ocean (Meredith et al., 2019). Spurious results or model issues are often rooted in faulty biases of historical ocean states. As observational data is more readily available, these issues should improve (Russell et al., 2018). However, model performance is still limited by the inability to explicitly and efficiently resolve the mesoscale eddy field (Rintoul and Naveira Garabato, 2013; Meredith et al., 2019).

In an ideal world, the mesoscale eddy field in the Southern Ocean would be explicitly modelled on a high resolution domain. Currently, this is computationally unfeasible. To accurately model the mesoscale eddy field, a grid resolution of $1/10°$ or finer is required. This high resolution simulation would then preferably run for hundreds to thousands of model years in order to reach equilibrium (Griffies, 1998). This issue is further compounded by the fact that transient eddies contain more energy than the mean flow, meaning that eddies greatly affect the large scale behaviour of the flow (Screen et al., 2009; Williams and Follows, 2011). This has substantial impacts on ocean heat uptake, carbon storage and transport, and other properties, all of which influence climate sensitivity in models. In high resolution models, the mesoscale eddy field is fully resolved and thus fully incorporated into the dynamics and subsequent results. However, not all models are at such high resolution. Lower resolution models can capture eddy saturation by means of parameterisation. Eddy parameterisations represent the effects of eddy-induced advection and eddy-induced diffusion.

The Gent-McWilliams scheme parameterises eddy-induced advection (Gent and McWilliams, 1990) and incorporates the Redi (1982) scheme with an anisotropic diffusion tensor (Gent et al., 1995) to include the effects of the mesoscale eddy field at low resolution. In current practice, both eddy-induced advection and diffusion are parameterised and treated as the antisymmetric and symmetric components of an eddy diffusivity tensor (Griffies, 1998; Fox-Kemper et al., 2019). Defining this tensor is an area of active research, with some evidence suggesting that the tensor should depend on eddy energy (Bachman and Fox-Kemper, 2013; Jansen et al., 2015; Mak et al., 2017; Bachman et al., 2017).

2.2.1 Mathematical details of Gent-McWilliams

In models that do not resolve eddies, the effects of baroclinic instability must instead be parameterised. The Gent-McWilliams scheme parameterises the effects of baroclinic mesoscale eddies by introducing an adiabatic stirring term to the mean density equation (Gent and McWilliams, 1990; Gent et al., 1995). This mathematically represents the eddies counteracting the steepening isopycnals and decreases the available potential energy. This subsection will proceed as follows:

1. a brief history and the contextual background of the Gent-McWilliams parameterisation scheme (GM);

2. a two-dimensional mathematical overview of GM; and

3. a discussion on some benefits and known deficiencies of GM.

The original motivation behind GM was to improve upon the previous technique of diffusing tracers along isopycnal surfaces in order to incorporate some effects of the mesoscale eddy field by instead parameterising the effects on an adiabatic flow. Before Gent and McWilliams (1990) closure terms–such as for potential temperature–were implemented by horizontal and vertical Laplacian diffusion. Even so, it was already known that mixing occurs more strongly along– rather than across–isopycnal surfaces. Hence, tracer diffusion ought to be oriented along (Redi, 1982) and perpendicular to isopycnals. A mathematical interpretation of this was necessary.

GM preserves the following three properties of the adiabatic primitive equations:

1. the volume between any two isopycnals is conserved, subject to a suitable choice of boundary conditions;

2. the domain average of tracers between any two isopycnals is conserved with the appropriate boundary conditions;

3. the equation for passive tracers is satisfied identically by the density.

To accomplish this, GM parameterises the effects of baroclinic eddies by introducing an adiabatic stirring of the mean density in order to decrease the available potential energy. Specifically, the effects of eddies are parameterised by the non-conservative term: $\nabla \cdot \mathbf{F}$, which appears in the thickness equation (in isopycnal coordinates). That is,

$$\frac{\partial h_\rho}{\partial t} + \nabla \cdot (\mathbf{u} h_\rho) + \nabla \cdot \mathbf{F} = 0, \tag{2.14}$$

where h is depth, ρ is potential density, and h_ρ is isopycnal layer thickness. This can be reformulated as,

$$\frac{\partial h_\rho}{\partial t} + \nabla \cdot (\mathbf{u}h_\rho) = \nabla \cdot (\kappa \nabla h)_\rho. \tag{2.15}$$

The κ term comes from the choice of $\mathbf{F}$. At the time of publication, κ was referred to as the "thickness diffusivity" whereas it is now better referred to as an eddy transfer coefficient (and will be for the rest of this thesis).

More relevant to this thesis is the reformulation of GM in two dimensions (Young, 2012; Gent et al., 1995). In Cartesian coordinates in two dimensions (the zonally averaged Boussinesq case),

$$\frac{\partial \rho}{\partial t} + (\mathbf{u}_{mean} + \mathbf{u}_{eddy}) \cdot \nabla \rho = 0, \tag{2.16}$$

where the mean and eddying components of velocity have been separated. Eq.(2.16) arises from thermodynamics in the purely adiabatic case. Additionally, this only holds in idealised conditions (i.e., zero-diffusion and a linear equation of state). The mean velocity is zonally averaged at constant height. The flow is non-divergent, leading to mass conservation in the Boussinesq limit,

$$\nabla \cdot (\mathbf{u}_{mean} + \mathbf{u}_{eddy}) = 0, \tag{2.17}$$

where

$$\nabla \cdot \mathbf{u}_{mean} = 0, \tag{2.18}$$

and

$$\nabla \cdot \mathbf{u}_{eddy} = 0. \tag{2.19}$$

Defining eddy streamfunctions is of particular interest. Applying GM (Gent et al., 1995) leads to

$$\psi_{eddy} = \kappa \left[\frac{\partial \rho}{\partial y}\right] \left[\frac{\partial \rho}{\partial z}\right]^{-1}, \tag{2.20}$$

where

$$\mathbf{u}_{eddy} = \left(\frac{\partial \psi_{eddy}}{\partial z}, -\frac{\partial \psi_{eddy}}{\partial y}\right). \tag{2.21}$$

This means that there is an eddy induced overturning in which neutral surfaces are flattened. In the eddy streamfunction, $[\frac{\partial \rho}{\partial y}][\frac{\partial \rho}{\partial z}]^{-1}$ can be interpreted physically as the negative slope of the mean density surfaces.

The choice of κ is an active area of research. However, GM has its shortcomings, often linked to this choice of κ. As stipulated by GM, κ can be spatially varying, but it is often taken to be a constant over space and time. Standard GM neglects the influence of eddy Reynolds stresses which results in generation of strong recirculations around topography, and jet formation (Marshall et al., 2012). Crucially, when a constant κ is used, the ACC transport is excessively sensitive to wind stress changes (Munday et al., 2013; Mak et al., 2017).

2.2.2 GEOMETRIC

GEOMETRIC (Geometry and Energetics of Ocean Mesoscale Eddies and Their Rectified Impact on Climate) is a framework for parameterising eddies to better represent oceanic eddy-mean flow in climate models while conserving momentum and satisfying energetic constraints (Marshall et al., 2012). GEOMETRIC works by preserving conservation laws in the unaveraged equations of motion by the use of closures to preserve tensor properties and symmetries of the eddy flux tensor. There are two fundamental elements in GEOMETRIC:

1. eddy mean flow interaction is represented through an eddy stress tensor that can be bounded by total eddy energy;
2. there is a consistent solution to the eddy energy equation for both parameterised and resolved processes.

In the simple case when lateral Reynolds stresses are neglected and eddy buoyancy fluxes are closed, GEOMETRIC defines the GM eddy transfer coefficient as

$$\kappa = \alpha E \frac{N}{M^2}, \tag{2.22}$$

where E is total (kinetic and potential) eddy energy, $N = (\frac{\partial \bar{b}}{\partial z})^{1/2}$ is the vertical buoyancy frequency, and $M^2 = \left|\nabla_H \bar{b}\right|$ is the horizontal buoyancy frequency. The overline indicates a time mean over many mesoscale eddy turnover times at fixed height in coarse resolution. The dimensionless parameter, $|\alpha| \leq 1$, is the GEOMETRIC eddy efficiency parameter. More specifically, α measures the relative magnitudes of the eddy buoyancy fluxes to the eddy kinetic and eddy potential energy (Bachman et al., 2017). This means, however, that if the eddy energy and stratification is known, the only quantity left to define is a dimensionless and bounded parameter. In practice, the choice of α acts to tune the parameterisation. GEOMETRIC has resulted in emergent eddy saturation in ACC-like models (Mak et al., 2017; Marshall et al., 2017; Mak et al., 2018).

An eddy energy budget is formulated in order to satisfy element (2) of GE-

OMETRIC. This energy budget is chosen to vary in both space and time. The following depth integrated eddy energy budget is given in Mak et al. (2018),

$$\frac{\partial}{\partial t}\int E\,\mathrm{d}z+\nabla_H\cdot[(\tilde{\mathbf{u}}-|c|\,\mathbf{e}_x)\int E\,\mathrm{d}z]=\int\kappa\frac{M^4}{N^2}\,\mathrm{d}z-\lambda\int E\,\mathrm{d}z+\eta\nabla_H^2\int E\,\mathrm{d}z, \tag{2.23}$$

where $\tilde{\mathbf{u}}$ is depth-averaged flow, c is the baroclinic Rossby phase speed which varies with latitude, $\mathbf{e}_x$ is the longitudinal unit vector, and η is the Laplacian diffusion coefficient of depth-integrated eddy energy. From left to right on the right hand side, the terms represent the following: source, dissipation, and diffusion of eddy energy; the second term on the left hand side represents the advection of eddy energy. Dynamically, Eqs.(2.16) to (2.21) still hold for GEOMETRIC. Likewise, Eq.(2.23) is applicable to standard GM.

2.3 Modelling eddy saturation

This section describes how eddy saturation is modelled and hypothesised mechanisms behind it. Two high resolution models are first put forth and discussed. Both of these lead to eddy saturation, but the models differ in configuration and analysis. Firstly, Munday et al. (2013) show eddy saturation at equilibrated timescales at high resolution. Secondly, Constantinou and Hogg (2019) detail a multi-layer channel model used to investigate different dynamical perspectives of eddy saturation. Thirdly, Mak et al. (2017) and Mak et al. (2018) both employ GEOMETRIC to reach emergent eddy saturation, but in two- and three-dimensions, respectively.

Munday et al. (2013) show equilibrated eddy saturation in sufficiently high resolution ACC-like models. Munday et al. (2013) analyse a narrow sector model in MITgcm forced by a sinusoidal steady (in latitude) wind stress profile with surface buoyancy restoring conditions. The longitude spans from 60°S to 60°N and the domain is $20°$ wide. This domain is on the longer side to allow representation of overturning circulation. This is necessary for the inclusion of eddy compensation. Hence, the model domain's narrow East-West width is dictated by computational expense in order to balance out the meridional extent. The narrow domain additionally allows this configuration to reach equilibrium faster, which is advantageous since eddy saturation is investigated at equilibrium. This model has mostly flat bathymetry, with the exception of a one grid-cell half-depth ridge appended to the circumpolar channel in order to ensure that the surface wind stress is balanced by bottom form stress via interfacial form stress. The Gent-McWilliams parameterisation is used for all grid resolutions investigated ($2°, 1/2°$, and $1/6°$). For coarse resolution ($2°$), GM is used to parameterise the entire eddy field. At finer resolutions, GM is used for eddy closure. The eddy transfer coefficient, κ, is chosen to decrease with resolution. This ensures that in comparison with the meridional heat transport, GM's contribution is small.

The key result of this work shows that there is eddy saturation at high resolutions and wind sensitivity at low resolutions when the Gent-McWilliams parameterisation (GM) is used. This parameterisation is detailed in Section 2.2.1. At low resolution, GM is used purely to parameterise the eddy field, and transport grows with wind stress magnitude. At higher resolutions ($1/2°$ and $1/6°$), the model shows a high degree of eddy saturation. However, as wind stress magnitude increases, so does the variability in transport, supporting the idea that extra energy from wind work is transferred into variability rather than to the mean flow. This further emphasises that this extra wind work goes towards increasing eddy energy rather than increasing equilibrium transport (Marshall et al., 2017). These experiments are run for model years on the order of centuries to millennia in order to reach thermodynamic equilibrium. In this case, eddy saturation is only discussed for the equilibrated state.

Alternatively, some work suggests that eddy saturation is not just a consequence of baroclinic instability, but also a consequence of feedbacks between transient eddies and the mean flow (Constantinou and Hogg, 2019). Constantinou and Hogg (2019) use a high resolution zonal re-entrant channel with several Gaussian ridges at 4 km grid resolution. Parameters are typical for the Southern Ocean, and a steady eastward wind stress forces the model. The primitive equations are solved in isopycnal coordinates and the Boussinesq approximation is used. The wind stress magnitude and number of vertical layers is varied. Wind stress spans four orders of magnitude, $\mathcal{O}(10^{-3})$ $\mathrm{N/m^2}$ to $\mathcal{O}(10^{1})$ $\mathrm{N/m^2}$. Barotropic and baroclinic dynamics are separated by varying the number of vertical layers in calculations. When $n = 1$ layer is used, the system only exhibits barotropic dynamics. When $2 \leq n \leq 4$ layers are used, the dynamics are combined barotropic and baroclinic; as the dynamics are qualitatively similar for each baroclinic case, $n = 2$ is used in analysis. Therefore, this experimental set up allows for separation between the two dynamical regimes by design.

The model is run to equilibrium as determined by kinetic and potential energy. For the purely barotropic case, this takes about 5 years, and for the baroclinic case, this can take up to 500 years (when wind stress is extremely weak). For extremely weak wind forcing ($\tau_s \leq 0.02$ $\mathrm{N/m^2}$), barotropic transport increases linearly with wind stress. At intermediate wind stress (0.05 $\mathrm{N/m^2} \leq \tau_s \leq 6.0$ $\mathrm{N/m^2}$) transient eddy generation is responsible for the relative wind stress insensitivity, even in the barotropic case. Finally, at high winds (7.0 $\mathrm{N/m^2} \leq \tau_s$), barotropic transport scales with the square root of wind stress magnitude. In the baroclinic case, transport is relatively insensitive, if not negatively correlated, to wind stress magnitude for $\tau_s \leq 0.5$ $\mathrm{N/m^2}$, which is similar to the results from Mak et al. (2018). For high wind stress (1.0 $\mathrm{N/m^2} \leq \tau_s$), baroclinic transport also follows the square root of wind stress magnitude, like in the barotropic case. When more realistic wind stress magnitudes are prescribed, both the barotropic and baroclinic setups are eddying in the equilibrated state. The barotropic case is steered by topography whereas the baroclinic case shows an imprint of the bathymetry.

The results from both cases suggest that eddy saturation is not just controlled by baroclinic mechanisms. In both the barotropic and baroclinic configurations, the bathymetry greatly influences the mesoscale eddy field. This in turn prevents transport from growing with wind stress magnitude, as a pathway for topographic form stress to counter surface wind stress is evidently available. While this can be attributed to baroclinic instability in the multi-layer case, this is fully attributed to topographic interaction in the barotropic case. This suggests that eddy saturation may occur on different timescales, but from different physical processes. It is worth noting however, that the use of a fully barotropic model for comparison with a barotropic-baroclinic model is unorthodox, as in a fully barotropic setup there are no baroclinic eddies. Mixed barotropic-baroclinic dynamics have been studied in other works, such as in Youngs et al. (2019). It is hypothesised that the ACC may exhibit mixed instability. In particular, mixed barotropic-baroclinic instability may play a central role in potential and kinetic energy conversion.

2.3.1 Modelling with GEOMETRIC

Much of the work in this thesis follows on from Mak et al. (2017) and Mak et al. (2018). In these papers, GEOMETRIC is implemented in idealised ACC-like configurations. Both of these works are now summarised in chronological order of publication. In the former, several different parameterisation methods are implemented in a two-dimensional model in y and z, where $(y, z) \in ([0\ \mathrm{km}, 2000\ \mathrm{km}] \times [-3\ \mathrm{km}, 0\ \mathrm{km}])$. The domain is forced by a steady sinusoidal wind stress, with a bottom form stress of equal and opposite magnitude to the surface stress to represent the effects of bottom topography. Four parameterisation methods are used with different definitions of the eddy transfer coefficient. Here we discuss the results of standard GM and GEOMETRIC. In experiments, peak wind stress and eddy energy dissipation (λ) are varied following spin up to steady state. As expected, when standard GM is used, thermal wind transport is sensitive to wind stress. When κ is defined by GEOMETRIC, transport has low sensitivity to peak wind stress. It is shown that κ decreases with λ, as eddy energy dissipation scales with λ, and κ scales with eddy energy.

Mak et al. (2018) continue to use GEOMETRIC to investigate eddy saturation in an ACC-like configuration, only this time in three spatial dimensions. Here, constant κ (GM-like) and GEOMETRIC are compared to an eddying reference case. GEOMETRIC is used in two different ways, locally and integrated ($\mathrm{GEOM_{loc}}$ and $\mathrm{GEOM_{int}}$ respectively). As the name suggests, $\mathrm{GEOM_{int}}$ uses the domain-integrated eddy energy budget. This leads to the eddy transfer coefficient,

$$\kappa_{\text{int}}(t) = \alpha \frac{\iiint E \, \mathrm{d}z \, \mathrm{d}x \, \mathrm{d}y}{\iiint (M^2/N) \, \mathrm{d}z \, \mathrm{d}x \, \mathrm{d}y}, \tag{2.24}$$

which can vary in time but is spatially constant, similar to the first experiment set in Mak et al. (2017). $\mathrm{GEOM_{loc}}$ is depth-integrated, allowing it to spatially vary in the horizontal while remaining constrained in the vertical. The eddy transfer coefficient is given by

$$\kappa_{\text{loc}}(t, x, y, z) = \alpha \frac{\int E \, \mathrm{d}z}{\int \mathcal{S}(z)(M^2/N) \, \mathrm{d}z} \mathcal{S}(z), \tag{2.25}$$

where $S(z)$ is a prescribed and dimensionless structure function.

Calculations are for a channel that is 4000 km long, 2000 km wide, and has a maximum depth of $3000\ \mathrm{m}$. The channel contains a ridge with a maximum height of $1500\ \mathrm{m}$ to allow for topographic form stress. After running calculations to equilibration, transport decreases with increased wind stress in the eddying and GEOMETRIC cases. While this is not eddy saturation, it is notable that GEOMETRIC follows the behaviour of the eddying calculations. In this configuration, the thermocline shallows with increasing winds. However, this may be an artefact of the high vertical diffusivity imposed at the northern boundary. In the sector model, this inverse relationship is absent. In comparison with the constant eddy transfer coefficient calculations (standard GM), the eddying and GEOMETRIC calculations are much closer to eddy saturated. Furthermore, when constant κ is used, transport increases with wind stress magnitude as expected. In all these calculations however, it is stated that thermal wind transport composes most of the total transport. Hence, eddy saturation is assumed to be controlled by baroclinic instability, and no prediction is made for (barotropic) bottom or total transport.

Therefore, in Mak et al. (2017) and Mak et al. (2018), eddy saturation is discussed for long timescales, just as it is in Munday et al. (2013). Here, eddy saturation is the product of baroclinic instability inducing isopycnal slumping, which is countered by eddy-induced stirring. Due to this mechanism, it is not surprising that eddy saturation is only discussed in the long term, as this physics is most relevant to equilibrated thermal wind transport.

As mentioned, there is a discrepancy between standard GM and eddy resolving models when it comes to modelling the response of the Southern Ocean to different wind stresses. In particular, coarse-resolution models employing GM exhibit a higher degree of sensitivity to wind stress than eddying models and (to some extent) observational data. However, in models applicable to the Southern Ocean, GEOMETRIC is far more insensitive to changes in surface wind stress. In other words, GM does not lead to eddy saturation, whereas GEOMETRIC and eddy resolving models suggest eddy saturation in the Southern Ocean.

2.4 Conclusions

This chapter provided a condensed overview of the Southern Ocean and ACC dynamics. Eddy saturation and its representation in high and low resolution models was discussed, with a particular selection of sources and methods reviewed in detail. The rest of this thesis focuses on circumpolar adjustment on various timescales in the context of eddy saturation. As discussed, eddy saturation is the insensitivity of thermal wind transport to wind stress on equilibrated timescales. However, many sources describe eddy saturation-like behaviour on transient timescales. This thesis attempts to reconcile transient and equilibrated eddy saturation through the investigation of a hierarchy of circumpolar channel models. The use of a hierarchy of models is advantageous in discerning the relevant physical mechanisms to circumpolar adjustment on different timescales, as well as model dimension and resolution. It is hoped that the findings will have some applicability to the Antarctic Circumpolar Current in more realistic models and in the ocean.

3 | Models and methodology

This thesis focuses on numerical results from ACC-like configurations in multiple dimensions. Models in three-dimensions are configured using the Massachusetts Institute of Technology general circulation model (MITgcm) (Marshall, Adcroft, et al., 1997; Marshall, Hill, et al., 1997). Certain diagnostics and mathematical techniques are readily used throughout this thesis, both with and without outputs of MITgcm. The following chapter provides a brief overview of MITgcm, detailed definitions of frequently used diagnostics, and a summary of any non-obvious mathematical techniques.

3.1 MITgcm

MITgcm is a model rooted in the incompressible Navier-Stokes equations (Marshall, Adcroft, et al., 1997; Marshall, Hill, et al., 1997). This model is used for both ocean and atmosphere calculations from large to small scales. To accommodate an array of scales, MITgcm can include a non-hydrostatic term as well as capture mixing processes. This model also uses finite volume method representations of topography, allowing for detailed dynamical topographic interactions. MITgcm is used widely and regularly in both oceanic and atmospheric studies. This software is highly portable and can run on a vast array of computational platforms. For example, simple models can run on the Author's Lenovo ThinkPad and more computationally expensive models are run on ARCHER2. This thesis uses MITgcm to configure ACC-like models. In Chapter 6, circumpolar channel models with topographic obstructions are used to represent the ACC. Bathymetry is easily incorporated into the model, and more realistic configurations are also possible (although beyond the scope of this thesis).

3.1.1 Circumpolar channel model configuration

MITgcm is used to simulate an eddy parameterised and an eddy resolving three-dimensional circumpolar channel. These configurations simulate wind forced flow through a channel with bathymetry. By choosing the appropriate parameters and making configuration choices, these models crudely mimic the ACC. The details of the configurations are discussed below.

The model domain is 2000 km wide and 6000 km long with a maximal depth of $H_0 = 5000$ m. A submerged ridge is centred in the domain and defined

$$h = h_0 \cos(2\pi x/N_x)^{20} - H_0 \text{ where } x \in [N_x/4, 3N_x/4] \tag{3.1}$$

where $h_0 = 1500$ m and N_x is the number of grid points over the whole domain in the x-direction. In the eddying configuration, $N_x = 600$ and in the eddy parameterising configuration, $N_x = 60$. The eddy resolving configuration is high resolution, with zonal grid size of 10 km which is about $1/10°$ in this region. The eddy parameterised configuration is coarser (about $1°$ in this region) with zonal grid size of 100 km. In both models, the grid is Cartesian and the Coriolis parameter f is defined

$$f(y) = f_0 + \beta y. \tag{3.2}$$

In the Southern Hemisphere, f_0 is negative; in these configurations, $f_0 = -1.363 \times 10^{-4}\ s^{-}1$ and $\beta = 1.47 \times 10^{-11}\ s^{-1}\mathrm{m}^{-1}$. A linear equation of state is used where density only depends on temperature with thermal expansion coefficient $2 \times 10^{-4}\ K^{-1}$. There is no sea ice present.

In both configurations there are thirty unevenly spaced vertical levels. From the surface to sea floor these layers increase with depth from 10 m at the surface to 421.5 m at the bottom[1]. There is no rigid lid and the implicit free surface option is turned on. The boundary conditions at depth are no-slip, and at the walls the boundary conditions are free-slip. The advection scheme is a seventh order one-step method.

The eddy parameterised configuration uses GEOMETRIC. GEOMETRIC is implemented within the GM/Redi package in MITgcm (Mak et al., 2018). This package is used to compute the eddy transfer coefficient, κ, and the parameterised eddy energy. The eddy transfer coefficient is capped from above and below by κ_{max} and κ_{min} respectively to prevent unstably large eddy-induced velocities and ensure a minimal level of parameterised eddy activity; specifically $\kappa_{min} = 50\ \mathrm{m}^2/s$ and $\kappa_{max} = 10000\ \mathrm{m}^2/s$. Other parameter choices are discussed in detail in Chapter 6.

3.2 Diagnostics

Throughout this thesis, there are some frequently used diagnostics. This section defines and discusses these diagnostics. The total Antarctic Circumpolar Transport is given by

$$T_{\mathrm{ACC}}(t) = \iint u_x(t, y, z)\ \mathrm{d}y\mathrm{d}z, \tag{3.3}$$

where u_x is the zonal velocity value taken at a single longitude. This longitude is chosen to be furthest away from the ridge at $x = 6000$ km for this thesis. In other studies, transport is often time and/or zonally averaged. In this thesis, transport is not time averaged in order to study the transient response. By conservation of

[1]The exact vertical spacing is: $\Delta z = 10, 11.4, 12.9, 14.7, 16.7, 19, 36.8, 41.5, 47.3, 53.8, 61.2, 69.6, 79.1, 90, 102.4, 116.5, 132.5, 150.7, 171.4, 195, 221.8, 252.3, 287, 326.5, 372.4, 421.5, 421.5, 421.5, 421.5, 421.5$ m.

mass, zonal averaging is not necessary and is not used. Total ACC transport is broken down into the bottom and thermal wind (arising from thermal wind shear) transports (Munday et al., 2015). Velocity is computed at the cell centres, hence bottom transport is computed using the velocity one half grid point from the base, so that

$$T_{\mathrm{b}}(t) = \int u_b(t, y)\mathrm{d}y\mathrm{d}z \tag{3.4}$$

where $u_b(t) = u(t, x, y, -H + \Delta z_b/2)$ is flow at the one half grid point, Δz_b (approximately $210\ \mathrm{m}$), from the base, and H is the depth. Like in total transport, the zonal velocity is taken at the same single longitude, although it is noted that bottom transport is not independent of longitude. In words, this is the bottom flow integrated through the full column of water. This diagnostic is particularly relevant to barotropic dynamics. Thermal wind transport is defined here as the difference between total and bottom transport, so that

$$\begin{aligned} T_{\mathrm{tw}}(t) &= T_{\mathrm{ACC}}(t) - T_{\mathrm{b}}(t), \\ &= \iint \Big(u_x(t, y, z) - u_b(t, y)\Big)\ \mathrm{d}y\mathrm{d}z. \end{aligned} \tag{3.5}$$

Thermal wind transport is usually the transport referred to in the context of eddy saturation.

The area-averaged depth integrated kinetic energy is defined as

$$\mathrm{K}(t) = \frac{1}{L_x L_y} \iiint \mathrm{KE}(t, x, y, z)\ \mathrm{d}x\mathrm{d}y\mathrm{d}z, \tag{3.6}$$

where KE is the kinetic energy density. This diagnostic is used in the eddy parameterising and eddy resolving configurations in Chapter 6. This quantity is volume integrated kinetic energy divided by the area. $K(t)$ is referred to as depth integrated kinetic energy.

3.3 Frequency analysis

Any physical signal in time (or space) can be decomposed into a spectrum of frequencies. Frequency analysis is used to predict and detect periodic trends and underlying processes which may not be obvious from only analysing the time series. This approach is used widely across many fields. Musical notes for example, can be broken down into pitch and timbre, both of which are easily determined through frequency analysis. On the other hand, oceanic tides can be shown to respond to astronomical forcing with frequency analysis. Broadly speaking, frequency analysis is a tool used to explain how a system responds to external forces (Boashash, 2016).

The Fourier transform decomposes a time-domain signal into complex sinusoids. At each frequency, the magnitude gives the amplitude of the complex sinusoid at the associated frequency. The phase shift can also be computed for each frequency. Letting $x(t)$ be a signal in the time domain, the Fourier transform is defined:

$$\tilde{x}(\omega) = \int_{-\infty}^{\infty} \mathrm{e}^{-i\omega t} x(t) \mathrm{d}t, \tag{3.7}$$

where ω is the temporal frequency. When plotted against frequency, the magnitude peaks of the Fourier transform indicate dominant frequencies. For example, a cosine with a period of 1 second will have a magnitude peak at $1\mathrm{Hz}$. Furthermore, the magnitude will be zero for frequencies that are not present in the signal. In bulk diagnostics, it is expected that strong peaks coincide with the forcing frequency.

3.3.1 The response function

In subsequent chapters of this thesis, wind stress magnitude oscillations are treated as an external force applied to a system. Resulting diagnostics are therefore a response to the force. Response theory is used in order to fully characterise these systems (Blundell and Blundell, 2010). Response theory answers the overarching question: how does a system react to external influences? In a circumpolar channel model: how do transport and energy respond to surface wind stress oscillations?

In linear response theory, it is assumed that the force is a small perturbation away from the original system and the responses are assumed linear. To put this in equations, let a force, $f(t)$, which oscillates over time, be applied to the system. Then, the spatially average value of the responding diagnostic is defined by

$$< x(t) >= \int_{-\infty}^{\infty} \chi(t-t')f(t')\mathrm{d}t'. \tag{3.8}$$

The response function is represented by $\chi(t-t')$. As the past does not change, $\chi(t-t') = 0$ for $t < t'$. For this to be practically useful, the Fourier transform along with the convolution theorem is applied so that:

$$< \tilde{x}(\omega) > = \tilde{\chi}(\omega)\tilde{f}(\omega). \tag{3.9}$$

We solve for $\tilde{\chi}(\omega)$, which is complex and has the form,

$$\tilde{\chi}(\omega) = \mathrm{Re}\chi(\omega) + i\mathrm{Im}\chi(\omega). \tag{3.10}$$

To compute the response function, we use the fast Fourier transform (FFT).

For bulk diagnostic $D(t)$, this is practically defined

$$\tilde{\chi}(\omega) = \frac{\mathrm{FFT}[D(t)]}{\mathrm{FFT}[\tau_{\mathrm{m}}(\mathrm{t})]}. \tag{3.11}$$

The denominator, $\tau_m(t)$ gives the maximum wind stress value for a given time. After analysing the results of a set of experiments, it is then straightforward to take the magnitude and phase of this complex value to form a response curve.

3.3.1.1 Example: The damped harmonic oscillator

To best illustrate the response function a pedological example is given (Blundell and Blundell, 2010). Consider the damped harmonic oscillatory with an external driving force, $f(t)$. This satisfies the equation of motion,

$$\ddot{x}(t) + \eta\dot{x}(t) + \omega_0^2 x(t) = f(t), \tag{3.12}$$

where ω_0^2 is the resonant frequency and η is the damping. Applying the Fourier transform of the linear response function ($\tilde{\chi}(\omega) = \frac{\tilde{x}(\omega)}{\tilde{f}(\omega)}$) yields

$$\tilde{\chi}(\omega) = \frac{1}{\omega_0^2 - \omega^2 + i\eta\omega}, \tag{3.13}$$

which is composed of a real and imaginary components. The magnitude of the response function is computed by taking the amplitude of the complex $\tilde{\chi}$. The phase shift is computed by $\arctan(\mathrm{Im}\chi/\mathrm{Re}\chi)$, which gives the relationship between the phase of the output and input signals. "Resonance" occurs when $\omega = \omega_0$; at this frequency, the response function is at a maximum and the external forcing matches the system's natural frequency.

3.3.1.2 Previous methodology

The frequency analysis used in this thesis builds on work completed in Sinha and Abernathey (2016). Their work focuses on forcing timescales in the Southern Ocean and their relationship to eddy saturation. To characterise the response of the system to oscillatory forcing, they use what they term "composite analysis" in order to compute the gain (referred to as "response magnitude" in this thesis) and phase angle of diagnostics against oscillatory wind stress. The gain is defined as the root-mean-square of the diagnostic. To accomplish this, the composite average is first computed by averaging together the diagnostics from each cycle and subtracting the mean. The composite average is useful in seeing the average behaviour of a diagnostic across one cycle, although one must be aware that this can hide non-linear responses in the system. Unlike the response magnitude determined through Fourier transforms, the gain is always real. This however means that the phase cannot be determined from the gain.

This thesis uses an improved method of determining phase. To determine phase, Sinha and Abernathey (2016) use lag correlation analysis. The lag correlation is computed for each cycle of data (minus the mean of the entire diagnostic) against the corresponding wind stress, which completes one full cycle over this period. Each lag correlation is converted into phase and then arithmetically averaged together, forming the phase for each oscillation experiment. However, the space of phase shifts is not a vector space, as it is periodic and hence, there is no way to define an arithmetic average. To illustrate this, consider two phase values, $-\pi$ and $\pi - 1 \times 10^{-10}$. Correctly averaging these phases should yield approximately π, not approximately 0. It is clear from this simple example that arithmetically averaging the phase can give misleading results. Therefore, this method is not used in this thesis. Instead, phase is taken directly from the complex response function.

This method can work for some specific cases. For instance, given a forcing signal that oscillates with period P and a regular diagnostic that lags the forcing by a single timestep, this method will return a true result. Nevertheless, this is more by chance rather than rigour. It is important to note that while lag correlation analysis is not the correct approach for response functions, it is a useful method in the time domain when comparing periodic diagnostics over many cycles (Baldocchi and Meyers, 1988; Qiu et al., 2014).

4 | A dynamical system of eddy saturation across timescales

Eddy resolving models of the Southern Ocean suggest that this region is eddy saturated. That is, thermal wind transport in high resolution models is insensitive to changes in the mean surface wind stress magnitude. Eddy saturation is not a feature of all models, as many eddy parameterised models do not lead to transport insensitivity. One such parameterisation scheme that often fails to capture eddy saturation is the Gent-McWilliams scheme (GM) (Gent and McWilliams, 1990; Gent et al., 1995). This scheme represents the response of the mesoscale eddy field through an eddy induced overturning in order to oppose the source of baroclinic instability–the steepening density gradients. Building from GM, the GEOMETRIC parameterisation scheme does however result in eddy saturation for the zonally averaged and three-dimensional cases (Mak et al., 2017; Mak et al., 2018). These parameterisation schemes are discussed in greater detail in Chapter 2.

Most of the literature on eddy saturation focuses on the equilibrated transport sensitivity to changes in the mean surface wind. However, the response of the ACC to time varying wind fluctuations on top of the mean surface wind stress may be important in fully understanding eddy saturation. Eddy saturation on equilibrated timescales is controlled by baroclinic processes. Barotropic processes, which operate on faster timescales than baroclinic processes, are usually not considered in the context of equilibrated eddy saturation. It is not clear if these faster processes play a role in transient and equilibrated eddy saturation or the adjustment of the ACC, hence they cannot safely be ignored.

Reduced-order simple models can be crucial in understanding key processes in a system, especially when time evolution is of interest. In Ambaum and Novak (2014), a two-variable reduced order model is put forth to describe atmospheric storm track variability. This model describes the interaction of baroclinicity and baroclinic eddies, which results in a non-linear oscillator. This oscillatory behaviour is rooted in the conflicting relationship between the growth of baroclinicity and the growth of the mesoscale eddy field. Analysis then yields a timescale for eddy growth. This model has dynamically similar mechanisms to GEOMETRIC models (e.g., Mak et al. (2017), Marshall et al. (2017), Maddison et al. (2023)). It is therefore reasonable to expect inherent oscillations in reduced order GEOMETRIC models with fluctuating wind stress. Like atmospheric storm tracks, eddy saturation in the ACC is also the consequence of a precarious balance between the source of eddy energy and mesoscale eddying. The application of a fluctuating wind stress may upset this balance, causing oscillations.

This chapter extends the model described in Maddison et al. (2023). This model is a simple dynamical system that captures the key elements of equilibrated eddy saturation as described in Marshall et al. (2017). Close attention is paid to the Antarctic Circumpolar Current transport and eddy energetics in an oscillatory forced experimental setup. This model uses the GEOMETRIC form of the Gent-McWilliams eddy parameterisation with an integrated eddy energy budget. To extend this model, a time-dependent oscillatory wind stress is imposed on the system. This is briefly introduced within Maddison et al. (2023), but this chapter provides further details and background of the findings. Finally, the stratification is generalised and compared to the assumed linear stratification profile originally put forth in this model. Original work contributed to Maddison et al. (2023) by Maurer-Song is put forth in Sections 4.2 and 4.4. This contribution focussed on the addition of a time-dependent wind stress forcing and subsequent analysis.

4.1 Summary of the time-independent wind stress model

The following describes the dynamical framework of Maddison et al. (2023) and its key results when time-independent wind forcing is applied. This models a zonally periodic channel, $(y, z) \in [0, L_y] \times [-H, 0]$, with a linearly varying density profile in z and y (up to the addition of a constant) :

$$\rho(y, z, t) = -\frac{\rho_0}{g} m(t) y - \frac{\rho_0}{g} N_0^2 z. \tag{4.1}$$

Here ρ_0 is constant background reference density, g is the gravitational acceleration magnitude, and N_0 is the buoyancy frequency, all assumed to be constants. Thermal wind balance on an $f-$plane leads to the following equation for mean thermal wind transport, where mean refers to averaging in space:

$$T(t) = -\frac{1}{2} L_y H^2 \frac{1}{f_0} m(t), \tag{4.2}$$

where f_0 is the Coriolis parameter and thermal wind transport is solely a function of time (t). Rewriting Eq.(4.1) in terms of thermal wind transport leads to

$$\rho(y, z, t) = 2 \frac{1}{L_y H^2} \frac{f_0 \rho_0}{g} y T(t) - \frac{\rho_0}{g} N_0^2 z. \tag{4.3}$$

In this framework, zero flow is assumed at the base. To determine an equation for mean transport over time, the mean density equation in this channel is considered:

$$\frac{\partial \rho}{\partial t} + \frac{\partial}{\partial y}\Big((v_{mean} + v_{eddy})\rho\Big) + \frac{\partial}{\partial z}\Big((w_{mean} + w_{eddy})\rho\Big) = 0. \tag{4.4}$$

This is then multiplied by gy and integrated, leading to

$$\frac{d}{dt}\int_0^{L_y}\int_{-H}^0 \rho g y \,\mathrm{d}z\mathrm{d}y = \int_0^{L_y}\int_{-H}^0 (v_{mean} + v_{eddy})\rho g \,\mathrm{d}z\mathrm{d}y, \tag{4.5}$$

where no-normal-flow boundary conditions are assumed. For the density profile given by Eq.(4.3),

$$\frac{d}{dt}\int_0^{L_y}\int_{-H}^0 \rho g y \,\mathrm{d}z\mathrm{d}y = \frac{2}{3}\frac{L_y^2}{H} f_0 \rho_0 \frac{dT}{dt}. \tag{4.6}$$

The planetary geostrophic mean zonal momentum equation states that

$$-f_0 v_{mean} = F - D, \tag{4.7}$$

where F is mean zonal momentum forcing and D is dissipation. It is assumed that the surface wind stress forcing is balanced by a bottom form stress of opposite but equal magnitude at depth. Therefore,

$$-\int_0^{L_y}\int_{-H}^0 f_0 v_{mean}\rho \,\mathrm{d}z\mathrm{d}y = \frac{\tau_0}{\rho_0}\int_0^{L_y}\int_{-H}^0 [\delta(z) - \delta(z+H)]\rho \,\mathrm{d}z\mathrm{d}y, \tag{4.8}$$

where τ_0 is the surface wind stress forcing. Applying the density profile (Eq.(4.3)) gives

$$\int_0^{L_y}\int_{-H}^0 v_{mean}\rho g \,\mathrm{d}z\mathrm{d}y = L_y H \frac{N_0^2}{f_0}\tau_0. \tag{4.9}$$

The eddy-induced transport velocity is reformulated in terms of the eddy transport streamfunction (ψ) so that

$$v_{eddy} = \frac{\partial \psi}{\partial z}, \tag{4.10}$$

which leads to

$$\int_0^{L_y}\int_{-H}^0 v_{eddy}\rho g \,\mathrm{d}z\mathrm{d}y = \int_0^{L_y}\int_{-H}^0 \frac{\partial \psi}{\partial z}\rho g \,\mathrm{d}z\mathrm{d}y, \tag{4.11}$$

$$= -g\int_0^{L_y}\int_{-H}^0 \psi\frac{\partial \rho}{\partial z}\mathrm{d}y\mathrm{d}z. \tag{4.12}$$

Boundary conditions are applied so that $\psi = 0$ on boundaries. Gent-McWilliams is used to define the eddy transport streamfunction (Gent and McWilliams, 1990; Gent et al., 1995),

$$\psi = \kappa_{GM}\frac{\partial \rho}{\partial y}\left(\frac{\partial \rho}{\partial z}\right)^{-1}. \tag{4.13}$$

For the mean density profile (4.3) and assuming that κ_{GM} is spatially constant,

$$\int_0^{L_y}\int_{-H}^0 v_{eddy}\rho g \,\mathrm{d}z\mathrm{d}y = -2\frac{1}{H}f_0\rho_0\kappa_{GM}T. \tag{4.14}$$

Putting these components together leads to an equation for the mean thermal wind transport:

$$\frac{dT}{dt} = \frac{3}{2}\frac{H^2}{L_y}\frac{N_0^2}{f_0^2}\frac{\tau_0}{\rho_0} - 3\frac{1}{L_y^2}\kappa_{GM}T. \tag{4.15}$$

This gives a model for mean transport as parameterised by standard Gent-McWilliams if κ_{GM} is set to a constant value. If this was the completed model, there would be no eddy saturation. If constant κ_{GM} were used, then the steady-state transport scales with wind stress (Munday et al., 2013). It is noted that Eq.(4.15) follows on from Gnanadesikan (1999), which models Southern Ocean pycnocline depth (h) through flux balance. This model is also time dependent, but does not result in depth insensitivity to wind stress due to the representation of the eddying contributions.

In order to obtain a model for eddy saturation, Eq.(4.15) must use the reformulated κ_{GM} as defined in GEOMETRIC. GEOMETRIC defines the eddy transfer coefficient,

$$\kappa_{GM} = \alpha E \frac{N_0}{m}, \tag{4.16}$$

where $|\alpha| \leq 1$ is a constant and m is set by the magnitude of the horizontal density gradient. In this framework,

$$m(t) = -\frac{2T(t)f_0}{L_y H^2}. \tag{4.17}$$

In order to model southern hemispheric conditions, it is assumed that f_0 is negative. It is also assumed that $f_0 T(t)$ is negative. Were this term assumed positive, this would permit thermal wind reversal with baroclinic stability. Using integrated eddy energy ($\mathcal{E} = \int_0^{L_y} \int_{-H}^{0} \rho_0 E \,\mathrm{d}z\mathrm{d}y$), the eddy transfer coefficient can be rewritten as

$$\kappa_{GM} = -\frac{1}{2}\alpha \frac{H}{L_x} \frac{N_0}{f_0 \rho_0} \frac{\mathcal{E}}{T}. \tag{4.18}$$

GEOMETRIC provides a depth-integrated total eddy energy budget (Mak et al., 2017). With further simplifications made for this model, this is given by

$$\frac{d\mathcal{E}}{dt} = -L_x \int_0^{L_y} \int_{-H}^{0} g\kappa_{GM} \Big(\frac{\partial \rho}{\partial y}\Big)^2 \Big(\frac{\partial \rho}{\partial z}\Big)^{-1} \mathrm{d}z\mathrm{d}y - \lambda\mathcal{E} + \lambda\mathcal{E}_0, \tag{4.19}$$

where $\mathcal{E}_0$ is the background eddy energy and λ is the eddy energy dissipation rate.

Putting together both the transport equation and the eddy energy budget leads to a coupled system of ordinary differential equations:

$$\frac{dT}{dt} = \frac{3}{2}\frac{H^2}{L_y}\frac{N_0^2}{f_0^2}\Big[\frac{\tau_0}{\rho_0} + \alpha \frac{f_0}{N_0}\frac{\mathcal{E}}{\rho_0 L_x L_y H}\Big], \tag{4.20}$$

$$\frac{d\mathcal{E}}{dt} = \Big[-2\alpha \frac{1}{L_y H^2}\frac{f_0}{N_0} T - \lambda\Big]\mathcal{E} + \lambda\mathcal{E}_0. \tag{4.21}$$

With constant wind forcing in time and space, this system of equations has an oscillatory timescale that is inherent to the system. This is given by

$$\begin{aligned} t_{1\mathrm{D}} &= \frac{2\pi}{\sqrt{3}}\sqrt{-\frac{1}{\alpha}L_y^2\frac{f_0}{N_0}\frac{\rho_0}{\tau_0}} \\ &= \frac{2\pi}{\omega_{1\mathrm{D}}} \end{aligned} \tag{4.22}$$

where $\mathcal{E}_0$ is assumed to be 0. This is an inherent oscillatory timescale associated with GEOMETRIC. For the chosen parameters shown in Table 4.1, this gives an inherent oscillatory timescale of approximately 9.7 years, where one year is 360 days. It is not yet clear if this oscillation timescale has a real world equivalent, or if it is purely associated with this parameterisation.

The dynamical system given in Eqs.(4.20) and (4.21) can be rewritten in terms of mean thermal wind shear ($S = T/LH^2$) rather than transport. Assuming $\mathcal{E}_0 = 0$ for simplicity, this leads to

$$\frac{dS}{dt} = \frac{3}{2}\frac{1}{L_y^2}\frac{N_0^2}{f_0^2}\left[\frac{\tau_0}{\rho_0} - \alpha\frac{f_0}{N_0}\frac{\mathcal{E}}{\rho_0 L_x L_y H}\right], \tag{4.23}$$

$$\frac{d\mathcal{E}}{dt} = -2\alpha\frac{f_0}{N_0}\mathcal{E}S - \lambda\mathcal{E}. \tag{4.24}$$

Using this form of the system allows for a clearer look at what sets the angular frequency of oscillation, $\omega_{1\mathrm{D}}$. This frequency is the product of the mean shear production and the eddy energy efficiency. The mean shear generation is due to the wind stress, which forces Eulerian overturning, whereas the efficiency is for a given eddy energy and the mean vertical shear:

$$\omega_{1\mathrm{D}}^2 = \underbrace{\frac{3}{2}\frac{1}{L_y^2}\frac{N_0^2}{f_0^2}\frac{\tau_0}{\rho_0}}_{\text{Mean shear production due to wind}} \times \underbrace{-2\alpha\frac{f_0}{N_0}}_{\text{Energy conversion efficiency}}. \tag{4.25}$$

The timescale of oscillation varies inversely with the square roots of wind stress

Parameter	Value	Description
L_y	2000 km	meridional length
H	3500 m	depth
τ_0	$0.2\ \mathrm{N/m^2}$	surface wind stress magnitude
λ	$3\times10^{-8}\ 1/s$	eddy energy dissipation rate
f_0	-1.11×10^{-4}	Coriolis parameter
ρ_0	$1028\ \mathrm{kg/m^3}$	reference density
α	0.1	eddy efficiency parameter
g	$10\ \mathrm{m}/s^2$	gravitational acceleration
N_0	$-30f_0$	buoyancy frequency

Table 4.1: Model parameters in the dynamical system for ACC-like results.

(τ_0) and α, and is independent of eddy energy dissipation, λ. Instead, the dissipation sets transport magnitude in the steady state and is responsible for changing mean thermal wind shear. Therefore, the oscillation timescale is set by the interaction between overturning mechanisms: wind driven Eulerian overturning and eddy driven (baroclinic) overturning.

4.2 Oscillatory wind stress forcing

The constant wind stress, τ_0, is redefined to vary sinusoidally in time. This is accomplished by replacing τ_0 with $\tau_0(1+\epsilon\sin(2\pi t/P))$ where P is the period of forcing and ϵ sets the wind stress magnitude change. This is applied to the system given by Eqs.(4.20) and (4.21):

$$\frac{d}{dt}\begin{bmatrix} T \\ \mathcal{E} \end{bmatrix} = \begin{bmatrix} 0 & \frac{3}{2}\frac{H^2}{L_y}\frac{N_0}{f_0}\frac{\alpha}{\rho_0 L_x L_y H} \\ 0 & -\lambda \end{bmatrix}\begin{bmatrix} T \\ \mathcal{E} \end{bmatrix} + \begin{bmatrix} \frac{3}{2}\frac{H^2}{L_y}\frac{N_0^2}{f_0^2}\frac{\tau_0}{\rho_0} \\ -\frac{2f_0\alpha}{N_0 L_y H^2}T\mathcal{E} + \lambda\mathcal{E}_0 \end{bmatrix} + \begin{bmatrix} \frac{3\epsilon}{2}\frac{H^2}{L_y}\frac{N_0^2}{f_0^2}\frac{\tau_0}{\rho_0}\sin(2\pi t/P) \\ 0 \end{bmatrix}. \tag{4.26}$$

This system is the sum of linear, non-linear, and time-dependent components. There are fixed points at

$$T_{tw}^* = -\frac{1}{2}\frac{L_y N_0 H^2}{\alpha f_0}\Big(\lambda - \lambda\frac{\mathcal{E}_0}{\mathcal{E}^*}\Big), \tag{4.27}$$

$$\mathcal{E}^* = -\frac{N_0 \tau_0 H L_y L_x}{\alpha f_0}. \tag{4.28}$$

This system is solved in two different ways. First, the linearised solution is found, which gives an explicit–albeit linearised–solution to the system. Next, the system is solved numerically with the third-order Adams-Bashforth scheme. In both case, $\epsilon = 0.1$ (10% wind magnitude change) is used. This weak forcing is used in order to maintain stability in the linearised solution.

4.2.1 The linearised solution

A reduced and simplified model is advantageous as it can be directly solved for in its linearised form. Solving directly for $T(t)$ and $\mathcal{E}(t)$ in this form can further explain how the linearised system responds to oscillatory surface forcing.

At the fixed point given by Eqs.(4.27) and (4.28), the corresponding linearised system is

$$\frac{d}{dt}\begin{bmatrix} T - T^* \\ \mathcal{E} - \mathcal{E}^* \end{bmatrix} = \begin{bmatrix} 0 & \frac{3}{2}\frac{H N_0 \alpha}{L_y^2 L_x f_0 rho_0} \\ \frac{2 L_x \tau_0}{H} & -\lambda - 2\alpha\frac{f_0 T^*}{L_y H^2} \end{bmatrix} \begin{bmatrix} T - T^* \\ \mathcal{E} - \mathcal{E}^* \end{bmatrix}. \tag{4.29}$$

The general solution is of the form

$$\begin{bmatrix} T - T^* \\ \mathcal{E} - \mathcal{E}^* \end{bmatrix} = c_0 \mathbf{v_0} \mathbf{e}^{\Lambda_0 t} + c_1 \mathbf{v_1} \mathbf{e}^{\Lambda_1 t}, \tag{4.30}$$

where the eigenvalues ($\Lambda_{0,1}$) and the eigenvectors ($\mathbf{v}_{0,1}$) are the eigenvalues and eigenvectors of the matrix in the linearised system, and c_0 and c_1 are constants. The eigenvalues and eigenvectors are defined

$$\Lambda_k = -\frac{\lambda \mathcal{E}_0}{2\mathcal{E}^*} + (-1)^k \mathrm{i}\sqrt{\omega_{1D}^2 - \frac{4\mathcal{E}^*}{\lambda^2 \mathcal{E}_0}}, \tag{4.31}$$

$$\mathbf{v}_k = \begin{bmatrix} \frac{\omega_{1D}^2}{\lambda^2} \\ -\Lambda_k \end{bmatrix} \tag{4.32}$$

for $k = 0, 1$. At this stage, the time dependent oscillatory changes have been neglected. To include the time dependent forcing, the following particular solution is proposed:

$$\begin{bmatrix} T_p(t) \\ \mathcal{E}_p(t) \end{bmatrix} = \begin{bmatrix} A\cos(2\pi t/P) + B\sin(2\pi t/P) + T^* \\ D\cos(2\pi t/P) + F\sin(2\pi t/P) + \mathcal{E}^* \end{bmatrix}, \tag{4.33}$$

where A, B, D, F are constants solved for using the initial values for transport and eddy energy.

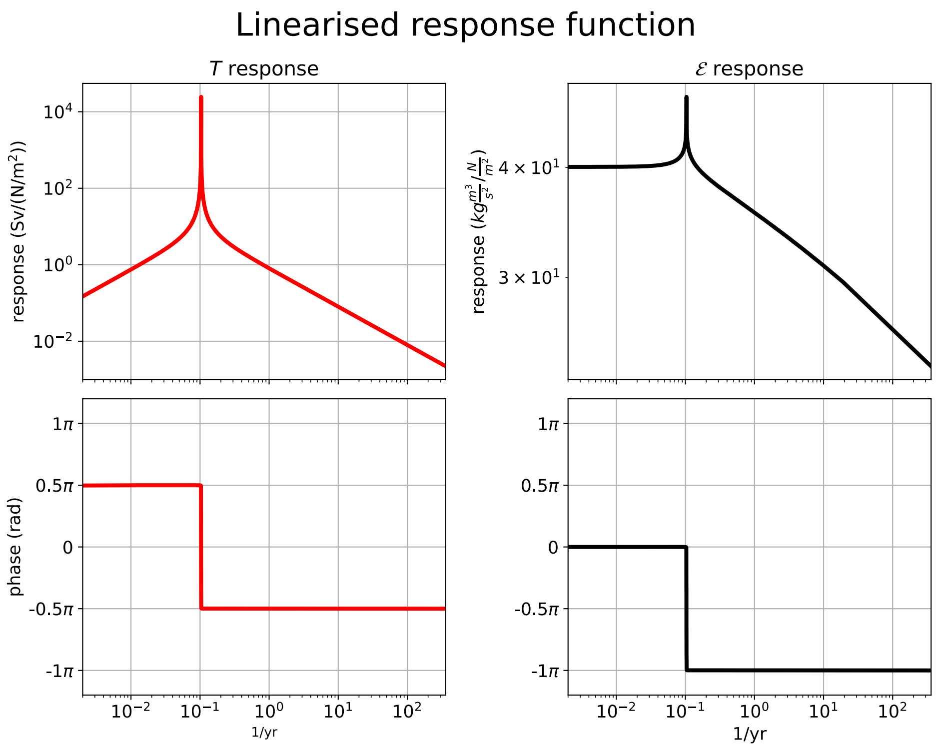

Figure 4.1: The response function for the linearised solution is shown. Magnitude (top) and phase (bottom) are plotted for transport (left) and eddy energy (right). There is a peak in both response magnitudes which coincides with a phase shift. The thermal wind transport lags the wind forcing by $\pi/2$ and the eddy energy response is out of phase with the wind forcing for frequencies greater than ω_{1D}. The thermal wind transport leads the wind forcing by $\pi/2$ and the eddy energy response is in phase with the wind forcing for frequencies less than ω_{1D}.

Rather than explicitly solving the system in the time domain for a sample of forcing frequencies, it is more useful to solve the system fully in the frequency domain. The solution in the frequency domain is shown in Fig. 4.1. The response magnitude is straightforward to compute when an explicit solution is attainable.

The response function magnitude is computed from the particular solution,

$$T_{\text{response}}(\omega) = \sqrt{A^2 + B^2}, \tag{4.34}$$

$$\mathcal{E}_{\text{response}}(\omega) = \sqrt{D^2 + F^2}, \tag{4.35}$$

where $A, B, D,$ and F vary for different frequencies.

4.2.2 Adams-Bashforth method

The third-order Adams-Bashforth method is an explicit method prescribed by:

$$D_{n+3} = D_{n+2} + \Delta t\Big(\frac{23}{12}f(t_{n+2}, D_{n+2}) - \frac{16}{12}f(t_{n+1}, D_{n+1}) + \frac{5}{12}f(t_n, D_n)\Big), \tag{4.36}$$

and

$$f(t_n, D_n) = D_n'. \tag{4.37}$$

where D_k is the diagnostic of interest (in this case, either transport or eddy energy), Δt is the chosen timestep, and t_k is the time at iteration k (Butcher, 2016). For numerical stability, $\Delta t = 43200\ s$ (equivalent to half a day) is used. As we are interested in the behaviour when a time-varying wind stress is imposed on the system, the fixed points of the homogeneous system are used as initial diagnostic values for transport and eddy energy (as defined in Eqs.(4.28) and (4.27)). This is equivalent to running the non-oscillatory wind stress model to equilibration.

Results in the time domain are shown in Fig. 4.2. This shows results for when $P = 1$ year as an illustrative example. By inspection, both diagnostics oscillate at two different frequencies. In both, the higher frequency oscillation follows the forcing frequency. This is particularly clear in the transport time series, where the high frequency oscillation is more significant. There is also evidence for a longer frequency of about 0.1 years^{-1} which is clear in both diagnostics. Translating the time series to the frequency domain (not shown), it is clear that this system oscillates at both 1 years^{-1} and approximately $\frac{1}{9.7}$ years^{-1} (which is equivalent to $\omega_{1D} = t_{1D}^{-1}$). Fig. 4.3 shows the same results for a $P = 1$ year forcing, but with a low-pass filtered applied to frequencies greater than or equal to 1 years^{-1}. This further highlights the lower frequency resonance inherent to the system, as the diagnostics oscillate only about the decadal frequency. For all forcing frequencies sufficiently far from the inherent oscillatory frequency of the system, both diagnostics exhibit oscillations of both the forcing and resonant frequency. When the system is forced with $P \approx 9.7$ years, the system approaches resonant instability. This could be bypassed by solving the system for a sufficiently long time or increasing the background eddy energy. However, this is not necessary for the scope of this thesis.

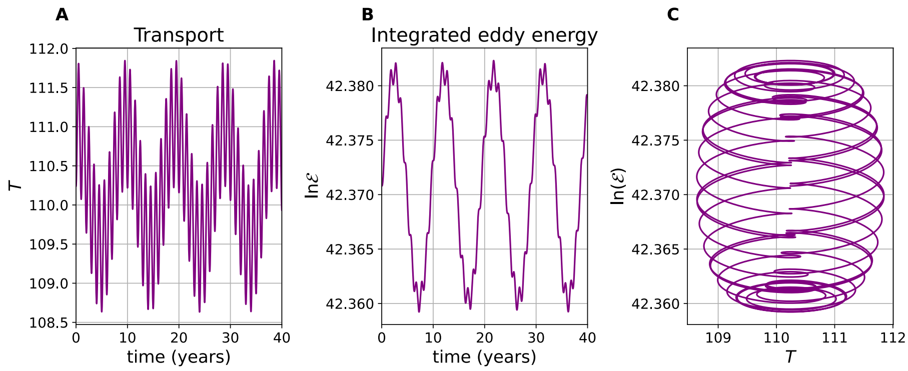

Figure 4.2: The system is solved using Adams-Bashforth third order with an oscillatory forcing period of 1 year. Time series are shown for (a) transport (Sv) and (b) integrated eddy energy (kg m^3/s^2). A phase portrait plotting transport against integrated eddy energy is shown in (c).

Fig. 4.3 also illustrates the cyclical behaviour of the system linked with the growth and decay of baroclinicity. As baroclinic instability grows, there is an initial growth in eddy energy. This growth further leads to large eddy form stress, which acts to reduce the transport. However, when shear is sufficiently low, the flow returns to a state of baroclinic stability. This then eventually leads to a decay in eddy energy. This behaviour cycles with the oscillatory wind stress perturbation, and is reminiscent of Ambaum and Novak (2014).

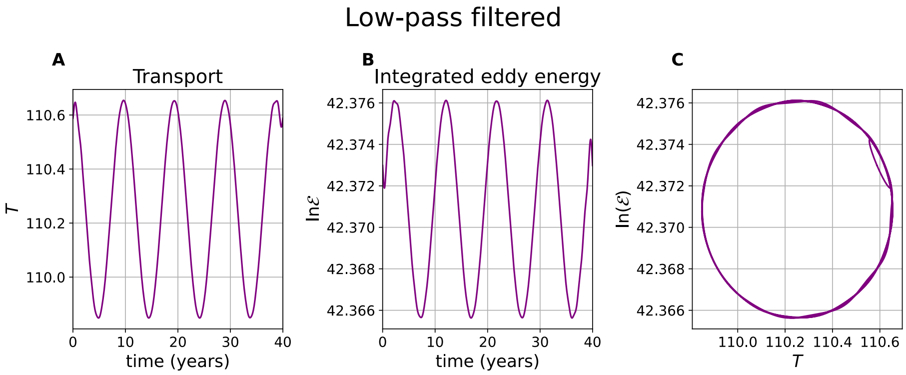

Figure 4.3: A low-pass filter is applied to the data shown in Fig. 4.2. Thermal wind transport and integrated eddy energy only oscillate at the decadal frequency, which suggests an inherent oscillatory timescale associated with the system regardless of the period of oscillatory wind forcing.

Instead of analysing discrete Fourier transforms for each perturbation frequency, the response function is far more useful in this circumstance as it can fully characterise the system. This is shown in Fig. 4.4 for transport and integrated eddy energy. The transport and energy response magnitudes both have prominent peaks at the resonant frequency of $\frac{1}{9.7}$ years^{-1}. In the frequency domain, the driven harmonic oscillator has a singular peak at the resonant frequency. It is therefore concluded that when solved with this method, both transport and eddy energy have response magnitudes that peak at the inherent GEOMETRIC oscillatory timescale. A notable difference between the two responses is at low frequencies. After peaking, the transport response rapidly decreases before equilibrating, whereas the eddy energy response equilibrates without a dramatic decrease. The phase also shifts at the resonant frequency.

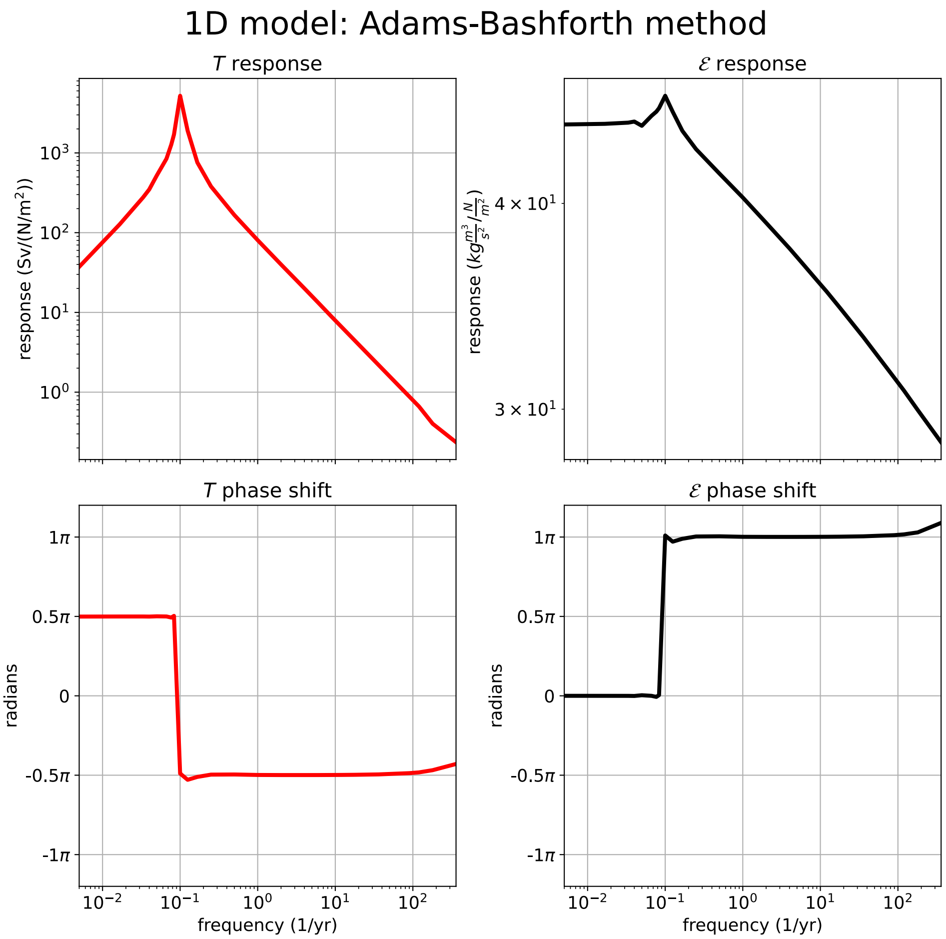

Figure 4.4: The response function magnitude (a,b) and phase (c,d) of transport (left) and eddy energy (right) from the numerical solution. Again, peaks in the magnitude of the response coincide with phase shifts. The thermal wind transport lags the wind forcing by $\pi/2$ and the eddy energy response is out of phase with the wind forcing for frequencies greater than ω_{1D}. The thermal wind transport leads the wind forcing by $\pi/2$ and the eddy energy response is in phase with the wind forcing for frequencies less than ω_{1D}.

Like in the linearised solution, the response for both transport and eddy energy peaks at the approximate resonant frequency inherent to the system. The linearised solution has sharper peaks, but this is due to the increased sampling available in this system, as computing the linearised solution is computationally cheaper. The multistep method requires separate experiments to first run before computing the response whereas the linearised system gives an expression for the response at each frequency.

The phase of both diagnostics is consistent across methods. For $\omega < \omega_{1D}$, the transport response leads the wind forcing by $\pi/2$ and the eddy energy response is in phase with the forcing. This behaviour changes at the oscillation frequency, as the transport response lags by $\pi/2$ and eddy energy is π out of phase with the forcing for $\omega > \omega_{1D}$.

The response function of the one-dimensional standard linear oscillator peaks only at the resonant frequency. This response frequency peak depends only on the steady state solution, whereas the general solution is a sum of the transient solution. That is, the transient response is the response of the system to a change from the steady state. The dynamical system's solution takes the form of the standard linear oscillator. The response peaks lie at the resonant frequencies, and the transient adjustment is encoded within the rest of the response curves.

4.3 Non-dimensionalisation

It is useful to non-dimensionalise the system given in Eqs.(4.20) and (4.21) as non-dimensionalisation can reveal characteristic properties of a system. It is particularly useful in showing key information about intrinsic resonance. Transport, eddy energy, and time are non-dimensionalised by:

$$T = -\frac{1}{2}\frac{L_y N_0 H^2}{\alpha f_0}\lambda\tilde{T}, \tag{4.38}$$

$$\mathcal{E} = \mathcal{E}^*\tilde{\mathcal{E}}, \tag{4.39}$$

$$\mathcal{E}_0 = \mathcal{E}^*\tilde{\mathcal{E}}_0, \tag{4.40}$$

$$t = \frac{1}{\lambda}\tilde{t}, \tag{4.41}$$

where $\mathcal{E}^*$ is the aforementioned fixed point of eddy energy.

This leads to the non-dimensional form of Eqs.(4.20) and (4.21):

$$\frac{d\tilde{T}}{d\tilde{t}} = F(1-\tilde{\mathcal{E}}), \tag{4.42}$$

$$\frac{d\tilde{\mathcal{E}}}{d\tilde{t}} = \tilde{T}(\tilde{\mathcal{E}}-1) + \tilde{\mathcal{E}}_0, \tag{4.43}$$

where F is a non-dimensional parameter,

$$F = -3\alpha\frac{1}{L_y^2}\frac{N_0}{f_0}\frac{\tau_0}{\rho_0}\frac{1}{\lambda^2} = \frac{\omega_{1D}^2}{\lambda^2}. \tag{4.44}$$

This is equivalent to the square of the non-dimensionalised angular frequency.

4.3.1 Hamiltonian form

The non-dimensionalised system given in Eqs.(4.42) and (4.43) can be further recast by letting $\tilde{M} = \ln\tilde{\mathcal{E}}$ and $\tilde{\mathcal{E}}_0 = 0$. This leads to the form:

$$\frac{d\tilde{T}}{d\tilde{t}} = F(1-\mathrm{e}^{\tilde{M}}), \tag{4.45}$$

$$\frac{d\tilde{M}}{d\tilde{t}} = \tilde{T} - 1. \tag{4.46}$$

This form is dynamically similar to Eqs.(6) in Ambaum and Novak (2014). In their model for baroclinic storm tracks, it is assumed that the eddy heat flux scales with the square of eddy amplitude. GEOMETRIC adapts the standard GM coefficient to scale with eddy energy, thus resulting in this similarity. This system can be further transformed into the Hamiltonian,

$$\mathcal{H}(\tilde{T}, \tilde{M}) = \frac{1}{2}(\tilde{T} - 1)^2 + F(\mathrm{e}^{\tilde{M}} - \tilde{M} - 1). \tag{4.47}$$

This is non-negative and vanishes only at the fixed point.

The Hamiltonian corroborates the growth-decay cycle inherent to this system. Starting from low transport and low energy leads to a growth in transport as the Eulerian overturning increases without much opposition from the eddy field. However, at sufficiently high shear there is also sufficiently high baroclinicity for the eddy energy to counteract the Eulerian overturning. This leads to an erosion of the shear, which fuels the eddy energetics. This decrease in shear cannot sustain sufficient baroclinicity for eddy energy generation, causing a drop in eddy energy as a result of the drop in transport. This behaviour is illustrated in Fig. 4.5, which shows the contours of the Hamiltonian.

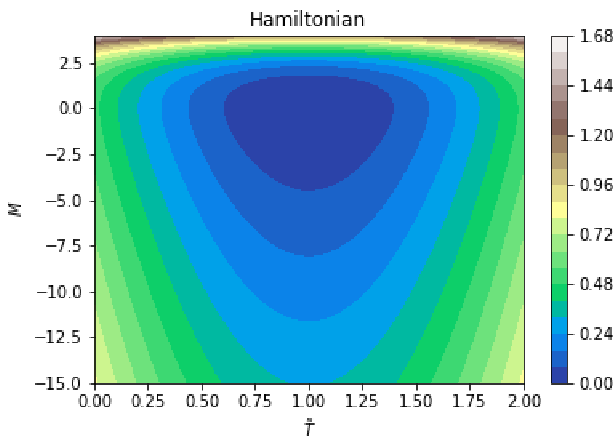

Figure 4.5: Hamiltonian for the system. Contours orbit anti-clockwise.

4.4 A generalised density profile

Maddison et al. (2023) assumes linear stratification in both y and z, however, this restrictive assumption is not applicable for more complex models. It is not clear what effects altering this linear profile will have on the results, especially in the frequency domain. In particular, the relationship between stratification and the oscillatory timescale is of great interest. To accomplish this, a new density profile is proposed. This profile allows for non-linear dependence on z. Using this profile, a new system of equations is determined and non-dimensionalised. An oscillatory timescale is computed and dynamical similarity is discussed.

4.4.1 General function of z

Let density (up to the addition of a constant) vary for some function of z so that

$$\rho(y, z, t) = 2\frac{1}{L_y H^2}\frac{f_0\rho_0}{g}yT(t) - \frac{\rho_0}{g}N_0^2 r(z), \tag{4.48}$$

for some function $r(z)$ such that $r(-H) = 0$ and $r(0) = 1$. To allow κ to vary in the vertical, let

$$E \longrightarrow ES(z), \tag{4.49}$$

where $S(z)$ is a function such that $|S(z)| \leq 1$, $|S(z)|_{\max} = 1$ and $S(z)_{min} \geq 0$. If κ were instead assumed spatially constant with a vertically varying stratification, this would lead to a strong assumption for a vertical structure of E, which is best avoided. Altering the energy budget in Mak et al. (2017) leads to (up to a constant of background eddy energy)

$$\frac{d}{dt}\iint ES(z)\mathrm{d}y\mathrm{d}z = -\iint \kappa\frac{g}{\rho_0}\left[\frac{\partial\rho}{\partial y}\right]^2\left[\frac{\partial\rho}{\partial z}\right]^{-1}\mathrm{d}y\mathrm{d}z - \lambda\iint ES(z)\mathrm{d}y\mathrm{d}z. \tag{4.50}$$

Instead of defining κ with integrated eddy energy ($\mathcal{E}$), instead let

$$\kappa = \alpha E S(z)\frac{N_0}{|m|} = -\frac{\alpha E S(z) N_0 L_y H^2}{2T f_0}. \tag{4.51}$$

Substituting the redefined κ into the eddy energy budget leads to,

$$\frac{d}{dt}E\int S(z)\mathrm{d}z = -\frac{2\alpha f_0 T E}{N_0 H^2 L_y}\int S(z)\left[\frac{dr}{dz}\right]^{-1}\mathrm{d}z - \lambda E\int S(z)\mathrm{d}z. \tag{4.52}$$

Likewise, the eddying component of the transport equation is altered so that

$$\frac{dT_{\text{eddy}}}{dt} = \frac{3}{2}\alpha\frac{HN_0}{f_0 L_y}E\int S(z)\mathrm{d}z, \tag{4.53}$$

where T_{eddy} represents transport from eddy velocities. This leads to the following system of equations:

$$\frac{dT}{dt} = \frac{3}{2}\frac{H}{L_y}\frac{N_0^2\tau_0}{f_0^2\rho_0} + \frac{3}{2}\alpha\frac{HN_0}{f_0 L_y}E\int S(z)\mathrm{d}z, \tag{4.54}$$

$$\frac{d}{dt}E\int S(z)\mathrm{d}z = -\frac{2\alpha f_0 T E}{N_0 H^2 L_y}\int S(z)\left[\frac{dr}{dz}\right]^{-1}\mathrm{d}z - \lambda E\int S(z)\mathrm{d}z + \lambda E_0, \tag{4.55}$$

with fixed point (T^*_{tw}, E^*)

$$E^* = -\frac{N_0\tau_0}{\alpha f_0\rho_0}\frac{1}{\int S(z)\mathrm{d}z}, \tag{4.56}$$

$$T^* = -\lambda\frac{(E^* - E_0)}{E_0}\frac{\int S(z)\mathrm{d}z}{\int S(z)[\frac{dr}{dz}]^{-1}\mathrm{d}z}\frac{N_0 H^2 L_y}{2\alpha f_0}. \tag{4.57}$$

Non-dimensionalisation leads to the familiar equations,

$$\frac{d\tilde{T}}{d\tilde{t}} = F_2(1 - \tilde{E}), \tag{4.58}$$

$$\frac{d\tilde{E}}{d\tilde{t}} = \tilde{E}(\tilde{T} - 1) + \tilde{E}_0, \tag{4.59}$$

for

$$F_2 = -3\alpha \frac{N_0 \tau_0}{L_y^2 f_0 \rho_0 \lambda^2} \times \frac{\int S(z)[\frac{dr}{dz}]^{-1} \mathrm{d}z}{H \int S(z) \mathrm{d}z}. \tag{4.60}$$

Like before, this is the non-dimensionalised angular frequency, and should be compared with F from Eq.(4.44). It is clear that the new non-dimensional parameter is equivalent to $F_2 = F \times \Sigma$. In the simple linearly varying density case, where $S(z) = 1$ for all z, $\Sigma = 1$. For more complex profiles, Σ is a measure of the scaled mean thickness between density levels. For example, a near surface intensified vertical stratification will increase Σ, which will decrease the oscillatory timescale.

4.5 Conclusions

This chapter extended the reduced order model from Maddison et al. (2023). In short, an oscillatory wind stress forcing was applied to this dynamical system and analysed. Solutions were found in the frequency domain, allowing for this system to be fully characterised. Two methods were used to solve this oscillatory system–linearisation of the dynamical system and a multistep numerical method. Both methods reassuringly result in the same conclusions. In the dynamical system, transport and integrated eddy energy cyclically evolve due to the growth and decay of baroclinicity. Baroclinically stable flow leads to transport growth. Excess growth results in baroclinic instability and eddy energy growth. This leads to a reduction in transport, which in turn leads to a reduction in instability. Eddy energy decays with increased baroclinic stability, and the cycle repeats.

Most notably, the solution in the frequency domain peaked in magnitude at $\omega_{1D} = \frac{1}{9.7}$ years^{-1} and underwent prominent phase shifts. This resonant frequency was also recovered in the system when forced with a steady wind, thus indicating the existence of an oscillatory timescale associated with GEOMETRIC, at least in reduced order systems. For the sake of discussion, frequencies higher than ω_{1D} are high and frequencies lower are low. At high frequencies, eddy energy is π out of phase with forcing and transport lags by $\pi/2$. There is a shift at ω_{1D}, at which eddy energy is in phase and transport leads by $\pi/2$ for low frequencies. It is also evident that this qualitative behaviour is not a consequence of the initial density profile. It is possible to change the oscillatory timescale, but this would simply shift any behaviour in the frequency domain.

These results from a dynamical system lead to some obvious questions. Primarily, it is unclear if this timescale of oscillation will persist in higher dimensional models. In order to determine this, the same set of experiments will be completed for a two-dimensional configuration in the next chapter. Additionally, it is undetermined whether or not this inherent oscillatory response is a consequence of using GEOMETRIC, or whether this is also present in higher dimensional and higher resolution models. This is explored in Chapter 6. It is unlikely for a dynamical system to perfectly capture the dynamics of the ACC. However, this model is certainly a start in understanding the response to time-dependent and oscillatory forcing.

5 | Two-dimensional model and the response of oscillatory forcing

This chapter focuses on a two-dimensional model of transient and equilibrated eddy saturation. This framework is based on Mak et al. (2017), which shows emergent eddy saturation on equilibrated timescales when GEOMETRIC is used. This model is extended by the inclusion of a time-dependent wind profile and analysis in the frequency domain. This model was built from scratch in Python 3.6 by the Author as part of this thesis.

In two-dimensions, a zonally averaged channel model is used. This allows for variability with depth and across latitude, in both the initial density profile and any results computed over time. In Chapter 4, the oscillatory frequency was analytically computed for an initial density profile which was a general function of z. This result suggests that surface intensified stratification profiles, which are often used to better replicate the real world–also lead to resonance, albeit with an altered timescale. However, this result assumes that density is linear in y. In two-dimensions, density (as well as the flow and energetics) can be general functions of both y and z. This chapter will determine how this affects the resonance and adjustment in this system.

This chapter contains the following: (1) the dynamical framework of the zonally averaged model, (2) replication of pre-existing steady state results, and (3) oscillatory wind stress experiments and results.

5.1 Dynamical framework

In two-dimensions, we restrict our attention to the Boussinesq case, focusing specifically on the mean density equation and eddy energy budget. The density equation is given by

$$\frac{\partial \rho}{\partial t} + \frac{\partial}{\partial y}\Big((v_{mean} + v_{eddy})\rho\Big) + \frac{\partial}{\partial z}\Big((w_{mean} + w_{eddy})\rho\Big) = 0, \tag{5.1}$$

where total velocity (mean plus eddy, $\mathbf{v}_{tot}$) satisfies incompressibility, $\nabla \cdot \mathbf{v}_{tot} = 0$. The eddy velocities are defined as

$$v_{eddy} = \frac{\partial \psi^*}{\partial z}, \tag{5.2}$$

$$w_{eddy} = -\frac{\partial \psi^*}{\partial y}, \tag{5.3}$$

where ψ^* is the eddy streamfunction,

$$\psi^* = \kappa \left[\frac{\partial \rho}{\partial y}\right]\left[\frac{\partial \rho}{\partial z}\right]^{-1}, \tag{5.4}$$

and κ is the eddy transfer coefficient. This is the channel model version of the Gent-McWilliams parameterisation scheme (Gent and McWilliams, 1990; Gent et al., 1995). The mean velocities satisfy the f-plane steady state equations,

$$-f v_{mean} = \frac{1}{\rho_0}\frac{\partial}{\partial z}(\tau_s - \tau_b), \tag{5.5}$$

and

$$\frac{\partial v_{mean}}{\partial y} + \frac{\partial w_{mean}}{\partial z} = 0. \tag{5.6}$$

In Mak et al. (2017), the surface wind stress is defined

$$\tau_s(y, z = 0) = \frac{\tau_0}{2}\left(1 - \cos\left(\frac{2\pi y}{L_y}\right)\right), \tag{5.7}$$

where τ_0 is peak wind stress magnitude. Bottom form stress is represented by τ_b. This is applied across the bottom cells, and is meant to model topographic form stress. This is chosen to exactly balance out the surface stress. To vary wind stress over time, this spatially sinusoidal wind jet evolves sinusoidally over time. This is implemented by first defining

$$A(t) = \epsilon\tau_0 \sin(2\pi t/P), \tag{5.8}$$

where ϵ is the amplitude change in wind stress magnitude and P is the forcing period. $A(t)$ is the magnitude change added to the steady wind stress. That is, in order to vary the wind profile over time, Eq.(5.7) is replaced with

$$\tau_s(t, y, z = 0) = \frac{\tau_0 + A(t)}{2}\left[1 - \cos\left(\frac{2\pi y}{L_y}\right)\right]. \tag{5.9}$$

This stress linearly decreases to 0 across the upper 146 m of the domain. As the bottom stress is chosen to exactly cancel out the surface wind stress, it is also applied to the bottom 146 m in order to represent bottom form stress from topographic barriers. This is equivalent to the top and bottom five cells of the domain for this configuration. Further, $\frac{\partial \tau_s}{\partial z}$ is constant over the forcing layer.

The eddy energy budget is given by

$$\frac{d}{dt}\int_{-H}^{0}\int_{0}^{L_y} E \,\mathrm{d}y\,\mathrm{d}z = \int_{-H}^{0}\int_{0}^{L_y} \kappa\frac{M^4}{N^2}\,\mathrm{d}y\,\mathrm{d}z - \lambda\int_{-H}^{0}\int_{0}^{L_y} E\,\mathrm{d}y\,\mathrm{d}z, \tag{5.10}$$

where M and N are the horizontal and vertical buoyancy frequencies respectively given by

$$M^2 = \frac{g}{\rho_0}\left|\frac{\partial \rho}{\partial y}\right|, \tag{5.11}$$

and

$$N^2 = -\frac{g}{\rho_0}\frac{\partial \rho}{\partial z}. \tag{5.12}$$

In the eddy energy budget, the first term on the right hand side is the source term and the second term is the dissipation of energy from topographic form stress. The source term is a weighted integral of the eddy transfer coefficient as defined by the GM scheme (Gent and McWilliams, 1990; Gent et al., 1995). This is a conversion of parameterised eddy energy to mean energy. Conveniently, κ can be defined via GEOMETRIC or other parameterisations. Eddy energy sources originate from instabilities in the ocean. Here, baroclinic instability is assumed to be the primary source of eddy energy (Eady, 1949; Straub, 1993). GM represents baroclinic instability through an eddy streamfunction that acts to flatten density surfaces, leading to a loss of mean potential energy. In GEOMETRIC, the eddy transfer coefficient depends linearly on the eddy energy.

Eddy energy dissipation is modelled with relative simplicity. In Eq.(5.10), eddy energy dissipation is represented by the linear damping rate, λ. In reality, dissipation is complicated and is the amalgamation of different processes such as bottom drag, lee wave radiation, and western boundary processes. Instead of modelling the many processes, λ parameterises all the physics involved in dissipation (Mak et al., 2018). The energy budget comes from the zonally averaged hydrostatic Boussinesq equations (Mak et al., 2017). Manipulating these equations leads to a budget for the eddy energy density, $\rho_0 E$. Since ρ_0 is a non-zero constant, this can be factored out of the budget as given in Eq.(5.10). However, it is noted that the literature often refers to eddy energy density when referencing eddy energy. Unless otherwise stated, this chapter is concerned with specific eddy energy, rather than the eddy energy density ($\rho_0 E$). When depth integrated eddy energy is computed, this is the depth integrated specific eddy energy. For ease, this is referred to as "depth integrated eddy energy".

These equations are first spatially discretised using finite difference methods and then numerically stepped forward in time with a linear multistep method with a time step of $\Delta t = 3$ hours. This time step is generously small enough to ensure numerical stability while avoiding the need to use a variable time step method. Equations are stepped forward in time using the third-order Adams-Bashforth method after discretising on a uniform Arakawa C-grid. This time stepping method was also used with the dynamical system and is summarised by Eq.(4.36). Density is defined on the cell centres and fluxes are defined on the cell interfaces. Before any wind perturbations are applied, the model is integrated in time until it reaches steady state. Due to the lack of surface buoyancy forcing, at steady state, there is zero mean residual overturning. The initial density profile is given by

$$\rho(y, z, t = 0) = \rho_0 - b e^{z/c}, \tag{5.13}$$

where $\rho_0 = 1028\ \mathrm{kg/m^3}$, $b = 0.6\ \mathrm{kg/m^3}$, and $c = 750\ \mathrm{m}$. To prevent blow-up the following bounds are imposed:

$$\kappa_{\max} = 10000 \ \mathrm{m}^2/s, \tag{5.14}$$

$$\kappa_{\min} = 50 \ \mathrm{m}^2/s, \tag{5.15}$$

$$\left|\left[\frac{\partial\rho}{\partial z}\right]\right|_{\min} = 1 \times 10^{-5} \ \mathrm{kg/m}^4, \tag{5.16}$$

$$-\left[\frac{\partial\rho}{\partial y}\right]\left[\frac{\partial\rho}{\partial z}\right]^{-1}_{\max} = 5 \times 10^{-2}. \tag{5.17}$$

Additionally, N^2 is restricted to positive values only. Relevant parameters are listed in Table 5.1.

Parameter	Value	Description
L_y	2000 km	meridional length
H	3500 m	depth
(dy, dz)	$(25$ km, 25 m$)$	grid spacing
τ_0	$0.2 \ \mathrm{N/m}^2$	surface wind stress magnitude
λ	$1 \times 10^{-7} \ s^{-1}$	eddy energy dissipation rate
f_0	-1.11×10^{-4}	Coriolis parameter
ρ_0	$1028 \ \mathrm{kg/m}^3$	reference density
b	$0.6 \ \mathrm{kg/m}^3$	decay factor of initial density profile
c	750 m	e-folding depth for initial density profile
α	0.1	eddy efficiency parameter

Table 5.1: Parameter values used in the numerical model. Values are typical for ACC-like configurations in two-dimensions.

5.2 Model verification

Before varying wind over time, the steady state results from Mak et al. (2017) are replicated in order to verify the model. To do this, a 100 year spin up with steady wind stress ($\tau_0 = 0.2 \ \mathrm{N/m}^2$) is first computed. This short spin up period is sufficient as this model quickly equilibrates across all diagnostics. Fig. 5.1 shows the initial and final density profiles for spin up. The isopycnals tilt towards the surface, outcropping towards the south, and the deep ocean is relatively unstratified. This behaviour is typical for zonally averaged circumpolar channel models with ACC-like parameters. The tilting of density surfaces is crucial for fuelling the mesoscale eddy field. Baroclinic instability counteracts the steepening of density surfaces via mesoscale eddies. From the parameterised eddy energy conversion source, the eddy induced circulation extracts available potential energy from the mean state and opposes the Eulerian (wind induced) circulation.

Following spin up, the model is then impulsively perturbed with different wind stress values ranging from $\tau_0 = 0.01$ to 0.5 $\mathrm{N/m^2}$ for a further 50 years. That is,

$$\tau_0 = \begin{cases} 0.2 & t \leq 100 \text{ years}, \\ \tau_p & t > 100 \text{ years}, \end{cases} \tag{5.18}$$

where τ_p is one of the new perturbation wind stress values. In other words, the model is subjected to an instantaneous step-wise wind stress magnitude change.

This spin up and suite of perturbations is completed twice–once using GEOMETRIC, and again using GM. Defining the eddy transfer coefficient with different parameterisations leads to conflicting results. Standard GM is straightforward and simple to implement, as the transfer coefficient is set to a constant. $\kappa_{GM} \approx 2454.3$ m^2/s^2, which corresponds to the equilibrated κ_{GEOM} value, is chosen to keep the control diagnostic magnitudes as close as possible. Different κ_{GM} values would lead to different transport and eddy energy values, but the qualitative behaviour of the system remains the same (not shown). It is noted that κ_{GM} is larger than usual for zonally averaged ACC-like models. It is possible to tune the eddy transfer coefficient, but this would not affect the physics of the perturbations. For example, doubling λ leads to smaller eddy transfer coefficient values (1095 m^2/s^2) and greater transport (190 Sv) values.

When using GEOMETRIC, the eddy transfer coefficient is defined

$$\kappa_{\text{GEOM}} = \alpha E \frac{N}{M^2}, \tag{5.19}$$

where the eddy energy budget is used in order to define the eddy transfer coefficient at each time step.

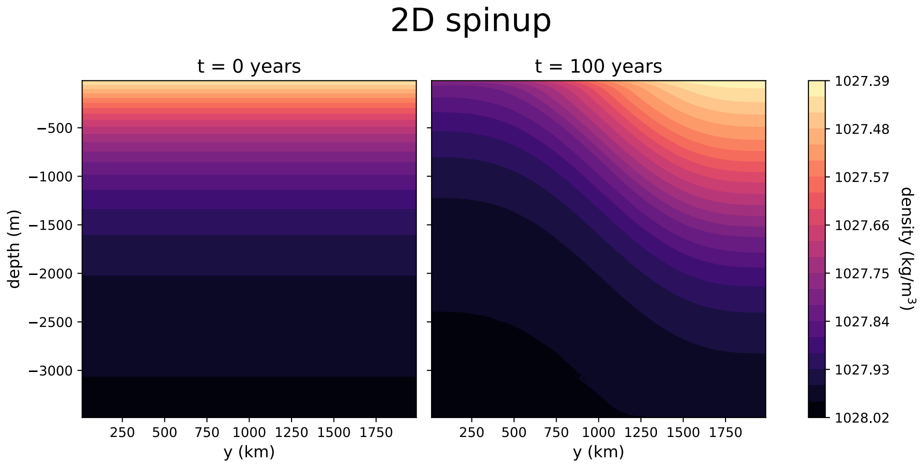

Figure 5.1: The density structure at the first and final steps of the two-dimensional spin up. There is change in both y and z. Isopycnals outcrop towards the south at equilibration and the deep ocean remains relatively dense.

Calculations computed with GEOMETRIC are discussed first. Immediately after perturbation there is an adjustment period for both transport and eddy energy. However, this is short lived, and transport shifts towards an emergent eddy saturated regime. Energy, on the other hand, scales with the magnitude of wind stress perturbation after the adjustment period. Both of these diagnostics are shown in Fig. 5.2. Within the first 40 years of perturbation, the low wind limit case ($\tau_0 = 0.01 \text{ N/m}^2$) does not approach eddy saturation. This is a constraint on κ_{GEOM}, which needs more time to counteract the dramatic wind stress change. For reference, after 100 years of perturbation (not shown) where $\tau_0 = 0.01 \text{ N/m}^2$, transport is approximately 102 Sv, $\kappa_{GEOM} = 117 \mathrm{~m}^2/s^2$, and depth integrated eddy energy is about $2 \mathrm{~m}^3/s^2$. Here, eddy energy includes both eddy kinetic energy and eddy potential energy. Eddy energy is additionally depth-integrated and averaged across the channel. That is, the low wind limit does eventually lead to eddy saturation, albeit with a severely reduced eddy transfer coefficient and low energetics. This, however, is expected from theory, as eddy energy scales with surface wind stress (Marshall et al., 2017). It is interesting to see how the transport and energy adjust over time, as the literature usually only presents long term averaged results.

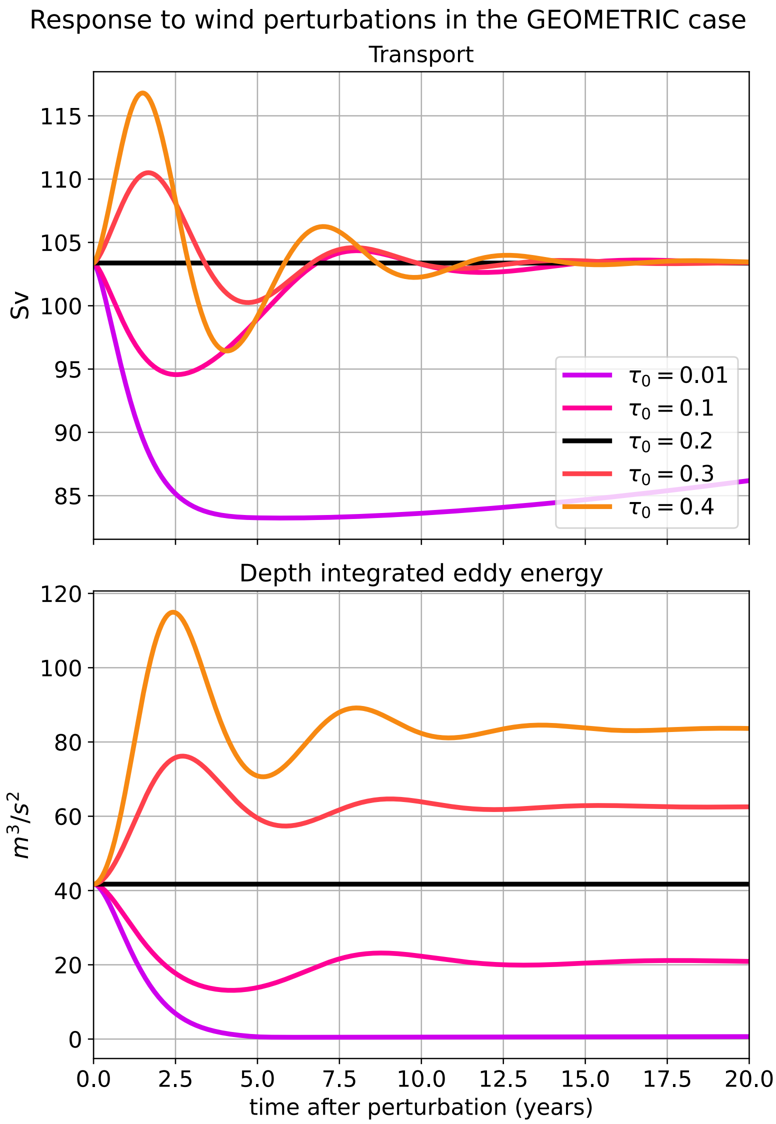

Figure 5.2: Time series of transport and eddy energy when parameterised with GEOMETRIC. This time series has been truncated to the first 20 years after perturbation to better show the adjustment and emergent eddy saturation.

Following the same procedure, the perturbations are computed with standard GM. As expected from theory and in agreement with the results in Mak et al. (2017), both transport and eddy energy scale directly with wind stress magnitude. The adjustment takes place over the first 10 to 15 years after perturbation before reaching a new steady state. Within this time frame, transport and depth integrated eddy energy either increase or decrease, depending upon the choice of τ_0. The exponential decay to equilibrium also takes place in Allison et al. (2011). In this work, the timescale of adjustment in much shorter (years to decade, rather than centuries) due to the lack of a northern basin. Shorter adjustment is to be expected in channel-only models. Time series of the diagnostics are shown in Fig. 5.3.

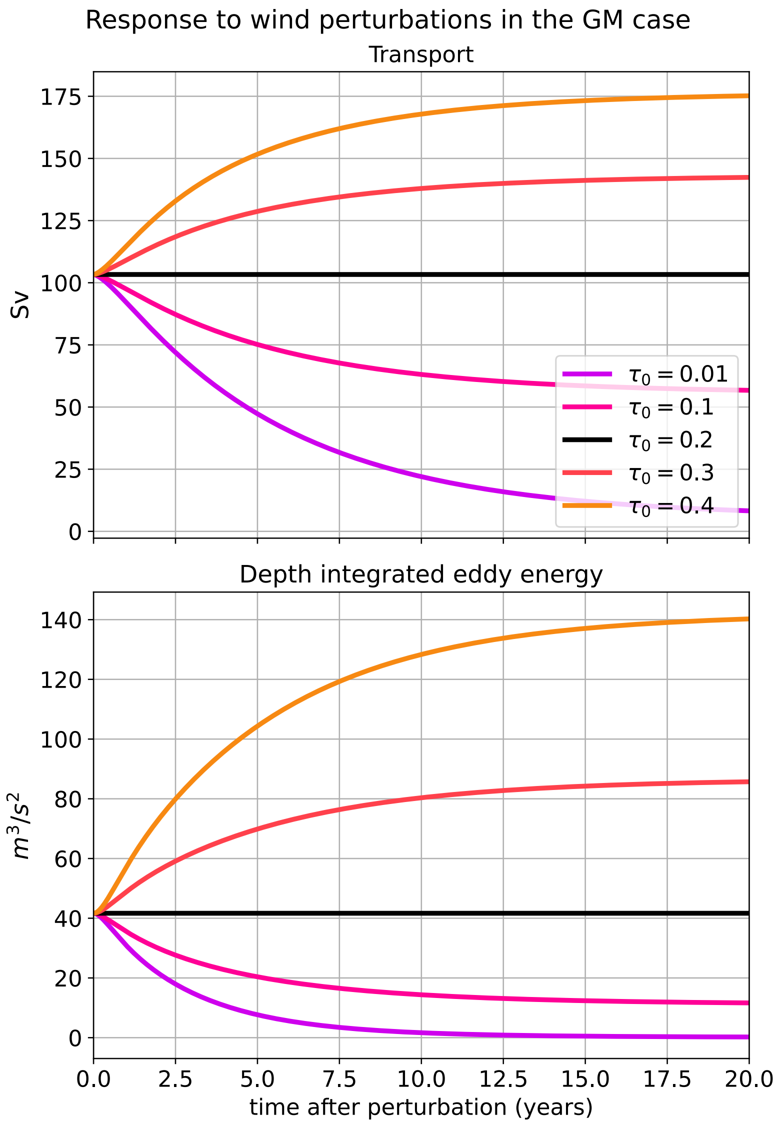

Figure 5.3: Time series of transport and parameterised eddy energy computed with standard GM. This time series has been truncated to the first 20 years after perturbation, showing adjustment to a new equilibrium that scales with wind stress magnitude.

After just 50 years of perturbation, it is very clear that GEOMETRIC leads to eddy saturation and standard GM does not. In both parameterisations, however, the total eddy energy scales with wind stress magnitude. This is clearly depicted in Fig. 5.4. These results replicate the findings in Mak et al. (2017), thus verifying this two-dimensional numerical model.

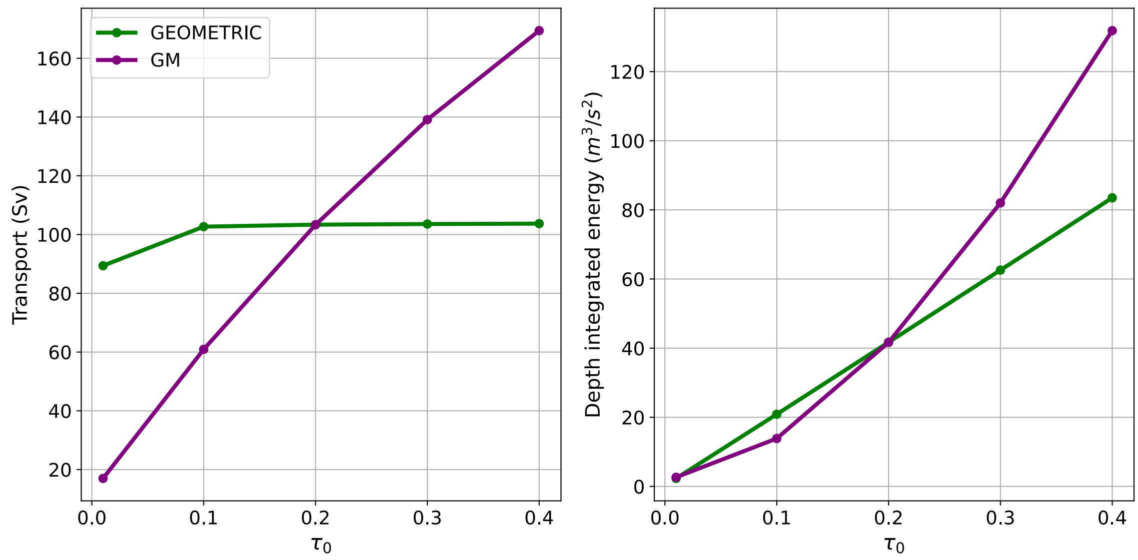

Figure 5.4: A comparison of the results computed with GEOMETRIC and GM. Following wind stress kicks, transport and depth integrated eddy energy are averaged over time. Each average is shown against the kick magnitude. The eddy energy equation is solved for both GEOMETRIC and GM to compute integrated eddy energy.

The steady state results shown in Fig. 5.4 are comparable with the fixed-point solutions from the dynamical system when GEOMETRIC is employed (see Chapter 4 equations (4.28) and (4.27)). The fixed point of integrated eddy energy depends on τ_0, so that $\mathcal{E}^*$ increases with wind stress magnitude. On the other hand, the fixed point for thermal wind transport is insensitive to changes in wind stress, as T^* does not depend on wind stress magnitude. This is depicted in Fig. 5.5.

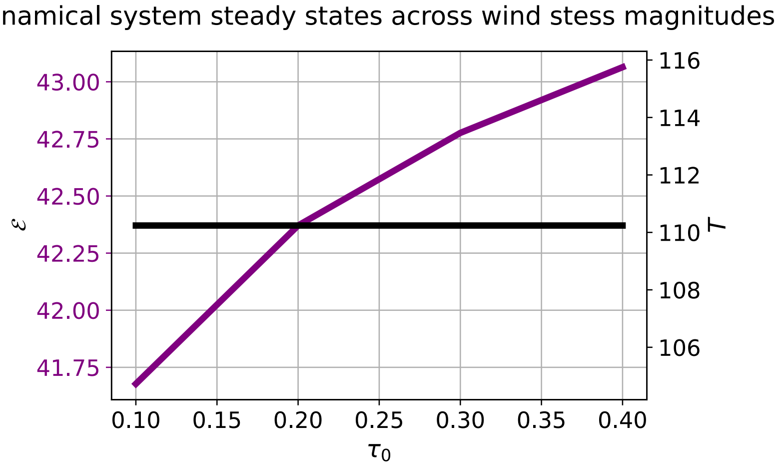

Figure 5.5: This shows how the fixed points for thermal wind transport and parameterised eddy energy from Chapter 4 evolve with wind stress magnitudes. GEOMETRIC is used to compute these values, and this should be compared with Fig. 5.4.

5.3 Oscillatory wind stress forcing

The following presents the results of the wind stress forcing experiments in the two-dimensional configuration. The two-dimensional system is forced with wind stress oscillations with periods ranging from 1 day to 90 years. It is noted that extremely high frequencies, such as $1\ \mathrm{days}^{-1}$ are not physical for the ACC. These frequencies are included for completeness in the response function calculations. Each experiment is run for either 40 years or 40 oscillations, whichever is longest. Frequency analysis is completed on the latter half of each experiment (i.e., for either 20 years or 20 oscillations, whichever is longest). As in the previous chapter, transport and the integrated eddy energy responses are determined. An additional diagnostic, depth integrated kinetic energy, is included for this configuration when GEOMETRIC is used. Depth integrated kinetic energy will be compared to results from later chapters. Specifically, Chapter 6 focuses on an eddy resolving model that cannot compute parameterised eddy energy, but can diagnose total kinetic energy. Total kinetic energy does not exclude the mean component. This diagnostic is defined by

$$K(t) = \frac{1}{2L_y} \iint \mathbf{u} \cdot \mathbf{u} \, \mathrm{d}y \mathrm{d}z, \tag{5.20}$$

where zonal velocity is found from the shear. This is depth integrated, meridionally averaged kinetic energy.

5.3.1 Results

Following spin up, wind perturbations of different periods are applied to the two-dimensional system. The time series of the responses are shown in Fig. 5.6 for the first 40 years following spin up. The time series for transport suggests that forcing oscillations longer than about 8 years show smaller amplitude variability, which foreshadows the solution in the frequency domain. Short forcing oscillations of periods less than a year appear relatively steady. Likewise, eddy energy follows these qualitative trends in the time domain.

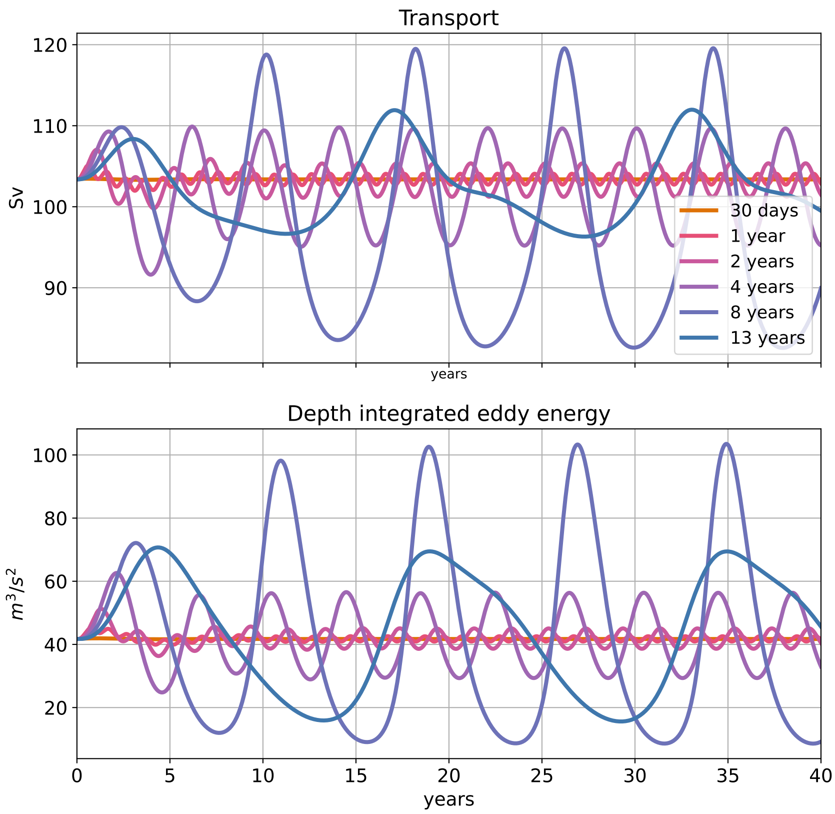

Figure 5.6: The time evolution of transport and eddy energy when computed using GEOMETRIC for a variety of wind forcing periods. A selection of periods are plotted for the first 40 years following spin up.

Fig. 5.7 isolates the final 20 cycles of the 90 day forcing experiment. For both the transport and integrated eddy energy diagnostics, there is a significant peak at the frequency associated with the forcing frequency. This is expected and persists across all experimental frequencies. Additionally, this peak is stable and does not decay over the integration.

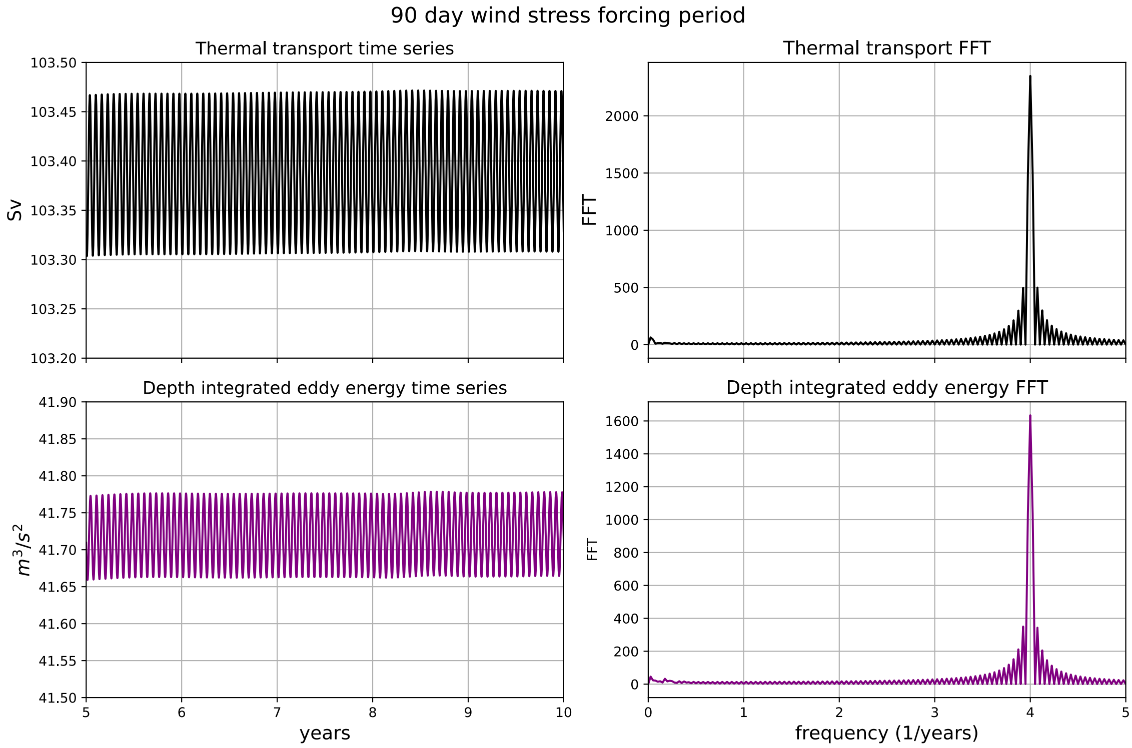

Figure 5.7: The time series (left) and Fourier transforms (right) for the 90 day perturbation experiment for the final 20 cycles of oscillatory perturbation. Diagnostics are de-trended before the Fourier transform is computed.

Fig. 5.8 shows the relationship between the oscillatory wind stress forcing and the computed diagnostics. The chosen forcing periods (90 days, 8 years, and 40 years) represent a range of forcing frequencies including high, resonant, and low frequency. All phase portraits show the final 20 cycles, in line with the frequency analysis methodology. At the highest shown frequency (90 day cycles), wind stress magnitude seemingly has no significant effect on transport nor eddy energetic variability when compared to the other wind oscillations. For such high frequencies, there is essentially not enough time for the density field to react with sufficient change for either transport or eddy energy to change. It is noted that both the traces of transport and eddy energy against wind stress are anticlockwise (not indicated). At the resonant frequency (at the 8 year forcing period), variability is at its greatest for both diagnostics. This frequency was determined empirically by simulations. Maximal wind stress magnitude is roughly correlated with maximal transport values. Likewise, minimum wind stress magnitude roughly coincides with minimum transport values. Depth integrated eddy energy is out of phase with the oscillatory wind stress magnitudes. For both diagnostics, decreasing magnitude is approximately linear with wind stress magnitude. The system exhibits a sawtooth oscillation with a faster decay phase. This was evident in the time series in Fig. 5.6. Diagnostic variability falls for lower frequencies, such as in the case of the 40 year forcing period. For this low frequency forcing, transport and wind stress magnitude are clearly out of phase. Transport approaches a maximal value when $\tau_0 < 0.2$ $\mathrm{N/m^2}$. Depth integrated eddy energy is in phase with the forcing. Increases and decreases in depth integrated eddy energy are linear with wind stress magnitude.

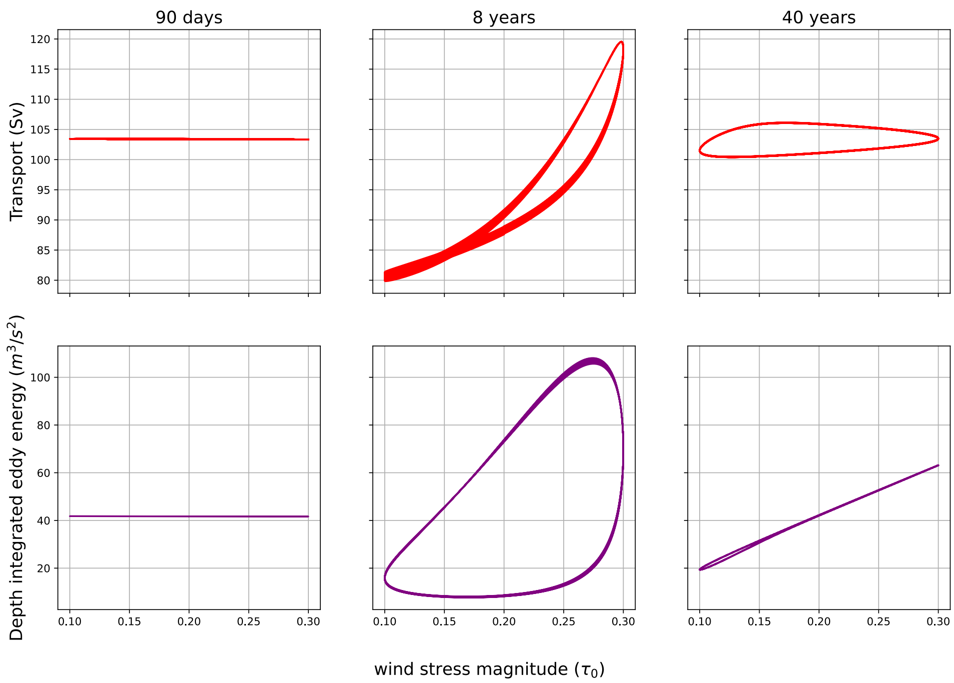

Figure 5.8: Phase portraits for the 90 day, 8 year, and 40 year perturbations (left to right). This shows transport against wind stress magnitude (top) and depth integrated eddy energy against wind stress magnitude (bottom). The forcing frequencies dominate the signals across diagnostics and forcing period.

Fig. 5.9 shows the same frequency subset, but for transport against eddy energy. The 90 day forcing experiment is in line with what has been previously discussed. On the shared axes at this frequency there is virtually no change over time, hence the "point" plot. The 8 year forcing period shows the greatest variability amongst the sub-selection of frequencies. Both of the longer forcing periods also show that the diagnostics are not in phase with each other. However, this is more pronounced in the 40 year forcing period. For a complete look at the relationship between transport and eddy energy, Fig. 5.10 shows each phase portrait for all forcing frequencies. It is clear that the resonant frequency results in the greatest variability.

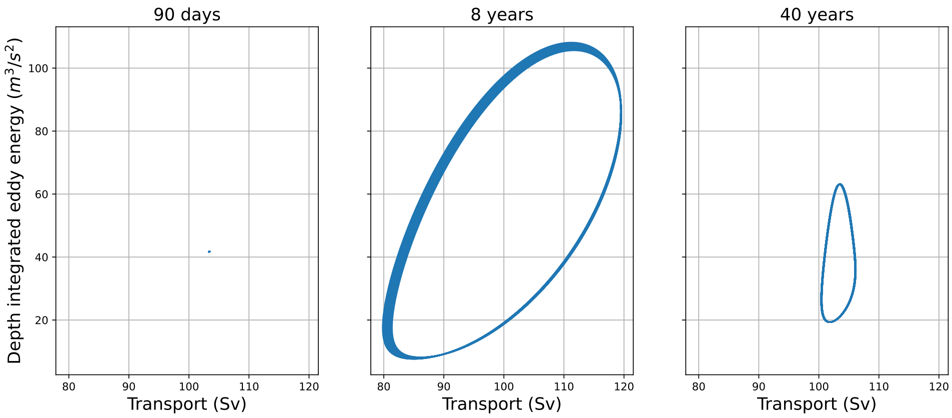

Figure 5.9: Transport against eddy energy for the 90 day, 8 year, and 40 year wind forcing perturbations. This complements Fig. 5.8. The axes are shared across this figure.

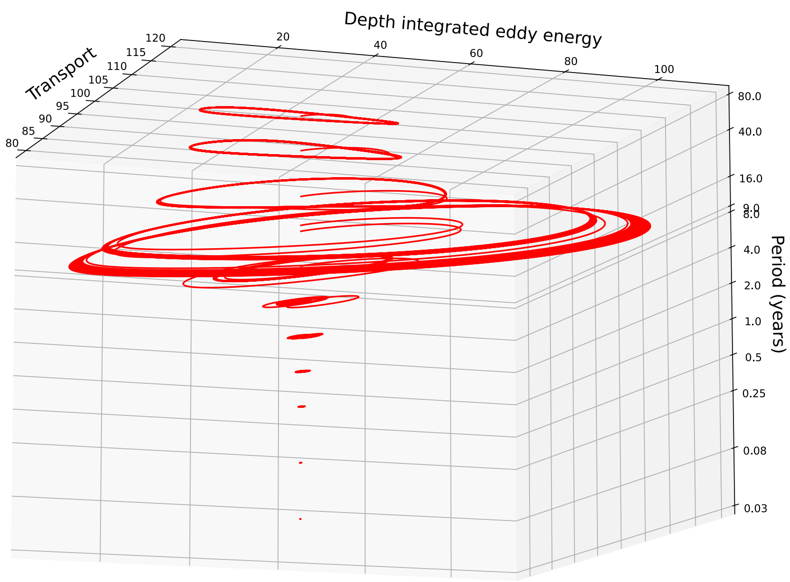

Figure 5.10: A three-dimensional interpretation of transport against eddy energy. The length of forcing period (in years) forms the third dimension of this figure (longer periods are upwards).

Time series and phase portraits will only suggest qualitative trends associated with different forcing periods. To best characterise the system, the frequency domain is more useful. The response function across all experimental frequencies is computed and shown in Fig. 5.11. The response magnitude peaks at $\frac{1}{8}$ years^{-1}

in transport, depth integrated eddy energy, and depth integrated total kinetic energy. This indicates that the system behaves as a driven harmonic oscillator with a driving frequency of approximately $\frac{1}{8}$ years^{-1}. The depth integrated eddy energy response plays a much larger role in this system than kinetic energy. Since this is a parameterised configuration, the energy is mainly put towards feeding the parameterised eddy field rather than the total kinetic energy.

Phase shifts are linked to the peak oscillatory timescale. Transport lags the wind forcing for frequencies greater than the resonant frequency. This change in phase relationship does not exactly fall at a single frequency as it does in the dynamical system. This deviation may be due to the long forcing periods, which have not yet completed adjustment. For transport, this change is sufficiently near $\pi/2$ for the dynamical system and the two-dimensional model to be comparable with each other. Depth integrated kinetic energy also lags by approximately $\pi/2$ for frequencies greater than the resonant frequency. Depth integrated eddy energy on the other hand, lags/leads by π for high frequencies. (Note, that a lag and lead by π are equivalent). For frequencies lower than the resonant frequency, transport and kinetic energy lead by approximately $\pi/2$ while eddy energy is in phase with the forcing. Therefore, both the transport and eddy energy responses behave in line with the reduced order dynamical system.

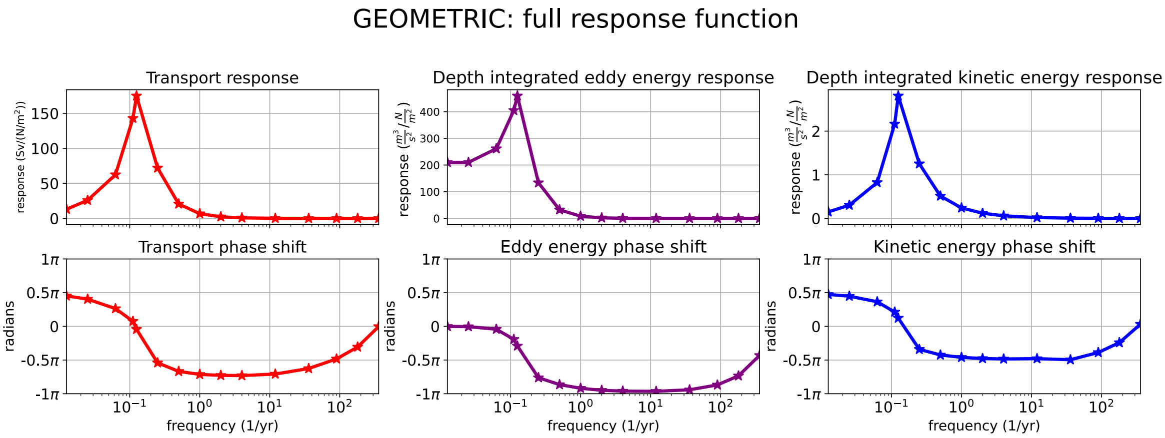

Figure 5.11: The response functions (magnitude and phase) of transport, depth integrated eddy energy, and depth integrated kinetic energy (left to right). The transport and kinetic energy responses lag the wind forcing by approximately $\pi/2$ and the integrated eddy energy is approximately out of phase with the wind forcing for $\omega > \frac{1}{8}$ years^{-1}. For $\omega > \frac{1}{8}$ years^{-1} the transport and kinetic energy response leads the wind forcing by $\pi/2$ and the integrated eddy energy is in phase with the wind forcing. These responses are computed with GEOMETRIC. All diagnostics share a common peak frequency, which also coincides with a change in the phase relationship.

The response function for GM completely differs from GEOMETRIC's response. There is no response peak associated with any frequency (see Fig. 5.12). As the forcing frequency decreases, the response magnitude grows exponentially with the $\log$ of frequency for both diagnostics (kinetic energy is not shown but also follows this trend). This response complements the time series associated with GM, which shows diagnostic magnitude increasing with forcing period length. Unlike GEOMETRIC, there is no peak frequency at which diagnostics reach peak variability. This means that there is no evidence for resonance in GM.

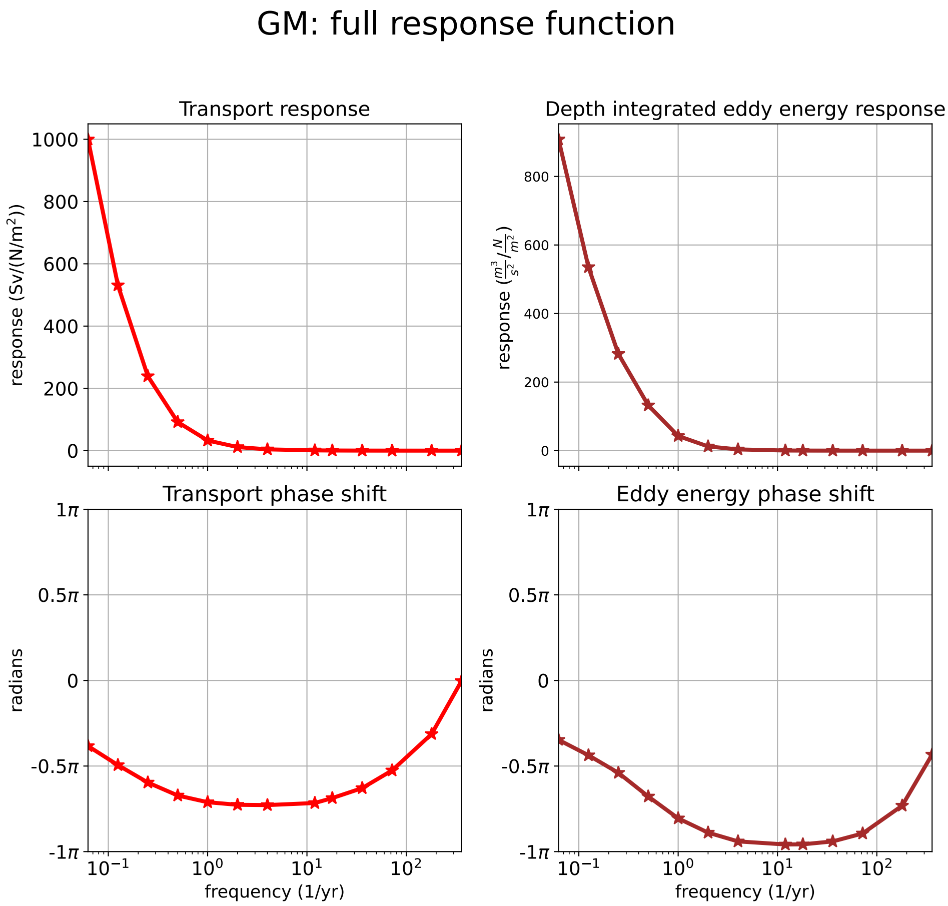

Figure 5.12: The response functions for transport and eddy energy when computed with standard GM. There is no peak frequency within the tested range. Transport and eddy energy both lag the wind forcing for the test frequencies.

5.3.2 Relationship to the dynamical system

Fig. 5.13 shows the linearised dynamical system and two-dimensional response function magnitudes and phase shifts on shared axes. Qualitatively, the response functions show similar behaviour. However, in both diagnostics, the two-dimensional peaks are wider than the dynamical system with a linear profile's response peaks. The phase of both diagnostics are also similar between models. In the dynamical system, the phase sharply shifts at the resonant frequency, whereas in the two-dimensional model, this change is less abrupt. However, broadly speaking, transport shifts from lagging by approximately $\pi/2$ to leading by $\pi/2$ before and after the resonant frequency. Eddy energy on the other hands, goes from leading/lagging by π to being in phase with the forcing. This slow change in phase may be due to computational constraints. Running longer period forcings for longer would possibly alleviate the phase adjustment. However, running experiments for more cycles–especially at lower frequencies–is computationally expensive. For the sake of this experiment, it was not necessary, as the given forcings show the system's behaviour regardless. In both models, it is clear that there is a resonant frequency inherent to the system which delineates behavioural differences. The two-dimensional response function also takes the form of the standard linear oscillator. This is discussed in Chapter 4.

There are some clear differences between the response functions of the dynamical system and the two-dimensional model. Primarily, the oscillatory timescales differ–although this could be forced equal through model tuning. This is not very important, as there are already inherent differences between the two systems, as changing from a strictly time-dependent system to a space-and-time dependent system naturally leads to differences. For instance, the two-dimensional model imposes a bottom form stress that varies in y and is applied over the bottom five depth cells. In the dynamical system, there is only an eddy energy dissipation constant (λ) which acts to dissipate energy. This is present in higher dimensional configurations, but is not the sole dissipater of eddy energy. Additionally, the two-dimensional model imposes an exponential density profile in both y and z, whereas the dynamical system has only been verified to include depth varying only density profiles (see Section 4.4.1).

The two-dimensional system has a wider response curve peak. It is possible to diagnose an effective damping timescale from this width. This damping timescale is an inherent break in Hamiltonian structure due only to the spatial variation in density. This is a qualitative difference between the dynamical system and the two-dimensional model.

In both the dynamical system and two-dimensional model, the results at low frequency relate to what is known about eddy saturation at equilibrium. As the forcing frequency tends toward zero (the forcing oscillations are longer), the response functions converge to an equilibrated eddy saturated state. For thermal wind transport, the response converges to zero response while the response of depth integrated eddy energy rapidly converges towards a non-zero constant. This is consistent with eddy saturation in equilibrium. For sufficiently long timescales, the mesoscale eddy field opposes the growth of transport by the input of energy from excess wind stress. This is reflected in the response functions, where the integrated eddy energy approaches a constant (essentially fuelled by the external input of energy). This can be tied back to Eqs.(2.9) and (2.13), which state the eddy energy is set by surface wind stress and thermal wind transport scales with eddy energy dissipation.

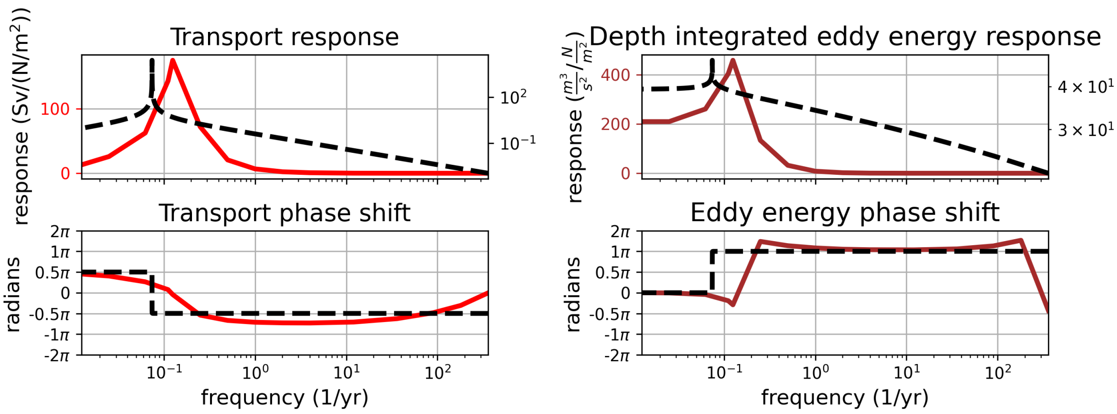

Figure 5.13: A comparison between the dynamical system and the two-dimensional model. The dashed lines show the magnitude and phase of the dynamical system, whereas the solid red and brown lines show the two-dimensional results. Only the linear response of the dynamical system is shown, as it agrees with the numerical solution.

5.4 Conclusions

This is a two-dimensional model of transient and equilibrated eddy saturation. This model allows for temporal and spatial variation in wind stress profile and a non-linear initial density profile. A notable weakness of this model is tied to its simplicity. For example, in more complex models, a surface restoring temperature condition can be applied to the ocean surface. With more work, this could be implemented in future iterations.

In Mak et al. (2017), other eddy parameterisation methods are analysed. These schemes use alternative eddy transfer coefficients from pre-existing schemes. It would be straightforward to apply other eddy parameterisations and subsequently determine the response functions. However, as GEOMETRIC produced the best emergent eddy saturation in the non-oscillatory experimental setup, it was not deemed necessary for the investigation of the transient response to oscillatory wind stress.

The next logical step in the hierarchy is to model three-dimensional spatial flow in an ACC-like configuration. This will help determine whether or not the inherent oscillatory signal is a signature of GEOMETRIC, or a signature of a "real" physical phenomena. The remaining two pieces of the hierarchy are eddy parameterising and eddy resolving three-dimensional circumpolar channel models. Comparing these against each other, and with the discussed dynamical system and two-dimensional model, will further explain circumpolar adjustment across frequencies.

6 | Oscillatory forcing in three-dimensional models

The previously discussed models are highly idealised. In Chapter 4, solving a set of coupled ordinary differential equations gives transport and integrated eddy energy. This model only varies in time rather than space, thus neglecting any spatial variation that may have an effect on the timescales of eddy saturation adjustment. While greatly simplified, this model is useful in the initial understanding of the response to oscillatory wind forcing, as an explicit solution can be determined through linearisation. Of course, the existence of an explicit solution for such a reduced model is by design. Due to the simplicity of the model a solution can be found; a solution can be determined for simple models of this order. Upon analysis, it was not obvious if the resonance from this highly simplified model would persist in models with increased dimensions.

The next logical step in a hierarchy of models is put forth in Chapter 5. This chapter presents a zonally averaged model, allowing for spatial variation in the yz plane. This model, while not solved explicitly, is still computationally inexpensive to solve using time-stepping methods. The results from this model nearly match the results from the reduced order dynamical system. Together, these results suggest an inherent oscillatory timescale that is at least associated with GEOMETRIC in lower dimensional models. This however leads to some obvious questions. Mainly, how will resonance apply to more detailed and higher dimensional circumpolar channel models? Will the consistency between models hold in three-dimensions? Is this timescale only associated with GEOMETRIC or is there evidence for its existence in eddying models (and furthermore, the real world)? How will topography affect the physics of eddy saturation across timescales? What physical mechanisms are controlling the system at low and high frequencies?

In an attempt to begin answering these questions, this chapter presents an eddy parameterised model and eddy resolving model, both with a submerged ridge, forced with oscillatory winds following a sufficiently long spin up. These models are built using MITgcm and simulate an ACC-like channel. The familiar experimental procedure from earlier chapters is applied to the three-dimensional channel models. In the context of pre-existing literature, these oscillatory wind stress experiments follow on from Sinha and Abernathey (2016) but with some notable developments. Primarily, this work looks at the frequency domain in greater detail by including more forcing frequencies. Wind stress periods are chosen to bridge gaps between the frequencies chosen in previous works. The methods of analysis also differ from Sinha and Abernathey (2016). These differences were described in Section 3.3.1.2. Furthermore, this work focuses on different diagnostics in order to understand the mechanisms behind transient eddy saturation and the response to oscillatory wind stress forcing. "The problem of a channel flow forced by oscillating winds [is] an ideal test case for mesoscale parameterisation" (Sinha and Abernathey, 2016). Mesoscale eddies play a role in the feedback mechanism of ACC transport through generation and dissipation of baroclinic instability. Whether or not a parameterisation has the ability to accomplish such conversion on transient timescales is therefore a test of the parameterisation's robustness. Comparing results between three-dimensional eddy parameterising, three-dimensional eddy resolving configurations, two-dimensional model, and dynamical system is a step in testing the parameterisation's robustness.

This chapter begins with a description of the parameterised configuration. This section states relevant parameters and describes the model. Results from the parameterised model are presented and discussed. A three-dimensional eddy resolving model is next presented. Finally, comparisons are made between all the models described within this thesis.

6.1 Eddy parameterised channel configuration

This configuration has similar bathymetry to widely studied ACC-like models (e.g., Munday et al. (2013), Sinha and Abernathey (2016), Mak et al. (2018), Youngs et al. (2019)). This model is the next logical step in the hierarchy of models.

The eddy parameterised configuration is a coarse resolution three-dimensional idealised ACC-like model on the β-plane implemented in MITgcm. The domain is 2000 km wide, 6000 km long, and 5000 m deep with a centred ridge with a maximal height of 1500 m. Grid resolution is 100 km $\times$ 100 km (about $1°$ resolution) which is not eddy resolving. The bathymetry is depicted in Fig. 6.1.

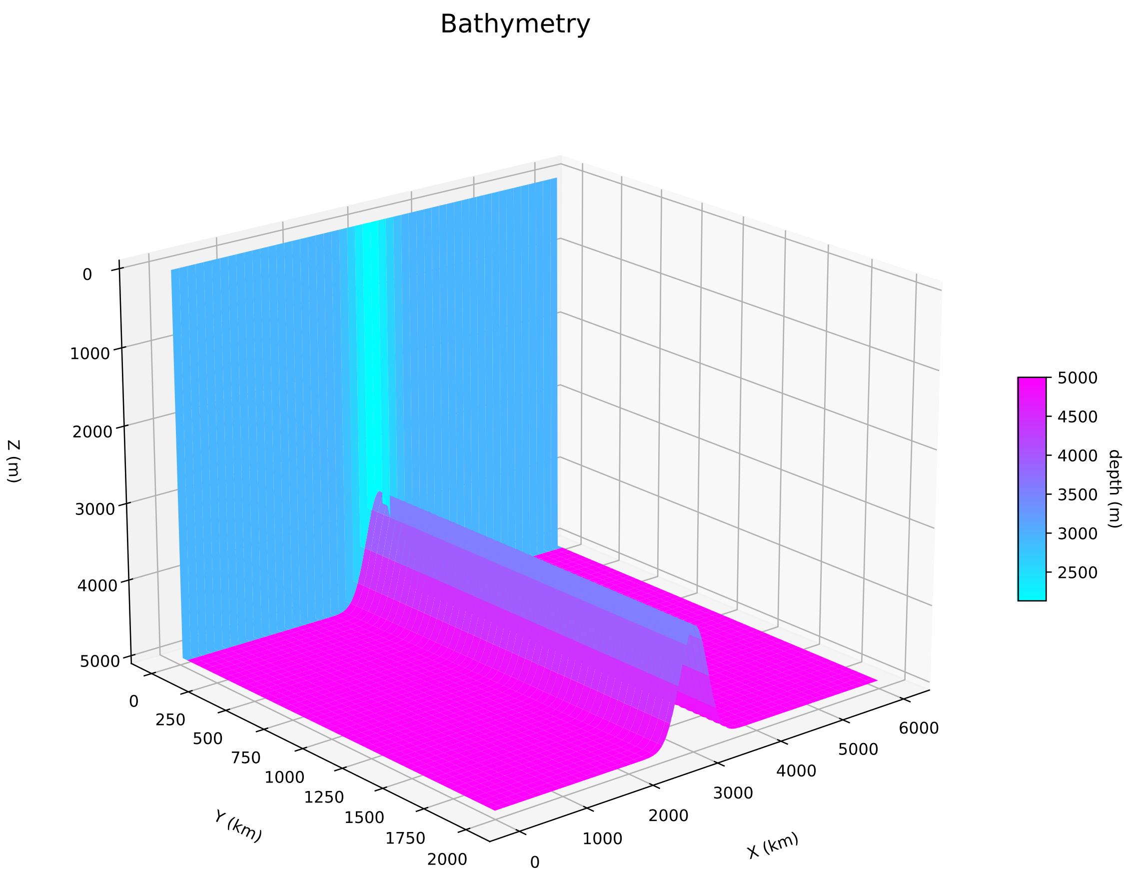

Figure 6.1: This shows the three-dimensional bathymetry in both the eddy parameterised and eddy resolving models. A submerged ridge extends the latitudinal extent of the circumpolar channel. The wall across $Y = 0\,\mathrm{km}$ in blue restricts any meridional flow, thus making this a zonal reentrant channel.

In the z direction, grid spacing increases with depth from $10\,\mathrm{m}$ at the surface to $421.50\,\mathrm{m}$ in the lowest layers. At the bottom, no-slip conditions are applied as well as a linear drag coefficient. In MITgcm, no-slip boundary conditions act as an additional stress on the interior. The linear bottom drag coefficient is then set to represent additional friction that is imposed by the no-slip condition. In the eddying configuration, linear bottom drag is set so that $r_b = 1.1 \times 10^{-3}$ m/s. The bottom drag is an additional friction, set as a linear function of the mean flow above the topography. r_b is the linear bottom drag coefficient of this function, with the units m/s. (Marshall, Adcroft, et al., 1997; Marshall, Hill, et al., 1997). With this implemented, drag is cast as a linear function of the mean flow as measured above topography. Other relevant parameters are listed in Table 6.1.

This configuration is subjected to both a restoring surface temperature profile and an idealised wind stress profile. During both spin up and perturbation, the surface temperature is restored to a linear profile ranging from $0°C$ to $15°C$ every 10 days so that

$$T_{\text{surf}}(y, z = 0) = \frac{\Delta T}{L_y} y. \tag{6.1}$$

This of course makes $\Delta T = 15°C$ and $y \in [0, L_y]$, where $L_y = 2000$ km (the width of the channel). During spin up, this configuration is forced by a temporally steady wind stress profile given by

$$\tau_s(y, z = 0) = \frac{\tau_0}{2}\left[1 - \cos\left(\frac{2\pi y}{L_y}\right)\right], \tag{6.2}$$

where $\tau_0 = 0.2$ $\mathrm{N/m^2}$. For the oscillatory perturbation experiments, this wind stress profile varies with time. Spin up is 500 model years (where 1 year is 360 days) which is sufficient time for most model drift to equilibrate. The viscosity is specified by a grid-dependent lateral eddy viscosity parameter (Munday et al., 2013). This ensures that horizontal Reynolds number is $\mathcal{O}(1)$ at the grid scale, so that the viscous terms are just as large as the advective terms. This number is chosen to be 0.0125 and allows for viscosity to change as appropriate.

For this coarse configuration, GEOMETRIC is implemented into MITgcm within the GM/Redi package (Mak et al., 2018). For these experiments, GEOMETRIC is used locally in longitude and latitude so that

$$\kappa(x, y) = \alpha \frac{\int E \, \mathrm{d}z}{\int \Gamma(z) \frac{M^2}{N} \, \mathrm{d}z} \Gamma(z). \tag{6.3}$$

This is Eq.(4) from Mak et al. (2018), and uses the depth-integrated eddy energy but allows for horizontal spatial variation. $\Gamma(z)$, the non-dimensional structure function is set to be 1 everywhere. This follows from Chapter 4 Section 4.4.1, where spatial variation is introduced to κ. To maintain parameterised eddy activity and to prevent numerical instability, κ is bounded from below and above by $50\ \mathrm{m}^2/s$ and $10^4\ \mathrm{m}^2/s$ respectively. Other relevant parameters are detailed in Table 6.1.

Parameter	Value	Description
L_y	$2000\ \mathrm{km}$	meridional length
L_x	$6000\ \mathrm{km}$	zonal width
H	$5000\ \mathrm{m}$	depth
(dx, dy)	$(100\ \mathrm{km}, 100\ \mathrm{km})$	grid spacing
τ_0	$0.2\ \ \mathrm{N/m}^2$	surface wind stress magnitude
λ	$2 \times 10^{-7}\ \ s^{-1}$	eddy energy dissipation rate
α	0.1	eddy efficiency parameter
-	2×10^{-3}	Maximum (isopycnal) slope used in slope tapering
-	gkw91	Slope tapering scheme (Gerdes et al., 1991)
f_0	-1.11×10^{-4}	Coriolis parameter
ρ_0	$1028\ \ \mathrm{kg/m}^3$	reference density
r	$1.1 \times 10^{-3}\ \mathrm{m}/s$	linear bottom-drag coefficient
t_t	10 days	restoring timescale (temperature)

Table 6.1: Parameter values used in the three-dimensional GEOMETRIC model.

The experimental setup follows on from Chapter 5 in that each perturbation is run for 40 forcing oscillations, unless otherwise stated due to computational expense. The forcing oscillation experiment lengths are listed in Table 6.2.

6.2 Results on the eddy parameterised model

This configuration is spun up for 500 model years with temporally constant winds. This spin up gives total transport values of approximately $60\ \mathrm{Sv}$ and integrated total kinetic energy of $1.3\ \mathrm{m}^3/s^2$ when time averaged over the final 100 years of spin up. Transport and total kinetic energy values are lower than the values from earlier models. However, the transport values are roughly comparable between these configurations, especially given that it is common for ACC-like models to yield lower than realistically observed transport values (Youngs et al., 2019). This is not a large concern, as the physical mechanisms of the system are of interest rather than realism. Diagnostics associated with GEOMETRIC's energy budget are also computed. The depth integrated parameterised eddy energy ($\mathcal{E}$) when averaged zonally is approximately $26.17\ \mathrm{m}^3/s^2$. It is noted that within this chapter, the averaged depth integrated parameterised eddy energy is also referred to simply as "parameterised eddy energy". Likewise, the averaged eddy transfer coefficient (κ) is approximately $827\ \mathrm{m}^2/\mathrm{s}$.

Forcing	Perturbation length	Sampling period (days)
2 days	80 days	0.5
5 days	200 days	0.5
10 days	400 days	1
20 days	800 days	1
30 days	1200 days	1
60 days	2400 days	1
90 days	3600 days	5
120 days	4800 days	5
130 days	5200 days	5
140 days	15.5 years	5
150 days	16.6 years	5
180 days	20 years	5
200 days	22.2 years	5
250 days	27.7 years	5
1 year	40 years	5
2 years	80 years	10
3 years	120 years	10
4 years	160 years	10
5 years	200 years	20
6 years	240 years	20
6.6 years	264 years	20
8 years	320 years	20
12 years	480 years	20
20 years	800 years	30
40 years	720 years	40
64 years	256 years	40
128 years	256 years	40
200 years	400 years	40

Table 6.2: Table detailing the wind oscillation periods, perturbation length, and sampling period for the eddy-parameterised configuration.

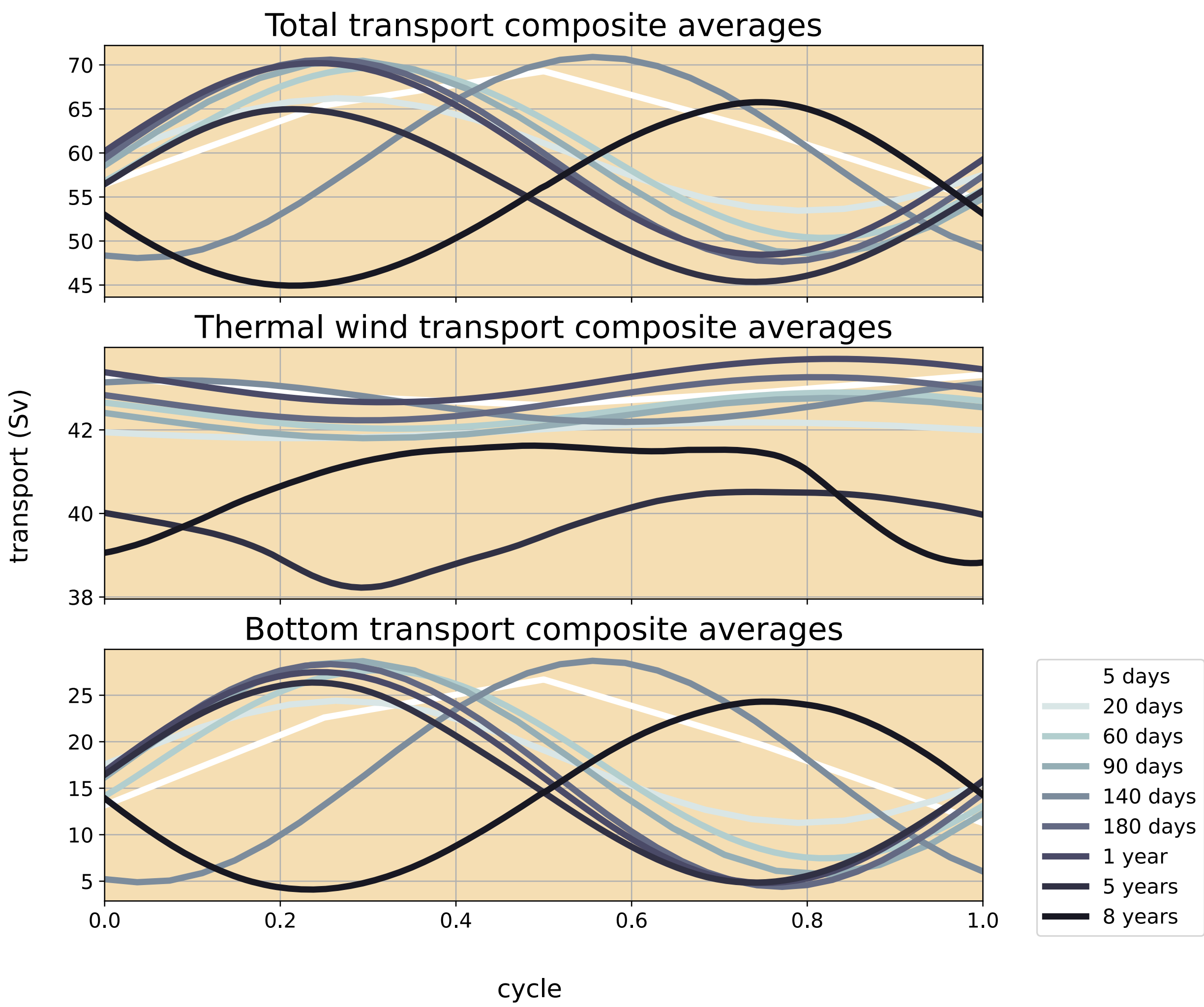

Figure 6.2: Composite averages of total, thermal wind, and bottom transport. Each composite average is plotted for one cycle of perturbation. Colours represent forcing oscillation period.

To get an idea of the behavioural trends present in the oscillatory perturbation experiments, the time dependent diagnostics are composite averaged (Sinha and Abernathey, 2016). This allows for each (averaged) cycle of data to be plotted together along the same axis in order to qualitatively see general variability and trends. This removes noise associated with inter-period variability. To compute the composite average, the data from each experiment is averaged together to compute one averaged cycle's worth of data. This is useful in giving a broad idea of the time evolution of the diagnostics. Composite averages for a selection of forcing periods are shown in Figs. 6.2 and 6.3 for transports and parameterised eddy energy, respectively. In general, the total and bottom transports follow a sinusoidal path with time, although a phase shift may be present depending upon the forcing frequency. Thermal wind transport suggests insensitivity to wind forcing on sub-annual timescales. At higher frequencies, thermal wind transport magnitudes are a few Sverdrups higher. This downward shift in thermal wind transport for the lower frequencies may be due to model drift, as well as the increasing parameterised eddy energy and variability for lower frequency forcing oscillations. The composite averages of parameterised eddy energy also suggest phase shifts at different frequencies. This is expected and investigated in more detail in the frequency domain for both transport-related and energetic diagnostics.

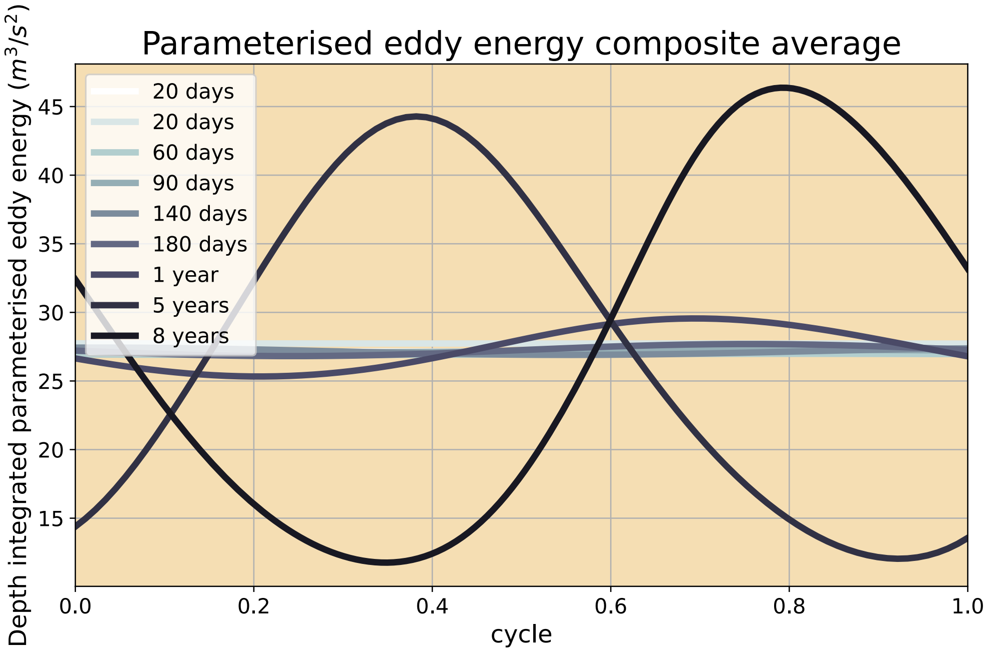

Figure 6.3: Composite average of eddy energy over one cycle of perturbation. Colours represent forcing periods.

The time averaged zonal velocity and total kinetic energy are shown for this setup in Fig. 6.4. This shows the time averaged diagnostics from the final 100 years of spin up. As expected, any eddying behaviour is smoothed out by the coarse resolution. This is a standard flow pattern for an ACC-like parameterised configuration with a bathymetric ridge. There is an energetic "hot spot" directly downstream of the ridge, which is expected and greatly influenced by the f/H contours guiding the flow.

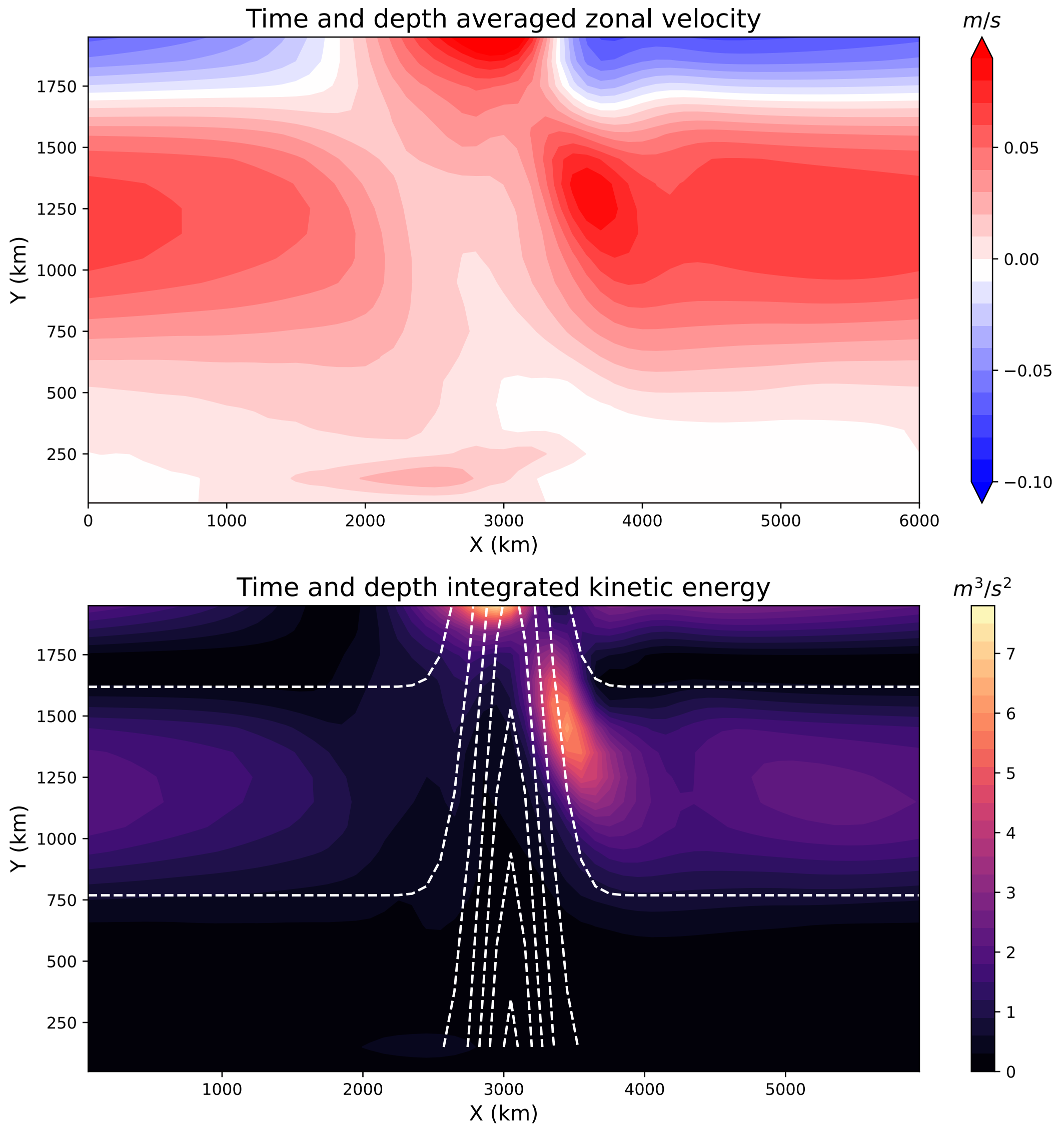

Figure 6.4: The flow structure when computed using GEOMETRIC in three-dimensions. The top panel shows time and depth averaged (over the top 725 meters) zonal velocity and the bottom panel shows time and depth integrated kinetic energy (integrated over the top 725 meters). f/H contours are overlaid (in white) on the kinetic energy.

Fig. 6.5 shows the depth integrated parameterised eddy energy. The structure of the eddy transfer coefficient, κ, follows the same spatial pattern (not shown) because κ roughly follows the parameterised eddy energy budget. Like kinetic energy and zonal velocity, the eddy energy "hot spot" is downstream of the submerged ridge. Additionally, the diagnostics follow a clear f/H contour path.

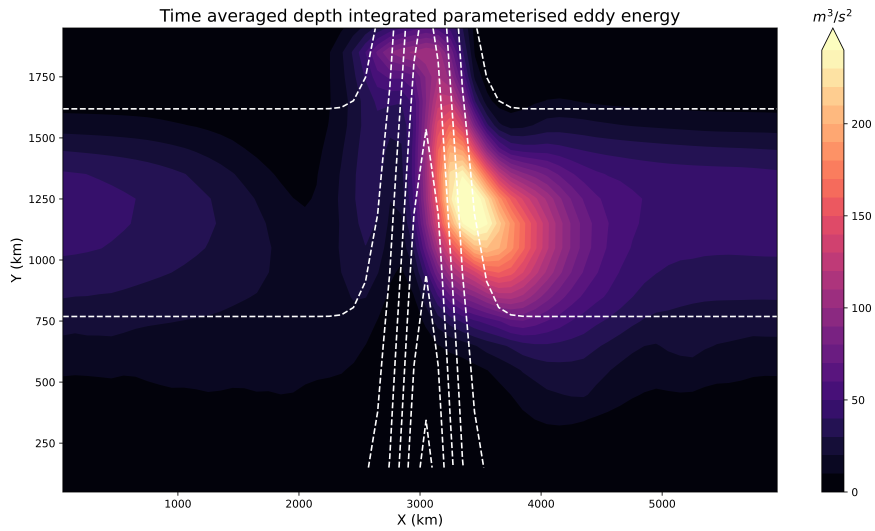

Figure 6.5: Time averaged depth integrated eddy energy in the last 100 years of spinup with GEOMETRIC, overlaid with the f/H contours in white.

It is also useful to compute the shear. Beneath the surface Ekman layer, the ACC is dominated by thermal wind balance so that,

$$\frac{\partial u_g}{\partial z} = \frac{g}{\rho_0 f}\frac{\partial \rho}{\partial y}, \tag{6.4}$$

$$\frac{\partial v_g}{\partial z} = -\frac{g}{\rho_0 f}\frac{\partial \rho}{\partial x}, \tag{6.5}$$

where (u_g, v_g) is the horizontal geostrophic velocity, g is the acceleration due to gravity, f is the Coriolis parameter, ρ_0 is a reference density, and ρ is the density (Vallis, 2006). For this model, it is useful to therefore compute the integrated quantity of geostrophic shear, $\int_{-H(x,y)}^{0} \frac{\partial u_g}{\partial z} \mathrm{d}z$. This term from hereon-out is referred to as the integrated shear. Integrated shear is of interest due to its connection to eddy energy generation. Using geostrophy, the eddy energy generation term is approximated

$$\int \alpha \frac{|f|}{N} \frac{\partial u}{\partial z} E \, \mathrm{d}z. \tag{6.6}$$

Within the eddy energy budget (see Chapter 5, Eq.(5.10) for a detailed explanation of the parameterised eddy energy budget), this term is balanced by the eddy energy dissipation. As expected from the equilibrium response, shear increases with λ, the dissipation rate, shear decreases with α, the GEOMETRIC parameter, when changes in N are assumed small. This was apparent in the lower dimensional models, and was used for transport tuning. Fig. 6.6 compares the depth integrated shear (left panel) and depth integrated parameterised eddy energy (right panel) across the final oscillation of the 6 year forcing period experiment. Both diagnostics are taken at the start of each model year for the final period of the experiment. The "hot spot" of depth integrated shear is split between two connected regions– the region at the northern most region of the submerged ridge and the region just downstream of the ridge. This is most clear in rows A, B, C, E, and F. On the other hand, the "hot spot" of depth integrated parameterised eddy energy is isolated to downstream of the ridge. Upon careful inspection, it is also noted that the "hot spots" of shear are shifted northwards in comparison to eddy energy. There are also regions of increased shear towards the meridional boundaries of the channel. Rows A to D show a decrease in both shear and eddy energy whereas rows D to F show an increase.

Fig. 6.7 compares shear with the growth rate of parameterised eddy energy. The growth rate is the ratio of the eddy energy generation to the parameterised

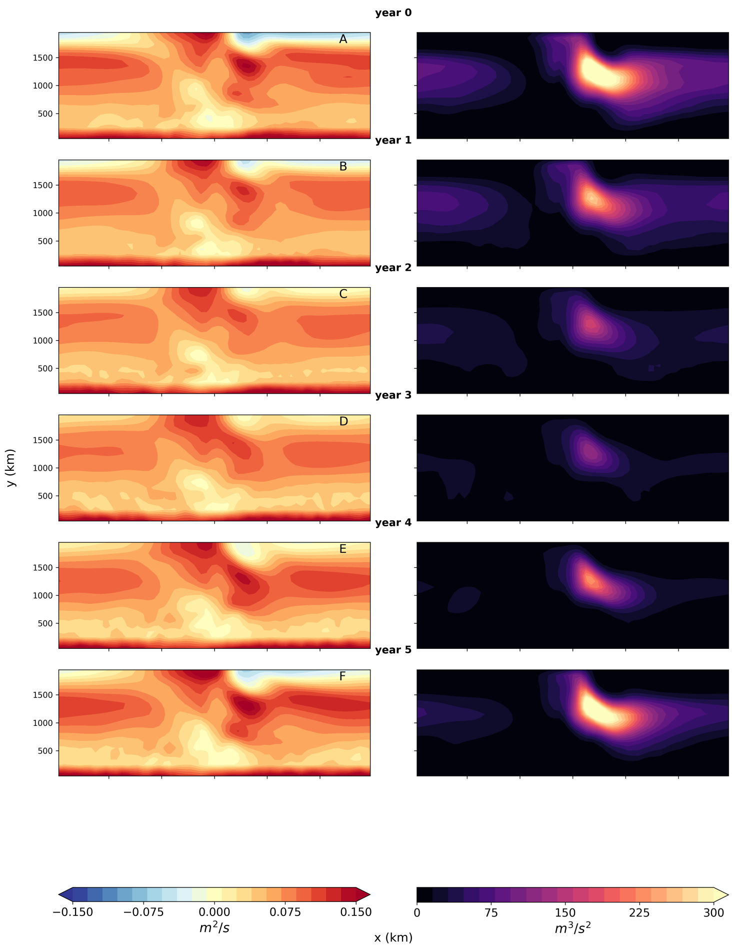

Figure 6.6: The left column shows the integrated shear and the right column shows the depth integrated eddy energy. This is taken over the final period of the 6 year forcing (time evolution is taken from top to bottom).

eddy energy. That is,

$$E_{gr}(x, y, t) = \frac{\int \alpha \frac{|f|}{N} \frac{\partial u}{\partial z} E \, \mathrm{d}z}{\int E \, \mathrm{d}z}. \tag{6.7}$$

In comparison to the parameterised eddy energy or eddy energy generation, the eddy energy growth does not extend downstream of the submerged ridge. Active areas of growth are confined on top of topographic obstacles. Figs. 6.6 and 6.7 suggest that increases in the flow and baroclinicity lead to growth in eddy energy. This then leads to a decay in flow and baroclinicity which leads to an eddy energy decay. This is in line with the oscillatory behaviour of the results in Chapters 4 and 5, as well as pre-existing literature (Ambaum and Novak, 2014; Sinha and Abernathey, 2016).

The same plots are shown for the 90 day and 128 year forcing periods. This gives examples of high and low frequency experiments. Fig. 6.8 shows the high frequency shear and parameterised eddy energy over the final 90 day period. Unlike in the 6 year example, there is no evidence for oscillatory behaviour between the growth and decay of the eddy energy and baroclinicity. Across rows A through F, both shear and parameterised eddy energy show no significant behaviour change over the forcing period. $\frac{1}{90}$ days^{-1} is considered high frequency for the Southern Ocean, hence the lack of growth/decay is not surprising.

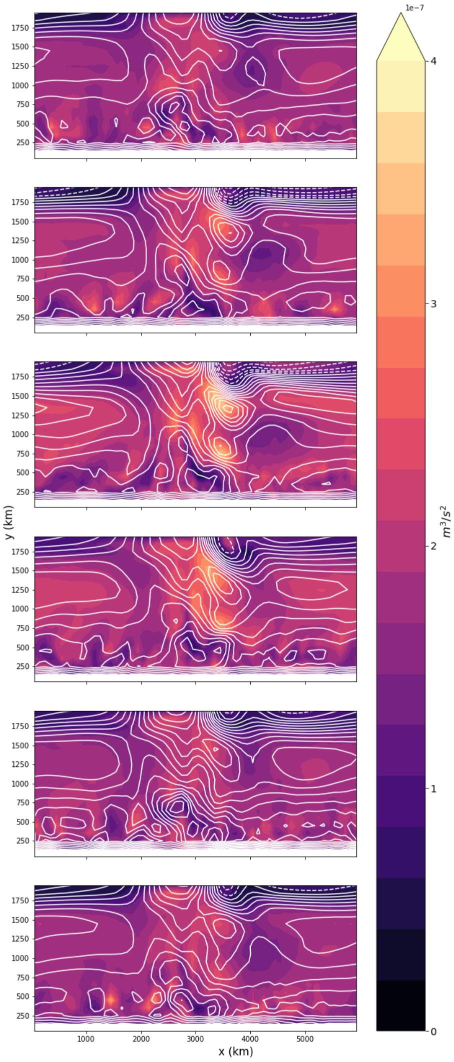

Figure 6.7: This shows the eddy energy growth (filled contour plot) with an overlay of the shear (white contours). This is also shown for the final period of the 6 year forcing perturbation, where time evolves from top to bottom.

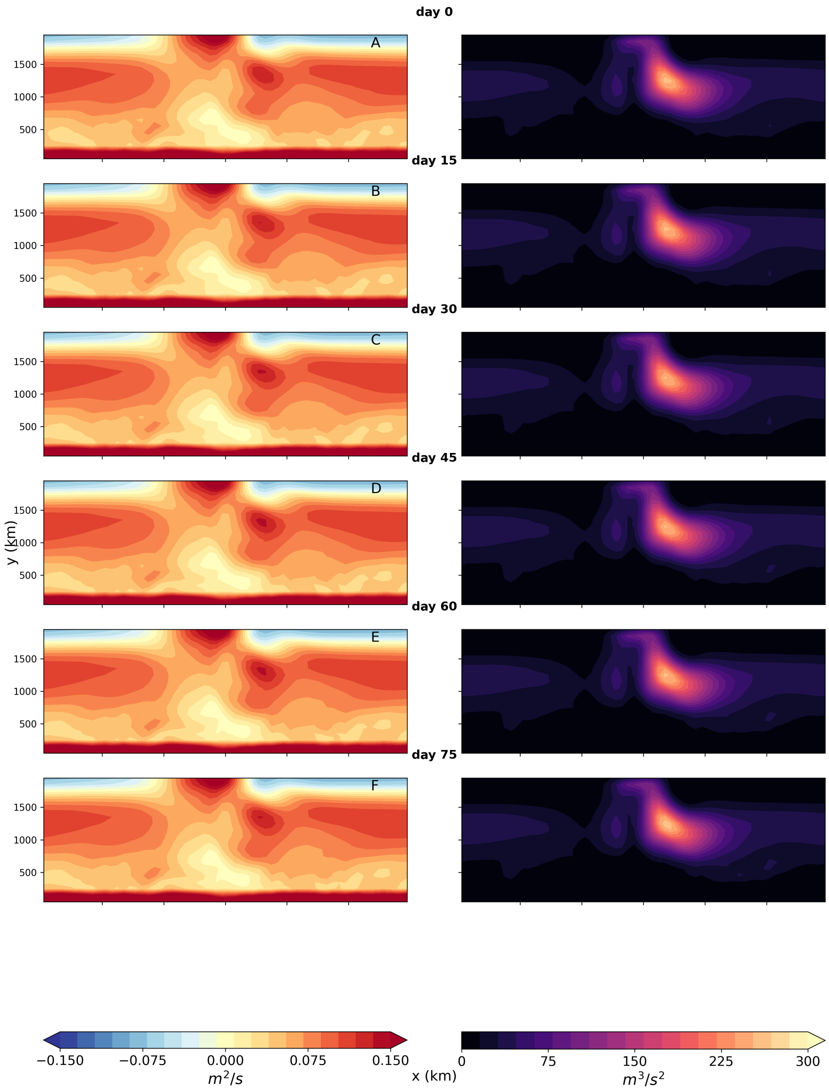

Figure 6.8: The complementary plot to Fig. 6.6 for the 90 day forcing period.

On the other side of the extreme, Fig. 6.9 shows a low frequency forcing experiment. In this figure, the rise and fall of baroclinicity and parameterised eddy energy is apparent. Panels A through C show a rise in the parameterised eddy energetics downstream of the submerged ridge. This is accompanied by a subtle south-eastward shift and increase in magnitude of the shear "hot spot" as compared to panel A. While panels A to C show the diagnostics as wind stress magnitude increases, increased wind stress is not strictly in phase with increased baroclinicity and energetics. This is discussed in Section 6.3.1. Panels D to F show the erosion of baroclinicity and parameterised eddy energetics. This is shown by the energetic "hot spot" decrease in size and magnitude. The shear "hot spot" also returns north-westward. In both high and low frequency shear diagrams, the general shape of the shear holds. That is, there are two distinct local maxima directly on top and directly downstream of the submerged ridge.

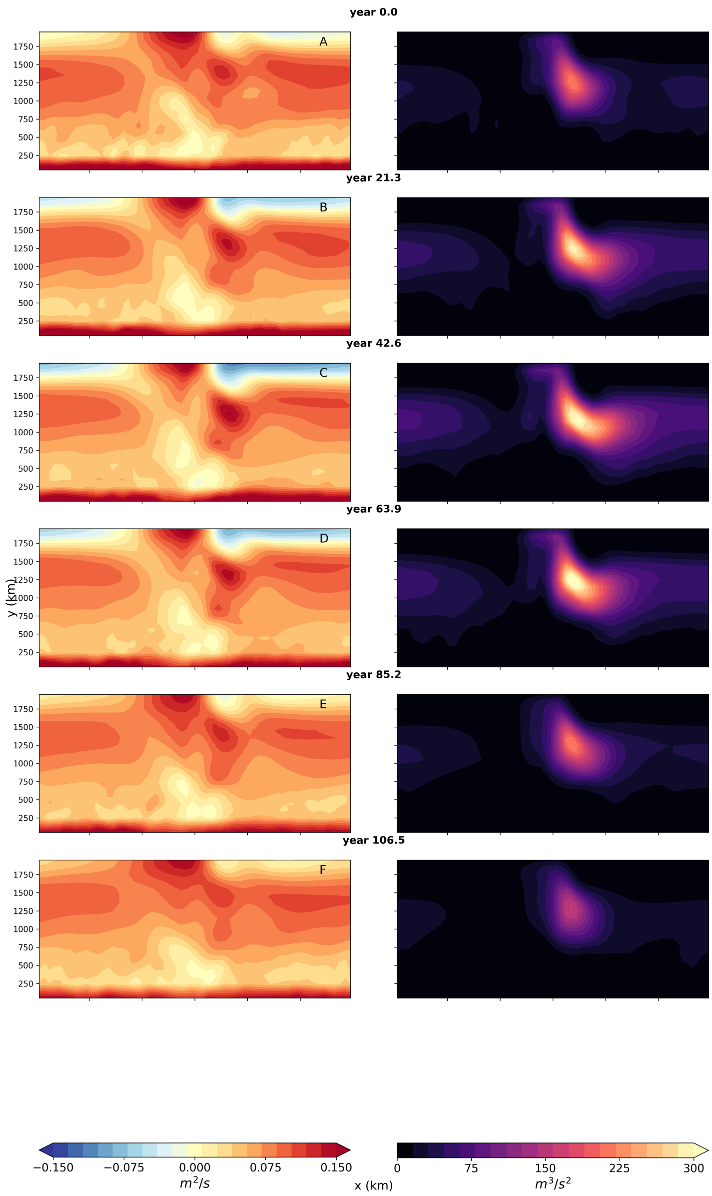

Figure 6.9: The complementary plot to Fig. 6.6 for the 128 year forcing period.

Oscillatory forcing leads to oscillating dynamics in the time domain. However, high frequency oscillation forcing leads to multiple frequency responses in thermal wind transport and parameterised eddy energy. An example of this behaviour is shown in Fig. 6.10. This shows thermal wind transport and parameterised eddy energy for the 90 day forcing period in both the time and frequency domain. While this figure only shows a single higher frequency experiment, this effect is present across frequencies where $\omega > 1\ \mathrm{year}^{-1}$. For both diagnostics, there are clear high frequency oscillations that match the forcing frequency. However, the main source of variability (in magnitude) is clearly at a lower frequency than $\frac{1}{90}\ \mathrm{days}^{-1}$. To better quantify this lower frequency oscillatory mode, the Fourier transform is computed for both de-trended diagnostics. For both thermal wind transport and parameterised eddy energy, there is a clear peak associated with the forcing frequency. This peak is noticeably smaller for the parameterised eddy energy, but is clear nonetheless. At low frequencies (the left hand side of the frequency domain), there are additional peaks in the Fourier transform of both diagnostics. The strongest peak in parameterised eddy energy correlates with $\frac{1}{6.67}\ \mathrm{years}^{-1}$. The thermal transport is similar, however, the most prominent peak is $\frac{1}{3.34}\ \mathrm{years}^{-1}$, which is a harmonic of the peak in parameterised eddy energy.

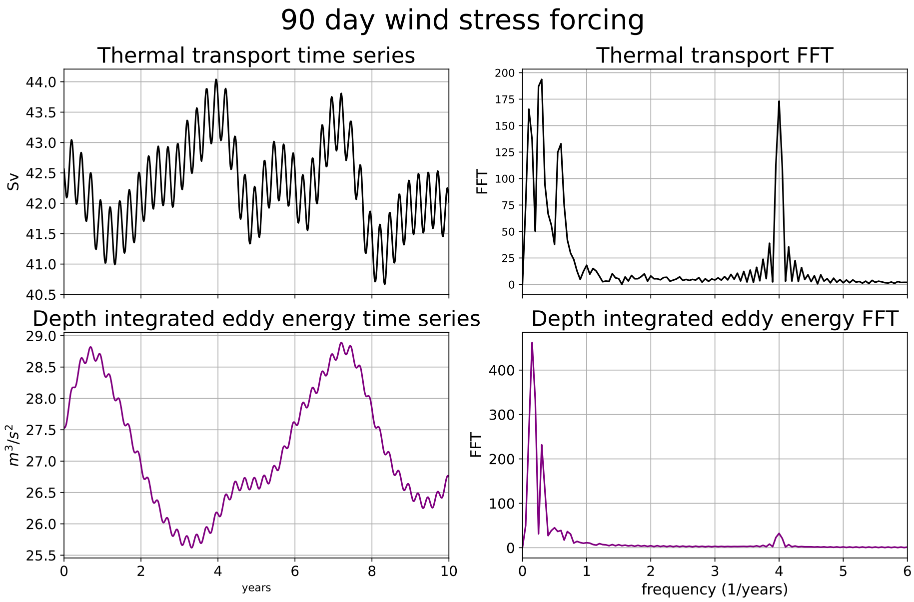

Figure 6.10: The time series and Fourier transform of thermal wind transport and eddy energy when forced with an oscillating wind stress with a 90 day period.

High frequency experiments hint towards resonance associated with oscillations with periods of approximately 6.67 years. To further investigate this, the model is forced with a windstress which oscillates at the frequency of $\omega = \frac{1}{6.66}$ years^{-1} (see Fig. 6.11). For thermal wind transport, the time series suggests high frequency variability superimposed on the prescribed forcing. In the frequency domain, this high frequency variability is confirmed by the Fourier transform of de-trended thermal wind transport. There is also evidence for significant lower frequency oscillations. The most prominent of these peaks are multiples of the forcing frequency, which comes from resonance in the system. On the other hand, the parameterised eddy energy is dominated by the forcing frequency. This is clearly shown in the Fourier transform of the de-trended diagnostic. While this signal is clear in the frequency domain, the results in the time domain indicate that this frequency may lead to resonance. This is characterised by large magnitude variation across the diagnostic of each forcing period. This behaviour was present in the dynamical system and two-dimensional model, and indicates that this is the resonant frequency associated with parameterised eddy energy. Resonant behaviour is best determined in the frequency domain, so again, response functions will be used to further explain this behaviour.

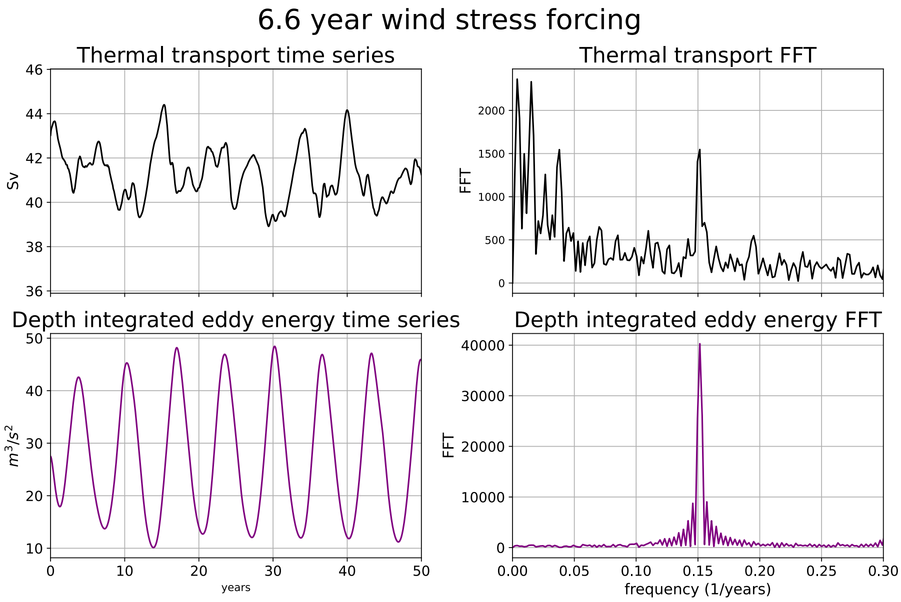

Figure 6.11: The time series and Fourier transform of thermal wind transport and eddy energy when forced with an oscillating wind stress with a 6.66 year period.

Before converting results into the frequency domain, phase portraits are first discussed (shown in Fig. 6.12). The phase portraits show the diagnostic against the peak wind stress magnitude for a selection of forcing frequencies. The two highest frequencies of the selection show approximate linearity between total and bottom transport against wind stress. Parameterised eddy energy and thermal wind transport are relatively insensitive to wind stress magnitude, with a slight negative correlation between wind stress and the diagnostics. As discussed, there is suspected energetic resonance for $P = 6.6$ years. For this forcing period, there are limit dynamics for total transport, bottom transport, and parameterised eddy energy–where the limit dynamics for parameterised eddy energy reaches peak variability for this forcing period. There is also evidence for drift or irregularity in thermal wind transport. The 12 year forcing period yields very similar results when compared to the 6.6 year forcing period. As stated, parameterised eddy energy has decreased variability. However, thermal wind transport exhibits even more drift and variability. Finally, a low frequency forcing experiment is plotted ($P = 128$ years). For this experiment, only two complete forcing oscillations were completed due to computational expense. While there is clearly some higher frequency variability within the diagnostics, each diagnostic leads to a limit dynamics. The total transport is relatively insensitive to the wind stress magnitude at these low frequencies.

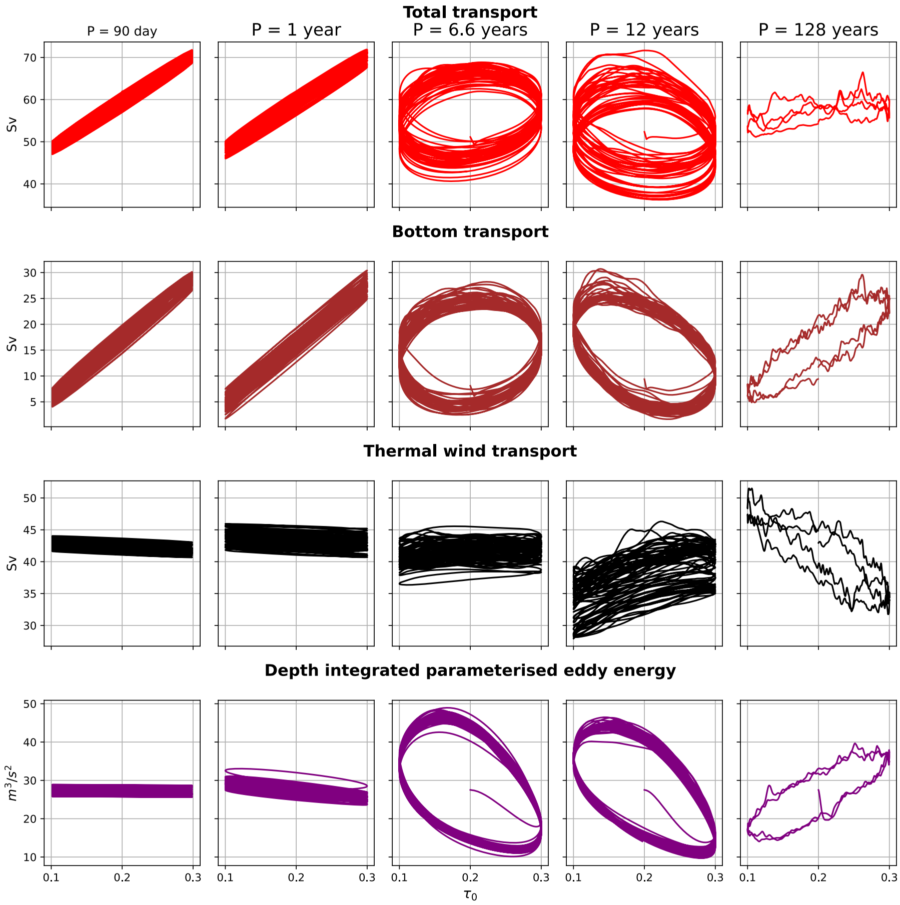

Figure 6.12: Diagnostics (total transport, bottom transport, thermal wind transport, eddy energy) against wind stress magnitude. Limit dynamics are very clear for periods greater than or equal to 6.6 years in all diagnostics but thermal wind transport. The frequency decreases from left to right. Note than the y axis is shared by row only.

Full results in the frequency domain are shown in Fig. 6.13 where results for forcing periods shorter than 20 days are not shown. The surface restoring condition leads to a spurious local peak at $\frac{1}{10}$ days^{-1}. From top to bottom, this figure shows the response function magnitudes and phase shifts of total transport, bottom transport, thermal wind transport, depth integrated and spatially averaged parameterised eddy energy, and depth integrated and spatially averaged total kinetic energy. Both response magnitudes of total and bottom transport rapidly increase to local maxima located at $\frac{1}{180}$ days^{-1} and $\frac{1}{150}$ days^{-1} respectively. These local maxima coincide with sudden phase shifts. This phase shift-local maxima pattern is shared between this GEOMETRIC configuration and the eddying configuration, as seen later in this chapter. Upon reaching this maximum, the bottom transport maintains a relatively steady response as frequency decreases. On the other hand, total transport maintains a steady response until a sudden drop at $\frac{1}{12}$ years^{-1}. It is also notable that the total and bottom transport responses are larger in magnitude than the thermal wind transport response (in particular, the bottom transport response is greatest at the tested frequencies).

Parameterised eddy energy and kinetic energy peak at lower frequencies in comparison to the transport diagnostics. Parameterised eddy energy has a peak at approximately $\frac{1}{6.66}$ years^{-1}, which approximately coincides with the predicted peak in the dynamical system and two-dimensional model. Depth integrated kinetic energy has a peak at approximately $\frac{1}{5}$ years^{-1}. Kinetic energy mimics the qualitative behaviour of the barotropic transport response magnitudes. That is, there is a rise in magnitude at high frequencies that levels off at lower frequencies. In comparison to the response magnitude of parameterised eddy energy, kinetic energy is particularly small. As seen in previous chapters, this is not surprising, as the mesoscale eddy field is more energetic than the mean flow in this region. Therefore, the energetic response curves indicate that the eddy energetics are more influential than the mean energetics. The phases of the energetic diagnostics also differ. At high frequencies, parameterised eddy energy is roughly leading the wind forcing by π, although this is subject to some variability. Phase variability at $\frac{1}{140}$ days^{-1} is the result of eddy energy dissipation inherent to the configuration. Disregarding this frequency region suggest that parameterised eddy energy leads the forcing at high frequency until about 1 years^{-1}.

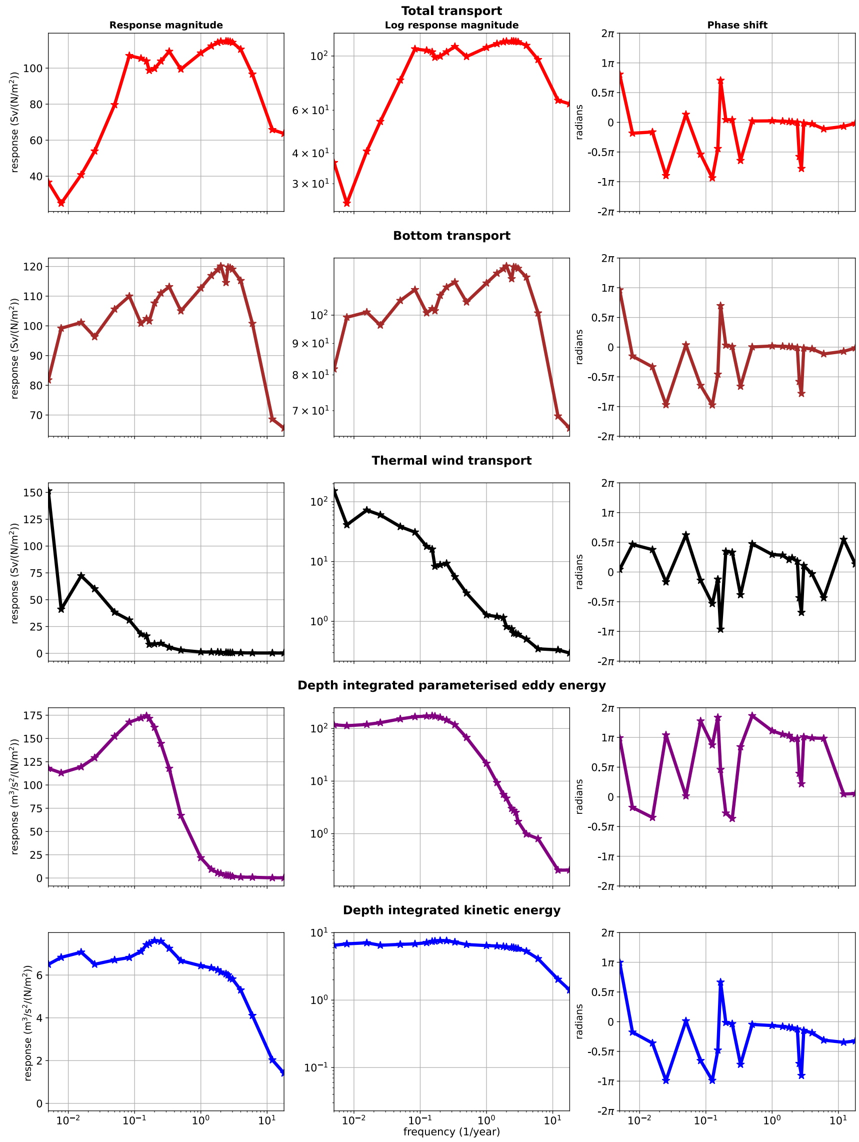

Figure 6.13: The response function (magnitude and phase shift) for total transport, bottom transport, thermal wind transport, eddy energy, and kinetic energy as computed with GEOMETRIC. From left to right, the response magnitude, the log-scaled response magnitude, and the phase response is shown.

Due to zonal variation of the mesoscale eddy field, spatially averaging can smooth over some variable dynamics. This, however, does not make much difference to the general behaviour of the response function magnitude. Rather, at energetic "hot spots"–such as directly downstream of the submerged ridge–the eddy energy response magnitude follows the averaged response, but scaled upwards (not shown). The choice of zonally averaging the parameterised eddy energy ultimately does not make any difference in understanding the physics of oscillatory eddy saturation in a parameterised three-dimensional circumpolar channel.

6.3 Discussion on the parameterised model

The ACC is insensitive to wind stress changes on equilibrated timescales. This insensitivity is not evident on transient timescales, as high frequency wind stress changes can lead to transport variability (Aoki et al., 2002; Meredith and Hogg, 2006). Analysis of the wind stress forcing experiments suggest that two distinct physical mechanisms control equilibrated and transient eddy saturation. The following hypothesis is therefore put forth: Circumpolar channel adjustment to wind stress changes is controlled by at least two different physical mechanisms. At high frequencies, barotropic processes dominate, allowing for short term sensitivity to wind stress changes. As wind stress changes shift to lower frequencies, baroclinic instability is able to take over, leading towards an eddy saturated state, as put forth in Straub (1993). This section covers the following:

1. the response of GEOMETRIC in three-dimensions to oscillatory wind stress forcing, and
2. a comparison with GEOMETRIC in three-dimensions to the dynamical system and two-dimensional model.

6.3.1 Phase

While the phase of the response is shown and briefly discussed, it is concluded that in three-dimensions the phase does not convey any important results. In particular, the phase responses in Fig. 6.13 do not suggest a clear story, especially at lower frequencies. This lack of clarity is due to depth and spatial dependency of a model in three-dimensions and computational constraints. As the oscillatory wind stress is applied to the surface, the interior ocean will respond, but at different timescales as the effect of the surface forcing propagates downwards. That is, oscillatory wind stress may not immediately affect the entire column. Furthermore, each layer is then subjected to a filtered signal from adjacent layers. Hence, variation in phase over depth leads to inconsistent phase for depth-integrated diagnostics throughout these three-dimensional model results.

Two possibilities related to this depth integrated "phase noise" are discussed. Firstly, it is possible that elements of this inconsistency with depth can be alleviated, but only with vast computational power. This variation with depth would minimise with sufficiently long compute time when compared to the forcing period. Secondly, it is possible that the depth variation of phase is due to physical processes related to stratification.

This phase-depth dependence is evident when breaking down the response function over depth. To accomplish this, a "transport per layer" diagnostic is formulated and analysed in the frequency domain.

Transport per layer is defined

$$T(z) = \int_0^{L_y} u_x(y, z)\, \mathrm{d}y \times \delta H(z), \tag{6.8}$$

where $\delta H(z)$ is the layer depth and u_x is the zonal velocity taken at $x = 6000$ km.

The response function is computed, but now as a function of both depth and frequency. Fig. 6.14 shows the response phase for a selection of frequencies over depth. The three frequencies–90 days, 12 years, and 40 years–are chosen to represent high frequency, middle frequency, and low frequency responses. The high frequency phase is relatively consistent across the entire depth. There is evidence for near surface change in the top most layers. This shows that for sufficiently high frequency forcing oscillations, the phase response at depth is consistent. As the period increases, there is more drastic change with depth. The middle and lower frequencies have significant phase change in the upper 1000 meters of the depth, which coincides with the pycnocline depth. There is then relatively consistent phase with depth for both frequencies. The middle frequency yields less significant phase change throughout the pycnocline in comparison with the low frequency phase. While this change is mathematically correct with the given data, the depth integrated result is essentially meaningless for this model.

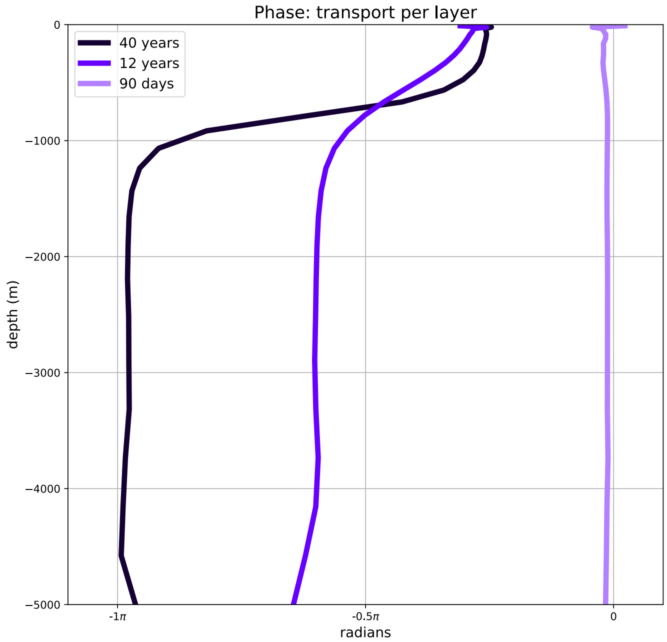

Figure 6.14: The phase with depth for transport computed at each depth level. This is shown for the 90 day, 12 year, and 40 year perturbation. The upper 1000 m shows less phase adjustment in the 12 and 40 year forcing periods.

Fig. 6.15 shows the response magnitude per layer for the same set of frequencies as Fig. 6.14. In the 90 day case, the magnitude over depth follows the solution for wave propagation through a viscous fluid. This figure illustrates the potential need for increased computational time. It is possible that the 90 day oscillatory perturbation was able to equilibrate over depth, whereas longer perturbations needed more time. It is also possible that the depth variability of phase is related to the vertical oceanic structure. The interior may be experiencing a filtered wind signal from the upper layers of the domain, particularly in the depths of the pycnocline, as suggested by the upper 1000 m of Fig. 6.14. However, this ultimately requires further investigation. Only three experiments are shown here, all of which were perturbed for forty forcing oscillations.

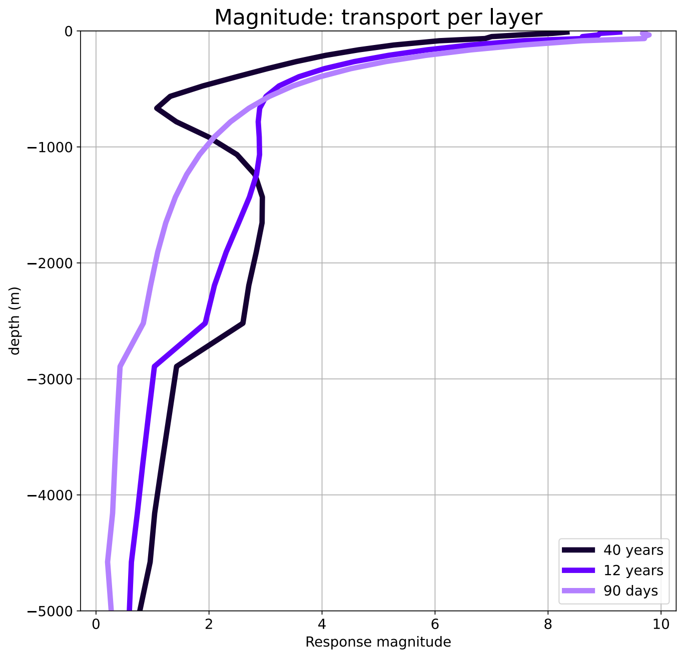

Figure 6.15: The response magnitude with depth for transport computed at each depth level. This is shown for the 90 day, 12 year, and 40 year perturbation.

This usability of the phase contrasts that found in the dynamical system and two-dimensional model. In the reduced order dynamical system, phase shifts are robust and behave in line with a standard linear oscillating system. By design, this model has no depth-dependency to consider, and is instead a coupled system with clear phase responses. The two-dimensional model also exhibits robust and interpretable phase shifts, even though there is a depth-dependent component in the model. Perhaps the lack of a third dimension and topography however is enough to maintain phase stability. It is noted that in three-dimensions, there are clear energetic "hot spots" downstream of topography–a feature clearly lacking in the zonally averaged two-dimensional model.

6.3.2 Response magnitude

While phase may not lead to meaningful conclusions, the response magnitude is fairly robust for the three-dimensional configuration. The integrated parameterised eddy energy response magnitude behaves like a linear oscillator in the frequency domain with a resonant frequency of $\frac{1}{6.6}$ years^{-1}. This timescale, $t_{3D} = 6.6$ years is an inherent oscillatory timescale associated with this model. As discussed earlier, at sufficiently high frequency, diagnostics oscillate at both the forcing frequency and approximately $1/t_{3D} = \omega_{3D}$. For frequencies higher than ω_{3D}, the parameterised eddy energy response logarithmically increases as frequency decreases towards the local maxima. Upon reaching the resonant frequency, the response peaks and then levels out towards a constant at low frequencies. This suggests that while the parameterised eddy energy has an inherent oscillatory timescale, parameterised eddy energy responds consistently to low frequency forcing. Forcing oscillations of sufficiently low frequency allow enough time for baroclinic dynamics to counteract transport changes induced by wind stresses (Meredith and Hogg, 2006; Ambaum and Novak, 2014).

The thermal wind transport response is more discontinuous than the eddy energy response. For frequencies higher than ω_{3D} thermal wind transport has no significant response. This is evident in Fig. 6.13. However, it is noted that the high frequency response does increase with forcing period, albeit with shallow slope. For frequencies lower than the resonant frequency, the thermal wind transport response increases, and suggests a local minimum located between $\frac{1}{128}$ and $\frac{1}{64}$ years^{-1} (we call this frequency ω_{GEOM}. Further tests could provide a more exact value). It is possible that with the inclusion of even lower frequencies, thermal wind transport would respond like eddy energy, but with a frequency delay. Defining baroclinic transport presents a challenge to the results. There is no single definition of baroclinic transport and using different interpretations could drastically change results. Therefore, choosing thermal wind transport to represent baroclinic transport is an assumption. Different choices could lead to different results in future work.

The total and bottom transport give information about the barotropic response of a parameterised circumpolar channel to oscillating winds. Neither diagnostic reacts to the resonant frequency, ω_{3D}. Bottom transport in particular, is directly affected by the bottom pressure gradient, which rapidly reacts to wind stress changes. In the time domain, bottom transport only oscillates at the oscillatory forcing frequency, albeit in some cases with a phase shift. Theory suggests that the phase response of bottom transport–and by extension–total transport should be zero. As discussed, this is not the case for the given number of forcing periods analysed, although at high frequencies, there is suggestion of the zero phase shift. Total transport and bottom transport follow similar behaviour patterns for frequencies greater than or equal to $\frac{1}{12}$ years^{-1}. After which, the total transport response magnitude suddenly decreases with decreasing frequency. As mentioned, both total and bottom transport response magnitudes rapidly increase to local maxima at $\frac{1}{180}$ days^{-1} and $\frac{1}{150}$ days^{-1} respectively. These frequencies are approximately equivalent within the range studied, hence this frequency is labelled $\frac{1}{t_{\mathrm{BTR}}} = \omega_{\mathrm{BTR}}$. Total and bottom transport are closely linked with Eulerian overturning. Hence, this half year timescale is postulated to be associated with resonance in overturning.

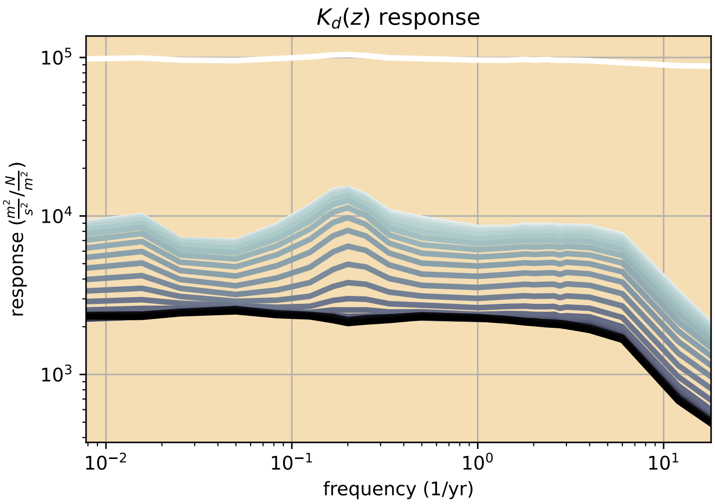

Figure 6.16: The kinetic energy response for every model layer. Light to dark colours shown surface to the deepest layer. The response magnitude is shown in the $\log$ scale.

It is interesting to further break down kinetic energy by depth level. To better understand the energetic response to oscillating wind forcing, the response functions are determined for each model layer of kinetic energy. This new diagnostic is defined:

$$\mathrm{K}_d(z,t) = \frac{1}{L_x L_y} \iint \mathrm{KE}(x,y,z)\,\mathrm{d}x\mathrm{d}y, \tag{6.9}$$

and the response function is computed following the standard procedure. The response is computed for all 30 depth layers and is shown in Fig. 6.16. From light to dark, this shows the layer dependent zonally averaged kinetic energy response from the surface to the bottom layer. Most obviously, the surface response is much greater and qualitatively different from any of the inner layers (note, this is shown in the $\log - \log$ scale). This contrast between the surface and interior model layers suggests that the interior reacts to a filtered signal from the oscillatory winds applied at the surface. Finally, the kinetic energy response scales with $\int u \cdot u \,\mathrm{d}z$.

This leads to a steady response for all but the highest forcing frequencies. The kinetic energy response can be shown over depth, and the response magnitude scales inversely with depth. This relationship does not hold for the phase, which like the other diagnostics, evolves with depth. At ω_{3D} there is a slightly elevated response in kinetic energy. This small elevation is not significant and just a small signature of the parameterised eddy field on kinetic energy.

6.4 Eddy resolving model in three-dimensions

The prior sections of this chapter focus on an eddy parameterised three-dimensional model. There are similarities with the dynamical system and two-dimensional model, such as the lower frequency peak associated with parameterised eddy energy. However, this three-dimensional model has far more internal variability and resulting noise across results in comparison with the previous models. This could be rectified with increased simulation lengths to capture a larger number of forcing oscillations, but at the expense of increased computational power. This configuration also contained a submerged ridge that guided the flow and was a source of bottom form stress. This feature was neglected in lower-dimensional models and may be a source of barotropic mechanisms. Even so, this three-dimensional model parameterised with GEOMETRIC gives greater insight into "real world" behaviour. By design, a parameterised model does not explicitly include the mesoscale eddy field. To include these effects, a high resolution three-dimensional channel model is configured. A high resolution eddy model will help determine if the resonant timescale associated with parameterised eddy energy in the previous models is apparent beyond GEOMETRIC. This model is also built using MITgcm and simulates an ACC-like channel at eddy resolving resolution.

6.4.1 Model configuration

The eddying configuration is a high resolution three-dimensional idealised ACC-like model on the β-plane. This model replicates the configuration for a parameterised circumpolar channel with topography but in high resolution. Grid resolution is 10 km $\times$ 10 km (about $\frac{1}{10}^\circ$ resolution) which is eddy resolving. This eddying reference case is similar to standard ACC-like channel configurations (e.g., Munday et al. (2013) and Mak et al. (2018)). A high resolution eddy resolving model gives insight into the "real world behaviour" of the ACC when subject to oscillatory winds. When parameterisations are used, the eddying calculations are used as a reference for physical mechanisms and behaviour (both qualitative and quantitative). Disparities between the eddying and parameterised solutions are of interest, as they illuminate missing physics (if any) which is not captured by the parameterisations.

The experimental procedure follows on from the parameterised model. A 500 year spin up with temporally steady winds is followed by a suite of experiments forced by wind stress forcing oscillations of different frequencies. The forcing perturbations are listed in Table 6.3.

6.4.2 Results

This configuration is spun up for 500 model years with temporally constant winds. This spin up gives total transport values of approximately 100 Sv and depth integrated kinetic energy of 30 $\mathrm{m}^3/\mathrm{s}^2$ when time averaged over the final 100 years of spin up. Transport and kinetic energy values are higher than the values from earlier models. In the parameterised channel model, transport is 60 Sv and depth integrated kinetic energy is 1.3 $\mathrm{m}^3/\mathrm{s}^2$. The transports are roughly comparable between these two configurations, especially given that it is common for ACC-

Forcing	Perturbation length	Sampling period (days)
2 days	80 days	0.5
5 days	200 days	0.5
10 days	400 days	1
15 days	600 days	1
20 days	800 days	1
30 days	1200 days	1
40 days	1600 days	1
60 days	2400 days	1
90 days	3600 days	5
100 days	4000 days	5
120 days	4800 days	5
140 days	5600 days	5
180 days	20 years	5
1 year	40 years	5
2 years	80 years	5
4 years	160 years	5
16 years	128 years	10
32 years	128 years	30
64 years	320 years	30
128 years	236 years	30

Table 6.3: Table detailing the wind forcing periods, experiment length, and sampling period for the eddying configuration.

like models to yield lower than realistically observed transport values (Youngs et al., 2019). The disparity between kinetic energy values however is significant. In the eddy parameterised model, most of the energy is parameterised eddy energy, which explains the seemingly low mean energy level. Even so, while transport and kinetic energy values are higher than the values given in earlier models, this is not a large concern as the physical mechanisms of the system are of interest rather than realism.

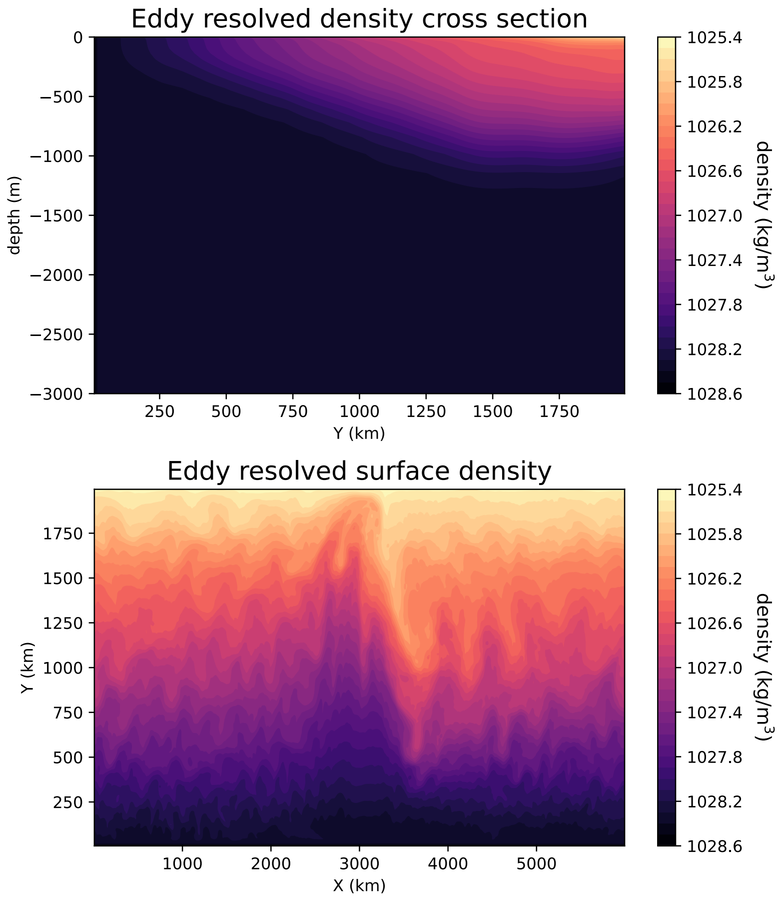

Figure 6.17: The equilibrated density structure from spin up. The cross-section is taken at the longitude furthest away from any bathymetry (top) and the surface density field (bottom).

Fig. 6.17 shows the density of the equilibrated flow before any perturbations. The cross-section is taken at a single longitude, furthest away from the submerged ridge. The upper layers (roughly the interior 1500 m, disregarding the surface layers) show the tilting isopycnals which are characteristic of ACC flow. Density is also shown at the surface. This shows how the bathymetry affects the flow, especially downstream of the ridge. The surface density shows a wavelike structure, which is strongest in the centre of the domain (approximately $Y = 1000$ km). This filament structure is due to the resolution, which explicitly resolves the mesoscale eddy field.

Fig. 6.18 shows more diagnostics of the upper ocean. Here, zonal velocity and kinetic energy are averaged in time for the last 20 years of spin up and averaged in depth over the top 725 m. Again, this is a standard flow pattern for an ACC-like configuration with a bathymetric ridge. For both diagnostics, the wavelike structure is apparent, but greatly enhanced downstream of the ridge. This is particularly clear in time averaged kinetic energy. This "hot spot" directly downstream of the ridge is expected and greatly influenced by the f/H contours guiding the flow.

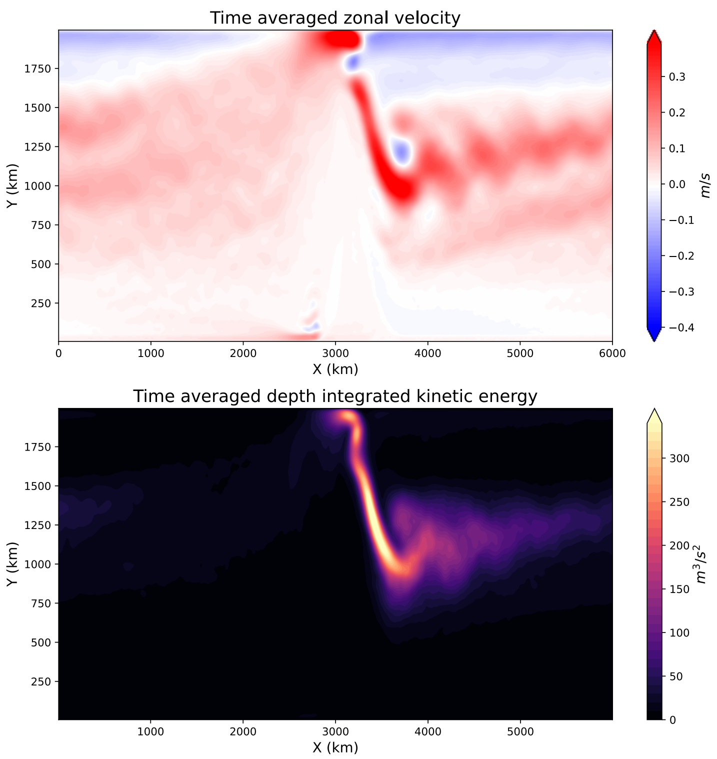

Figure 6.18: The time averaged velocity and depth integrated kinetic energy diagnostics over the final 20 years of spin up. Diagnostics are averaged in time and integrated over the top 724.7 m respectively.

Composite averages for a selection of forcing periods are shown in Fig.

6.19, Fig. 6.20, and Fig. 6.21 for total transport, thermal wind transport, and integrated kinetic energy, respectively. Total transport evolves with Eulerian overturning response and is highly correlated with bottom transport (not shown due to behavioural similarity). Transport has greater amplitude of variability for the highest and lowest frequencies. At high frequencies, this is to be expected, since there has not been time for any sort of equilibrated eddy saturation or compensation to emerge over one period. On the other hand, "mid-frequency" forcing experiments show hints of equilibration as baroclinic instability has had more time to act on the flow. At the lowest frequencies, total transport again shows greater amplitude of variability as well as a potential phase shift (although this phase shift, associated with composite averages, must be treated with great caution as discussed in Chapter 3). It is possible that at the longest periods of interest, internal variability and drift need more adjustment time. For the longest forcing periods, the full 40 forcing cycles were not carried out due to computational constraints.

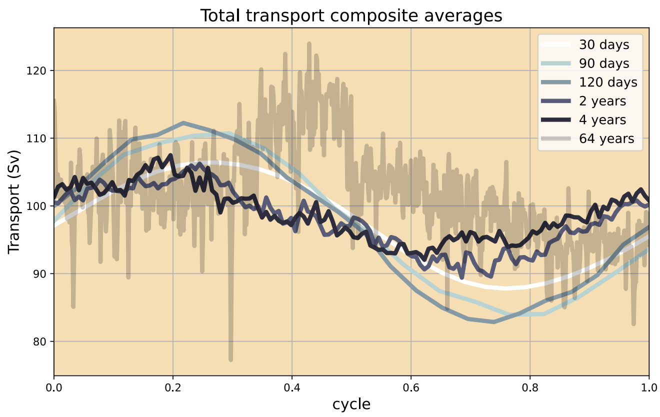

Figure 6.19: Composite averages of total transport from a sub-selection of wind forcing experiments. Colours represent different periods of forcing.

For all but the lowest frequency in the thermal wind transport composite averages, the system restores towards an eddy saturated state. Interestingly, for the 64 year forcing period, there is great variability. This may indicate a peak in response correlated with this frequency. As thermal wind transport is related to baroclinic processes (through density gradient adjustment), it is possible that the total transport (Fig. 6.19) was also exhibiting signs of the baroclinic processes. That is, if the 64 year perturbation is approaching a resonant frequency for baroclinic processes, this signature may be apparent in both thermal wind transport and total transport. These trends in composite average magnitude are also evident in Fig. 6.21. This figure shows the composite averages for the same sub-selection of wind forcing experiments for depth integrated kinetic energy. This suggests that longer forcing cycles lead to greater variability in kinetic energy, which could be an alternative explanation for the increased variability in both thermal and total transport associated with longer forcing periods.

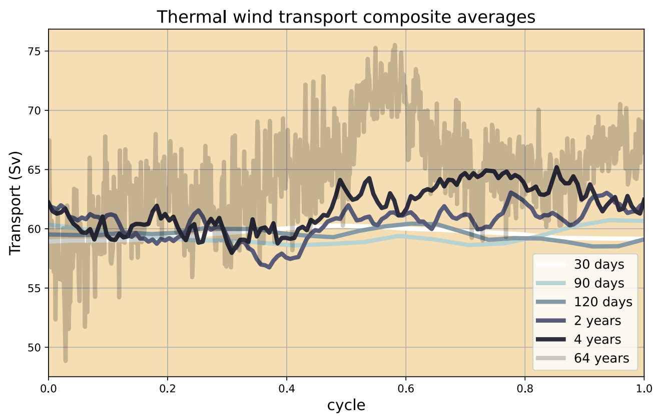

Figure 6.20: Composite averages of thermal wind transports for the same frequencies in Fig. 6.19. Colours represent different periods of forcing.

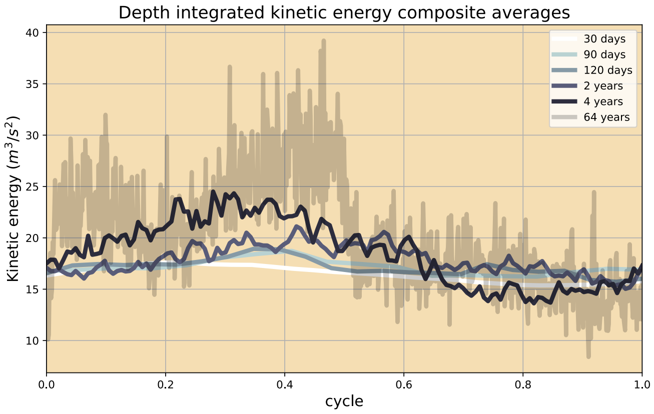

Figure 6.21: Composite averages of spatially averaged kinetic energy from the same sub-selection of wind forcing experiments in Fig. 6.19. Colours represent different forcing periods.

It is useful to also look at the raw time series of some diagnostics for a selection of forcing frequencies. In Fig. 6.22, the total and thermal wind transport for the wind forcing experiment with a 90 day period are shown for the final 2 years of perturbation. Bottom transport is not shown, as it qualitatively follows the behaviour of total transport. Even by eye, it is clear that there is a close relationship between wind stress magnitude changes and total transport evolution. This is further shown in the Fourier transform of de-trended total transport. The Fourier transform for the total transport also indicates non-zero low and high frequency components. This is reflected by the non-periodic variability of the time series. On the other hand, there is far less obvious regular oscillatory behaviour evident in thermal wind transport. This lack of periodicity at the forcing frequency is also evident in the de-trended Fourier transform, which does not point to a clear dominating frequency for this diagnostic. As mentioned, the thermal wind transport is associated with baroclinic processes, hence this result is not surprising. In the literature, there is suggestion of a lag between instantaneous forcing changes and thermal wind transport change, as time is required for the baroclinic adjustment (Meredith and Hogg, 2006). For high frequency forcing (as is the case for $P = 90$ days), it is possible that this forcing is too high frequency for any clear signals to manifest in thermal wind transport.

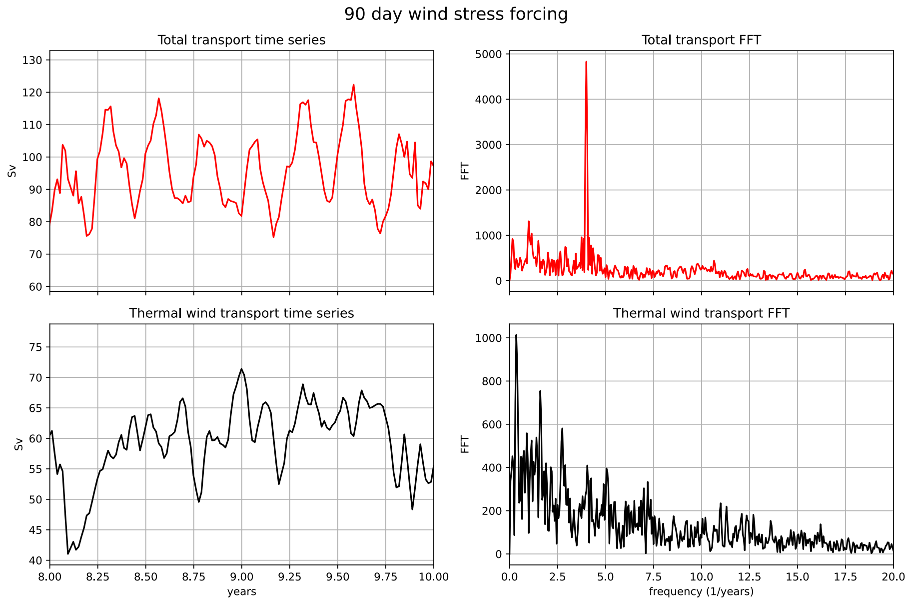

Figure 6.22: Time series (left) and Fourier transforms (right) for the total transport (top) and thermal wind transport (bottom) for the 90 day wind forcing period scenario. Data is taken from the final two years of the experiment and de-trended before the Fourier transform is computed.

The analogous plots for the $P = 16$ years experiment for the final 32 years of perturbation are shown in Fig. 6.23. In this case, both thermal wind and total transport exhibit oscillatory behaviour at the forcing frequency. This is discernible by the time series and is further proven by the Fourier transform for both de-trended diagnostics. There also is some high frequency variability associated with both diagnostics. This suggests that there is a forcing frequency somewhere between $P = 90$ days and $P = 16$ years at which thermal wind transport begins responding with the same frequency as the wind stress. This is in line with the previous discussion on the timescale of baroclinic adjustment. It is possible that $16\ \mathrm{year}$ perturbations are sufficiently long enough for a clear signal to become apparent.

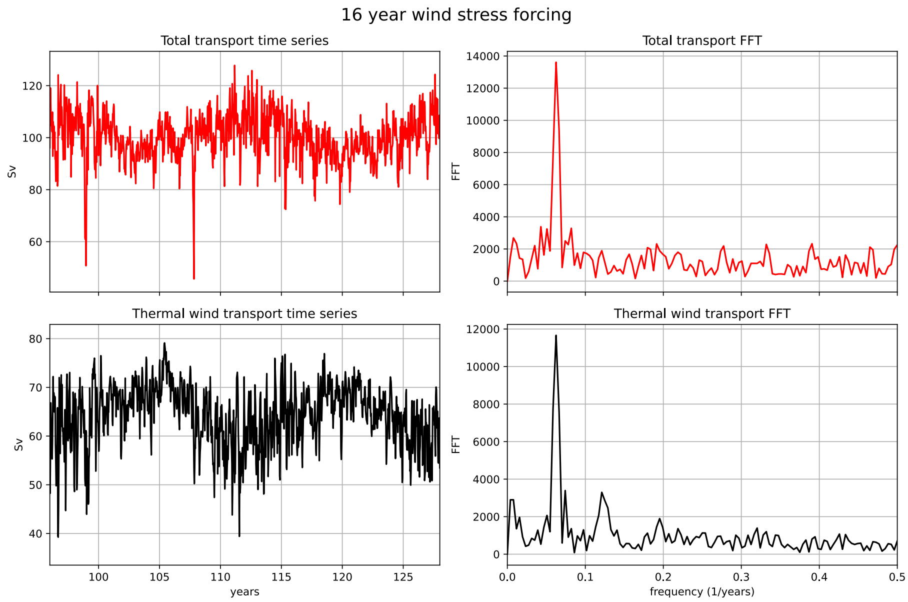

Figure 6.23: Time series (left) and Fourier transforms (right) for the total transport (top) and thermal wind transport (bottom) for the 16 year wind forcing period scenario. Data is taken from the final 32 years of perturbation and de-trended before the Fourier transform is computed.

The response functions for total, bottom, thermal wind transport, and depth integrated kinetic energy are shown in Fig. 6.24. This plot shows response magnitude in the linear and logarithmic scales (left and centre) as well as the phase shift (right). Forcing periods shown range from 2 days to 128 years (from right to left). There is a significant peak at $\frac{1}{10}\ \mathrm{days}^{-1}$ associated with total and bottom transport. This is a direct consequence of the restoring potential temperature timescale imposed on the model's top surface layer. This parameter in MITgcm sets a timescale, which in this case, is set to be 10 days. This timescale is much shorter than what is relevant to this work, and excluding such high frequencies would not be misleading in analysis. This frequency does not lead to peaks in either the depth integrated kinetic energy or thermal wind transport response magnitude. Therefore, this peak does not lead to any answers about eddy saturation, and can be safely excluded in analysis.

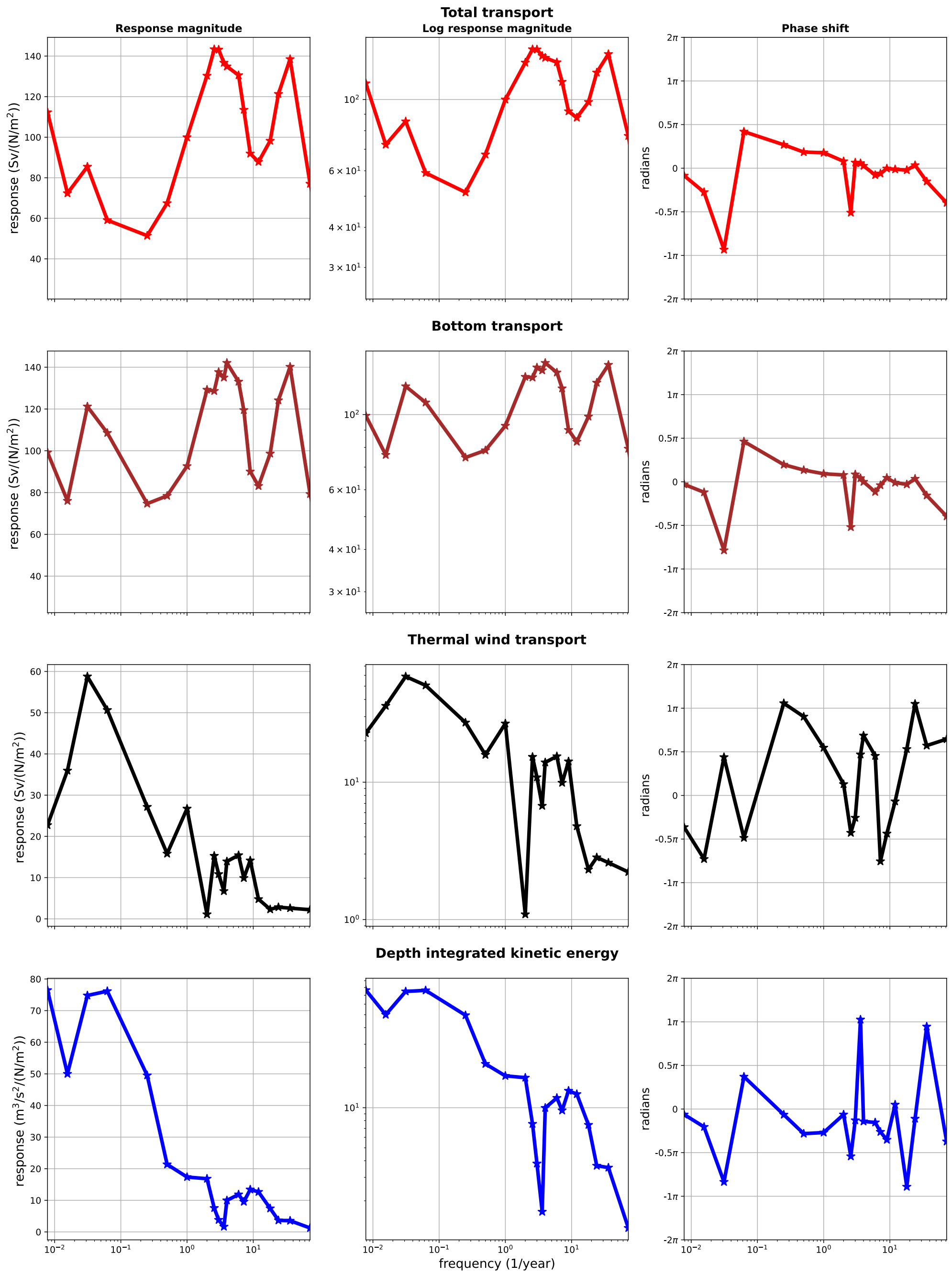

Figure 6.24: From left to right, this figure shows the response magnitude in the linear scale, the response magnitude in the logarithmic scale, and the phase shift. This is computed (top to bottom) for total transport, bottom transport, thermal wind transport, and depth integrated kinetic energy.

The total and bottom transport response functions are very similar, both in response magnitude and phase. Total and bottom transport are representative of the Eulerian overturning and barotropic responses. In overturning diagnostics (not shown), there is a prominent counterflow at all boundaries (including top, bottom, and sides). As a result, both of these diagnostics react nearly instantaneously to wind stress changes. This balance between surface and bottom stresses lines up with theory (Munk and Palmén, 1951). The second notable peak for total transport is at $\omega_{\rm tot} \approx \frac{1}{140}$ days^{-1} and for bottom transport at $\omega_{\rm b} \approx \frac{1}{90}$ days^{-1}. It is noted that response values between $\omega_{\rm b}$ and $\omega_{\rm tot}$ are roughly equivalent, forming a plateau rather than a sharp peak for both total and bottom transport. In both, there is a prominent phase shift associated with $\omega_{\rm tot}$. This coincides with the timescale associated with eddy energy damping. Following this peak, the transport response magnitudes briefly decrease as forcing frequency decreases. This inflection point suggests a shift from the transient towards equilibrated eddy saturation dynamics. This is faster than the timescale of transient eddy saturation given in Sinha and Abernathey (2016), which was determined to be 2 years in their model. The response for frequencies lower than $\omega_{\rm tot}$ and $\omega_{\rm b}$ are relatively steady.

The thermal wind transport responds differently in comparison to the total and bottom transport. Firstly, the thermal wind transport has a smaller response magnitude than the previous two response magnitudes. At high frequencies especially, any variability within the magnitude is essentially low-level noise. There is a peak in the thermal wind response magnitude at $\omega_{\rm tw} \approx \frac{1}{32}$ years^{-1}. The phase of thermal wind transport also shows a large degree of noise at high frequencies. Unlike in lower dimensional models, there is no evidence suggesting that the thermal wind transport phase lags/leads the wind stress forcing by π for frequencies higher than a resonant frequency.

Like thermal wind transport, the high frequency response of depth integrated kinetic energy is minimal with low-level noise. As seen in the logarithmic scale, the thermal wind and kinetic energy response magnitudes follow close behavioural development but with a frequency shift. The higher frequency (noise level) variability ends at $\frac{1}{6}$ years^{-1} and $\frac{1}{2}$ years^{-1} for kinetic energy and thermal wind transport respectively. Following this point, both response magnitudes grow. While it is clear that thermal wind transport reaches a peak, further experimental work would be required to fully characterise the low frequency response of kinetic energy.

The depth-dependent kinetic energy response is again shown in Fig. 6.25. Just like in Fig. 6.16, the surface response dominates in magnitude. This contrast between the surface and interior model layers suggests that the interior reacts to a filtered signal from the oscillatory winds applied at the surface.

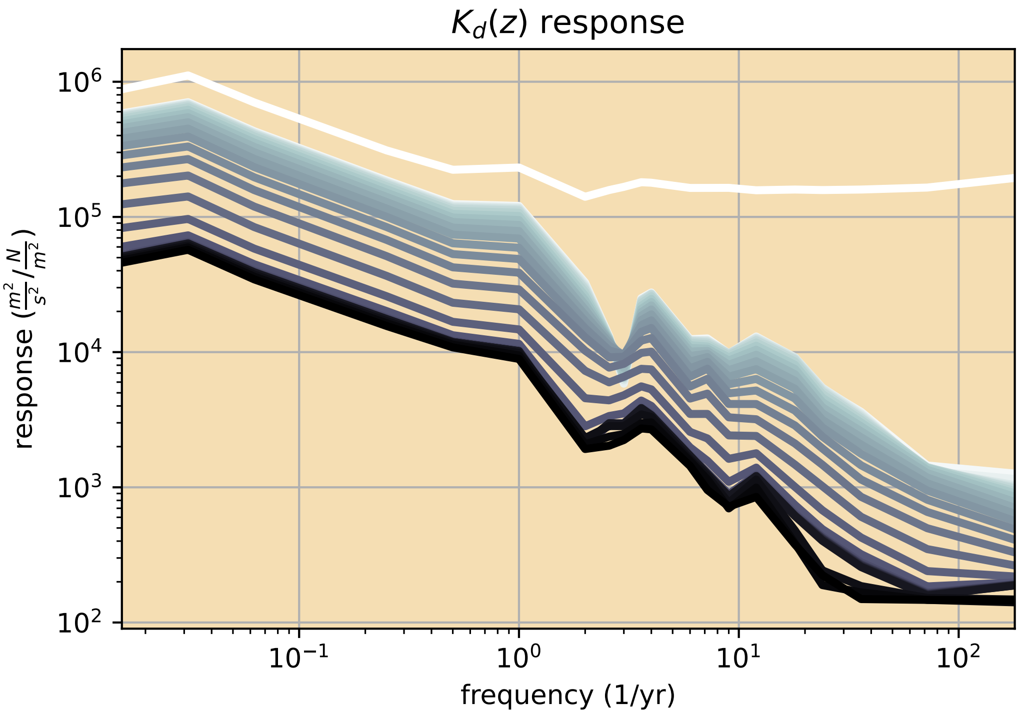

Figure 6.25: Depth dependent kinetic energy response magnitude for each model layer. Light to dark colours show surface to the deepest layer. Response magnitude is shown on the $\log$ scale.

6.4.2.1 Discussion

In this eddying circumpolar channel model, there are three significant response peaks across the transport diagnostics. In total transport, $\omega_{\text{tot}} \approx \frac{1}{140}$ days^{-1}, which coincides with a phase shift from approximately 0 to $-\pi/2$. The bottom transport also exhibits this shift at ω_{tot} even though the bottom transport has a magnitude peak at $\omega_{\text{b}} \approx \frac{1}{90}$ days^{-1}. Hence, both total and bottom transport have high frequency peaks (of approximately equivalent frequency locations within the frequency range studied. For ease of discussion, this frequency is referred to as ω_{tot}). As discussed, total and bottom transport are driven by barotropic mechanisms, such as bottom drag and form stress. These barotropic mechanisms therefore oscillate at a characteristic sub-annual timescale, set by the combined effects of bottom drag, form stress, and Eulerian overturning set by the surface wind stress at relatively high frequencies. Since total and bottom transport are associated with overturning, this may suggest timescales associated with eddy compensation, although this would require further research. Equilibrated ACC transport is essentially a balance between Ekman northward transport and eddy induced transport from baroclinic instability. Wind stress is quickly reflected in bottom form stress (barotropic mechanisms), which sets the Eulerian overturning, which in turn sets the Ekman response. After a time lag, this then is counteracted by eddy overturning, leading to eddy saturation. The sub-annual resonant timescale evident in total and bottom transport is therefore directly linked to the "fast" Ekman response in the ACC. This is reflected in total and bottom transport as the Eulerian streamfunction's rapid wind stress response is captured by the Ekman response (Stewart et al., 2021). This Eulerian-Ekman fast response also explains why the peak at ω_{tot} is not evident in thermal wind transport, as thermal wind transport is directly linked with baroclinic adjustment and is insensitive to barotropic changes.

Since this high frequency response is associated with the bottom stress response, it is heavily influenced by barotropic dynamics. This peak was not evident in lower dimension models, as these models did not account for either total or bottom transport. Instead, these lower dimension models assumed the no-flow bottom boundary condition, which the eddying and parameterised MITgcm three-dimensional channels do not assume. Hence, it is unsurprising that barotropic processes were neglected until this chapter of the hierarchy. The dynamical link between eddy saturation and eddy compensation is not yet clear in the literature. It is possible that the relationship between the barotropic and baroclinic responses link these two features of the ACC. Further understanding of this link requires a model with a basin to the north. A circumpolar channel model is not sufficient for believable overturning.

On the other hand, the peak in thermal wind transport (ω_{tw}) is associated with lower frequency processes. While there is no explicit peak in depth integrated kinetic energy, the lower frequency region ($\omega \leq \frac{1}{4}$ years^{-1}) clearly exhibits a pronounced response magnitude. This behaviour is also evident in the thermal wind response. These lower frequency processes are associated with the baroclinic response, which is responsible for equilibrated eddy saturation. It is expected that ω_{tw} marks the beginning of this baroclinic frequency region, which is associated with the dynamics of the mesoscale eddy field. After sufficient time, the mesoscale eddy field counteracts the northward Ekman flow, leading to eddy saturation (Meredith and Hogg, 2006). The response functions show what the time series and Fourier transforms suggested in Figs. 6.22 and 6.23.

Referring back to Table 6.3, wind oscillations with period greater or equal to 16 years do not complete 40 full cycles. It is likely that this does not give sufficient time for adjustment–particularly in phase. This could be rectified with a larger computational expense budget.

6.4.2.2 Conclusions

Unsurprisingly, the three-dimensional eddying model has significantly greater internal variability than the dynamical system, two-dimensional model, and eddy parameterised three-dimensional model. At such high resolution, there is explicit eddying which vastly contributes to non-linearity of the system. The response functions show at least two different processes that control the system at different frequencies. The faster of these frequencies is associated with ω_{tot} and ω_{b}. Total and bottom transport are controlled by Eulerian overturning. This suggests that barotropic processes associated with an adjustment towards eddy saturation–

and to some degree eddy compensation–dominate the system at sub-annual frequencies. The second process is associated with baroclinic processes responsible for equilibrated (standard) eddy saturation. This is the slower of the significant timescales of interest. This is timescale due to physics of the mesoscale eddy field. Time is required after wind stress perturbation for an eddying response, as there must be sufficient potential energy and sloping of the isopycnals (Straub, 1993), (Hogg and Blundell, 2006). This then leads to oscillatory dynamics linked with the depletion and generation of baroclinic instability (Ambaum and Novak, 2014).

6.5 Model comparison

The following section discusses the hierarchy of models as a whole. For convenience, Table 6.4 summarises the key results from each model.

Model	**Diagnostics**	**Peak response timescale**	**Chapter**
Dynamical system	Thermal wind transport	$t_{1D} = 9.7$ years	4
	Parameterised eddy energy	t_{1D}	
Two-dimensional	Thermal wind transport	$t_{2D} = 8$ years	5
	Parameterised eddy energy	t_{2D}	
	Depth integrated kinetic energy	t_{2D}	
Three-dimensional (GEOMETRIC)	Thermal wind transport	$t_{\text{GEOM}} = 64$ years	6
	Parameterised eddy energy	$t_{3D} = 6.6$ years	
	Total transport	$t_{\text{BTR}} = 180$ days	
	Bottom transport	t_{BTR}	
	Depth integrated kinetic energy	5 years	
Three-dimensional (Eddy resolving)	Thermal wind transport	$t_{\text{tw}} = 32$ years	6
	Total transport	$t_{\text{tot}} = 140$ days	
	Bottom transport	t_{tot}	
	Depth integrated kinetic energy	NA	

Table 6.4: A summary of key results across the hierarchy of models. Timescales associated with peaks in the response magnitude are listed, along with the corresponding diagnostic.

6.5.1 Comparison to dynamical system and two-dimensional model

Both the dynamical system and the two-dimensional model have only a single peak in response magnitude for all diagnostics. In the dynamical system, this peak is at $t_{1D} \approx 9.7$ years whereas in the two-dimensional model this peak is at $t_{2D} \approx 8$ years. For the sake of analysis, these timescales are approximately equivalent. Further model tuning could result in true equality, but is deemed unnecessary for this thesis.

Results from both three-dimensional models (eddy resolving and eddy parameterising) have peaks in the total transport response function at $\frac{1}{10}$ days^{-1}. This is a direct consequence of the surface restoring condition, hence it is not included in the dynamical system and two-dimensional model by design. Were a surface restoring condition added in either case, it is reasonable to expect this high frequency peak in total transport. This peak does not contribute to the comparative analysis, as this is purely a model artefact to maintain more realistic conditions.

The next peak at t_{BTR} is missing from both lower dimensional models. This timescale is associated with Eulerian overturning and is hypothesised to be associated with barotropic mechanisms. These dynamics are influential in three-dimensional models, but seemingly missing in models of lower dimensions. Lower dimensional models subscribe to equilibrated eddy saturation. That is, the dynamical systems use baroclinic instability rather than barotropic processes to model eddy saturation. It is possible that the bottom pressure differences have more influence on the system than previously assumed. In particular, neither lower dimensional model computes bottom transport, as it is assumed that the top and bottom stresses are equal and opposite. This effectively eliminates any quantifiable barotropic influence on the system.

Barotropic processes are dominant at high frequencies so the absence does not affect the dynamical system or two-dimensional model at low frequency. In particular, this does not seem to alter the equilibrated dynamics, as baroclinic instability mainly takes over. In both lower dimensional models, there are prominent peaks at t_{1D} and t_{2D}. In the three-dimensional GEOMETRIC configuration, there is an equivalent peak, t_{3D}, associated with baroclinic adjustment. While t_{3D} is faster than t_{1D} and t_{2D} this is most likely due to model tuning. As discussed, the three-dimensional GEOMETRIC model has much lower transport values than all other discussed models. This could be rectified by model tuning, but is deemed unnecessary for the sake of this thesis. In fact, applying Eq.(4.22) gives an oscillatory timescale of approximately $60\ \mathrm{years}$, which is not far off from the oscillatory frequency suggested by the model. This suggests that the underlying processes of thermal wind shear (transport) may be more accurately modelled at low resolution than the parameterised eddy energetics.

Because of this, it is assumed that the three peaks at ω_{1D}, ω_{2D}, and ω_{3D} all represent the response frequency associated with a shift into baroclinic instability. This result is somewhat surprising, as it verifies that the dynamical system and two-dimensional model have comparable results with higher dimensional configurations. In particular, the two-dimensional model has a zero residual mean by design, whereas the three-dimensional models do not. This design choice may impact the different behaviour between model dimension. This is reassuring, as it shows that simple models can give reasonable results, even with the liberal use of assumptions. However, this is only true for equilibrated dynamics, when baroclinic processes take over. This illuminates a gap in simplified circumpolar channel models, which often neglect crucial mechanisms, especially at high frequencies.

6.5.2 Comparison of three-dimensional models

In both the eddy resolving and eddy parameterised configurations, there are similar barotropic peaks. Using three-dimensional GEOMETRIC leads to $t_{\mathrm{BTR}} \approx 200$ days, whereas in the eddying configuration there is a prominent peak at $t_{\mathrm{tot}} \approx 140$ days. Again, there is some discrepancy between the peak numerical values but this may be rectifiable with model tuning. Even so, the physical mechanisms rather than the numerical values are of more importance for this thesis. There is a submerged ridge in both three-dimensional models with a linear bottom drag coefficient applied to the bottom layer of the configurations. In both cases, this causes bottom form drag. This is a notable difference between the lower dimensional and three-dimensional models–whether eddy resolving or eddy parameterised. It is therefore concluded that t_{BTR} and t_{tot} are directly associated with barotropic processes that are otherwise neglected in the dynamical system and two-dimensional model. The discussion on the barotropic timescale for the eddy resolving model holds for GEOMETRIC. In summary, wind stress changes across all frequencies are reflected by bottom form stress, which in turn sets Eulerian overturning and the Ekman response. Theory suggests that the ACC eddy field adjustment lags wind stress changes (Meredith and Hogg, 2006). Therefore, this fast adjustment with a sub-annual resonant frequency is associated with barotropic processes, which manifest in total and bottom transport due to form drag.

There are further shared characteristics between the two configurations in bottom transport. Fig. 6.24 shows response magnitudes of total transport, bottom transport, thermal wind transport, and depth integrated kinetic energy for the eddy resolving model. As in Fig. 6.13, for frequencies higher than $\frac{1}{300}$ days^{-1}, total and bottom transport have near identical qualitative behaviour and shared peaks.

Therefore, it is assumed that barotropic mechanisms dominate for frequencies where $\omega \geq \frac{1}{300}\,\mathrm{days}^{-1}$. Additional response functions of zonal bottom stress (not shown) also peak at this timescale, further supporting that bottom mechanisms greatly influence the barotropic and high frequency circumpolar adjustment.

The response function for thermal wind transport in three-dimensions has a substantial degree of noise in comparison to the dynamical system and two-dimensional model. Most of this noise is at higher (than the baroclinic peak) frequencies, so it is not as concerning in relation to baroclinic adjustment. GEOMETRIC in three-dimensions and the eddy resolving model have peaks associated with thermal wind transport at approximately ω_{3D} and ω_{tw} respectively. It is obvious that $\omega_{\mathrm{tw}} > \omega_{3D}$ but it is reassuring that both configurations result in a low frequency resonance of the same magnitude. In GEOMETRIC, the thermal wind transport does not behave like parameterised eddy energy, as suggested by the lower dimensional models. In three-dimensions, it is concluded that this mismatch is related to the baroclinicity generation and decay as well as the zonal mismatch of shear and parameterised eddy energy. While the eddy resolving configuration does not diagnose eddy energy, it is possible that some physical process is leading to low frequency resonance in thermal wind transport. That is, the mesoscale eddy field also grows and decays with baroclinicity.

7 | Conclusions

This chapter summarises the findings of this thesis. Further work is also outlined, with some preliminary and exploratory results shown.

7.1 Summary

Pre-existing literature on eddy saturation mainly focuses on equilibrated timescales. Within this framework, baroclinic eddy generation and erosion is the main driving force. In simple terms, increasing wind stress does not increase ACC transport, as the mesoscale eddy field grows more energetic and counteracts the effects of the wind. However, there is a notable gap in the literature when it comes to response of the ACC at non-equilibrated timescales. That is, there is a gap in understanding transient eddy saturation and adjustment. This thesis set out to accomplish the following:

1. To determine the mechanisms controlling the response of the circumpolar current to wind stress changes.
2. To compare and contrast the transient behaviour across models in multiple dimensions (dynamical system, two-dimensional, three-dimensional eddy parameterising, and three-dimensional eddy resolving) and understand the similarities and differences.
3. To analyse the effects of variable wind stress on a circumpolar current using frequency analysis techniques, which are often not used in this field.

This thesis can be summarised as follows.

A dynamical system of eddy saturation across timescales (**Chapter 4**) presented and analysed a dynamical system of eddy saturation. This model is parameterised with both GM and GEOMETRIC, with more focus on GEOMETRIC. There is an inherent oscillatory timescale/frequency associated with this model. This frequency, $\omega_{1D} = \frac{1}{9.7}$ years^{-1}, is associated with baroclinic processes of eddy saturation.

Two-dimensional model and the response to oscillatory forcing (**Chapter 5**) comprised the next step in the hierarchy of models: the two-dimensional model. This chapter extends previous two-dimensional models by including time-dependent wind stress forcing (Mak et al., 2018). Both wind stress kicks and oscillations are applied after spin up. The wind stress kicks replicate pre-existing work, however it is shown that the transient adjustment takes place within two decades of perturbation when parameterised by GEOMETRIC. The oscillatory wind stress forcing experiments are more interesting in the context of this thesis. The two-dimensional model and the dynamical system both exhibit nearly identical behaviour in the frequency domain. The resonant frequency associated with the two-dimensional model, $\omega_{2D} \approx \frac{1}{8}$ years^{-1}, is clear in both thermal wind transport and eddy energy. The two-dimensional model however suggests a damping timescale, associated with the increased width of the response peak. This is not present in the dynamical system. In both the dynamical system and the two-dimensional model, robust phase shifts at the resonant frequency are also clear. From the lower dimensional models, there is clearly a resonant frequency at least associated with idealised GEOMETRIC. This is associated with the baroclinic processes of eddy saturation, which GEOMETRIC captures. However, these models cannot capture barotropic mechanisms, hence the high frequency adjustment should be treated with caution.

Oscillatory forcing in three-dimensional models (**Chapter 6**) extends the earlier chapters of this thesis by analysing both eddy parameterising and eddy resolving three-dimensional circumpolar channel models forced by oscillatory wind stress. This comprises the final step of the hierarchy of models used to investigate the physical mechanisms of eddy saturation at multiple timescales. In the parameterised model, there are multiple resonant frequencies: ω_{BTR}, ω_{GEOM}, and ω_{3D}. It is put forth that at high frequencies, barotropic processes dominate, leading to short term sensitivity to wind stress changes (ω_{BTR}). As wind stress changes shift to lower frequencies, baroclinic instability is able to take over, leading towards emergent eddy saturation, as put forth in pre-existing literature (e.g., Straub (1993) and Marshall et al. (2017)), associated with ω_{3D}. However, ω_{3D} is only associated with the parameterised eddy energy diagnostic rather than thermal wind transport. It is concluded that the peak associated with ω_{3D} shows that the mesoscale eddy field grows and decays with baroclinicity just as thermal wind transport is assumed to do. Thermal wind transport however adjusts on longer timescales, as suggested by ω_{GEOM}, which is a lower frequency than ω_{3D}. In the eddy resolving model, there are two emergent peak frequencies, ω_{tot} and ω_{tw} (high and low frequency respectively). It is concluded that these frequencies are associated with barotropic (high frequency) and baroclinic (low frequency) mechanisms. In particular, the barotropic response is associated with the rapid change in bottom pressure gradients associated with instantaneous wind stress changes applied to the surface. After a sufficiently long adjustment, the mesoscale eddy field counteracts the wind stress changes, causing baroclinic resonance.

This thesis concludes that there are barotropic (high frequency) and baroclinic (low frequency) mechanisms that control the circumpolar current response to time-dependent wind stress forcing. It is known that bottom pressure gradients swiftly react to wind stress changes (Munk and Palmén, 1951; Marshall et al., 2017). In three-dimensional models, bottom form stress and processes associated with bottom form stress have a response peak at high frequency (ω_{tot} and ω_{BTR}). These processes are not included in the dynamical system and the two-dimensional model by design, hence there is no evidence for the corresponding barotropic response. However, lower-dimensional models and three-dimensional models do capture that resonant frequency associated with baroclinic adjustment. These timescales are detailed in Table 6.4.

Studying a circumpolar current's response to time-varying wind stress in the frequency domain is an uncommon approach in the field. As shown in this thesis, there are clear advantages in using frequency analysis. In the linear case, solutions in the frequency domain clearly and fully characterise the system's response to variable wind stress. The response functions of the reduced order dynamical system have robust magnitude and phase, which is useful in forming hypotheses about the circumpolar current's response. However, it is important not to rely too heavily on the results given through the frequency analysis methodology. As discussed, the phase shifts in three-dimensional models must be treated with caution, as the combination of depth and spatial variance prevent a consistent computation of the phase. Therefore, it is more sensible to look at phase with depth when studying three-dimensional models. Furthermore, frequency analysis is also limited by computational expense. It would be ideal to run each perturbation experiment for over 40 cycles before analysing; this is computationally unfeasible with the given resources. The longer each perturbation experiment is given to run, the clearer the results. This weakness is not a consequence of frequency analysis, and is rather a challenge presented to the field in general when running high cost experiments.

7.2 Future work

As this thesis contained a hierarchy of models, it is logical that the next step is the configuring and analysis of a more realistic ACC channel. The three-dimensional models presented in this thesis both included a submerged bathymetric ridge. Even with this ridge, these channel models are still extremely idealised. To better understand the flow through Drake Passage, the inclusion of a continental obstruction would vastly improve the understanding of the physical mechanisms associated with eddy saturation and adjustment. Preliminary work including a continental obstruction in a high resolution configuration is presented with non-trivial consequences.

7.2.1 A continental ridge

This model setup is nearly identical to the eddying model previously described. The only physical change in configuration is the addition of a continental obstruction on top of the bathymetric ridge. This obstruction begins at the northern edge of the domain and stretches southward for $L_y/2 = 1000\ \mathrm{km}$. This obstruction serves a variety of purposes. Firstly, this is more realistic for a model of Drake Passage, as the tip of South America has not yet been considered in many models. Secondly, this will cause the flow to interact more with topographical obstructions which is interesting from a physical and mathematical point of view. Because of this obstruction, a reduction is ACC transport is expected, as suggested by theory and reported in other models with a topographical block (Wang, 1994), (Munday et al., 2015).

While the relevant parameters listed in Table (6.1) still hold, the underlying physics and behaviour drastically change with the inclusion of the continental obstruction. The results of this model are currently inconclusive, but show an area of future work. Due to the f/H contours already present without this obstruction, the flow is already guided through a choke point along the bathymetric ridge. The wall essentially "compresses" the flow through a mid-longitude choke point and introduces sharp changes to the domain, as the flow cannot permeate the continental obstruction. Future work also includes introducing this continental obstruction to the parameterised configuration.

Diagnostics over the top $725\ \mathrm{m}$ and composite averages are shown in Fig. 7.1. Due to the obstruction, the flow is essentially forced to wrap as close as possible to the wall, following f/H contours. This leads to decreased kinetic energy in comparison to the previous configuration. Even with the narrow forced path, the flow has a wave-like structure downstream of the ridge. There is again an energetic "hot spot" downstream of the ridge. However, this "hot spot" is split in two, as there is an additional location at the southeast corner of the continental obstruction. This configuration also leads to a broader and more intense counterflow along the northern boundary (westward flow in this case). Composite averages are again computed for total transport and depth integrated kinetic energy for a subselection of oscillation experiments. For both diagnostics, the percent change is greater than the percent change in the configuration without a continent. That is, the time averaged diagnostics show greater sensitivity to wind stress changes. The qualitative behaviour of both, however, agree with the previously shown composite averages.

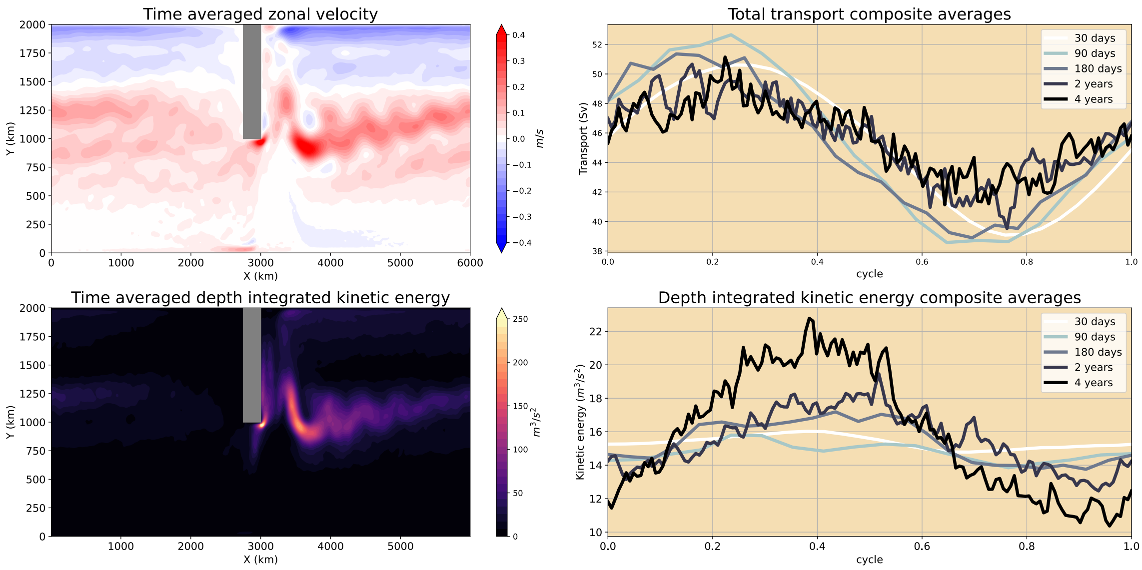

Figure 7.1: Time averaged zonal velocity and depth integrated kinetic energy over the top 725 m (left) and composite averages of total transport and depth integrated kinetic energy (right).

To fully understand the behaviour across different frequencies, the response functions for transport and kinetic energy are computed. Due to computational cost, low frequency oscillations were not computed. The response magnitudes and phases are shown in Fig. 7.2. Oscillation periods less than 20 days are excluded, as previous discussion determined that such high frequencies only showed model configuration artefacts. However, neither of the response function magnitudes have obvious peaks. There is some evidence for a peak at approximately $\frac{1}{90}\ \text{days}^{-1}$, as also suggested by the sudden phase shift but this is not significant enough to be a resonant frequency of the system. For transport, the only obvious peak is at $\frac{1}{10}\ \text{days}^{-1}$ (not shown) but this is due to the restoring condition. The integrated kinetic energy response loosely follows the same trend as the previous continent-less configuration, with the response increasing as frequency decreases. In both cases though, this relationship is not as clear as the results shown in Chapters 4 and 5. Compared to both three-dimensional responses in Chapter 6, the response function magnitude is larger in both diagnostics.

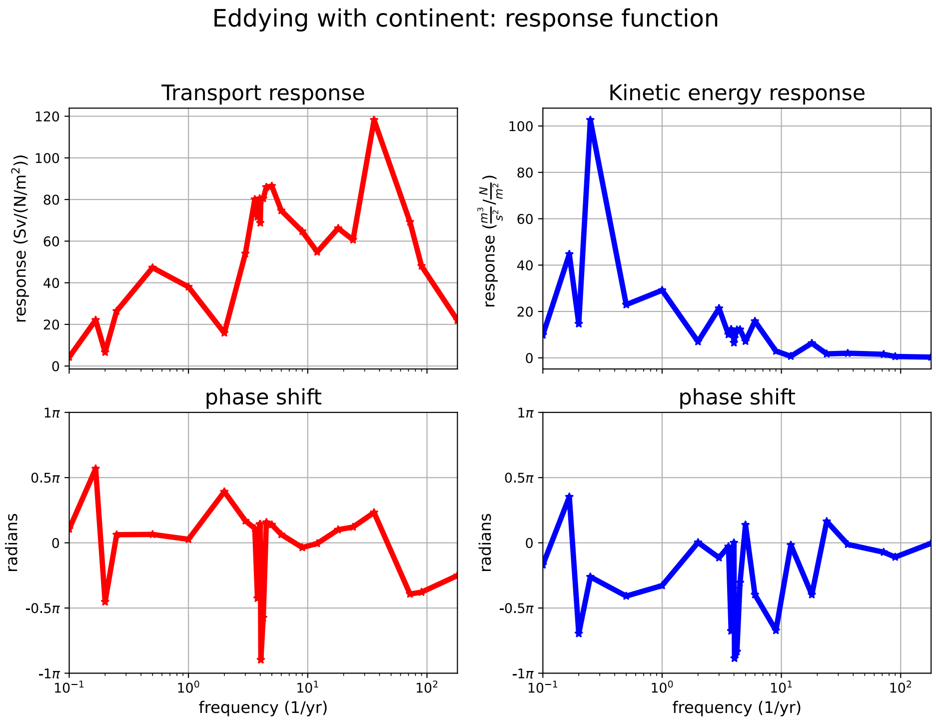

Figure 7.2: The total transport and integrated kinetic energy response functions. Frequencies higher than $\frac{1}{20}$ days^{-1} are excluded.

This experimental setup requires data from low frequency experiments. It is clear that the response functions for the configuration with the continental ridge differ from the results in Chapter 6. This shows that the inclusion of a continent is non-trivial and the dynamical response to periodic wind forcing in such a model requires further careful consideration.

7.3 Concluding remarks

Eddy saturation relies on baroclinic instability on equilibrated timescales (Straub, 1993; Munday et al., 2013; Marshall et al., 2017). The resulting insensitivity of thermal wind transport to surface wind stress changes is a defining characteristic of Antarctic Circumpolar Current dynamics. Eddy saturation is captured in high resolution models of the ACC and can be captured in parameterised models–given that the appropriate parameterisation is implemented–at equilibrated timescales (Munday et al., 2013), (Mak et al., 2018). However, the response and adjustment of a circumpolar current across different timescales is often a missing component in this discussion (Sinha and Abernathey, 2016).

In order to explore the adjustment and response across different timescales, this thesis presented a hierarchy of models forced by oscillatory wind stress at different frequencies. This thesis showed that there are both barotropic and baroclinic processes associated with circumpolar adjustment in three-dimensional models with both parameterised and explicity resolved eddies. While the barotropic processes were not evident in the dynamical system or two-dimensional model, it is reassuring that the inherent oscillatory timescale associated with GEOMETRIC from lower dimensional models persists to models of higher dimension and resolution. While there are similarities across all steps of the hierarchy, this thesis shows that models with increased dimensions and resolution lead to more opaque results. While higher dimensional results are closer to "model truths", the internal variability and inherent model drift is challenging to analyse within a reasonable computational budget. It is also clear that more realistic models (such as models with realistic bathymetry and air-sea fluxes) will have even increased complexity. It is hoped that the work in this thesis provides a starting point for fully understanding circumpolar adjustment across all timescales, and especially those timescales relevant to anthropogenic climate change. Increased understanding in this adjustment will lead to better eddy parameterisations, which will lead to better general climate models.

Bibliography

Abernathey, R., J. Marshall, and D. Ferreira (2011). "The Dependence of Southern Ocean Meridional Overturning on Wind Stress". In: *Journal of Physical Oceanography* 41(12), pp. 2261–2278. ISSN: 0022-3670.

Allison, L. C., H. L. Johnson, D. P. Marshall, and D. R. Munday (2010). "Where do winds drive the Antarctic Circumpolar Current?" In: *Geophysical Research Letters* 37(12). ISSN: 0094-8276.

Allison, L.C., H. L. Johnson, and D.P. Marshall (2011). "Spin-up and adjustment of the Antarctic Circumpolar Current and global pycnocline". In: *Journal of Marine Research* 69. ISSN: 0022-2402.

Ambaum, M. H. P. and L. Novak (2014). "A nonlinear oscillator describing storm track variability". In: *Quarterly Journal of the Royal Meteorological Society* 140(685), pp. 2680–2684. ISSN: 0035-9009.

Aoki, S., K. Shibuya, A. Masuyama, T. Ozawa, and K. Doi (2002). "Evaluation of Seasonal Sea Level Variation at Syowa Station, Antarctica, Using GPS Observations". In: *Journal of Oceanography* 58(3), pp. 519–523.

Bachman, S. and B. Fox-Kemper (2013). "Eddy parameterization challenge suite I: Eady spindown". In: *Ocean Modelling* 64, pp. 12–28.

Bachman, S., D. Marshall, J. Maddison, and J. Mak (2017). "Evaluation of a scalar eddy transport coefficient based on geometric constraints". In: *Ocean Modelling* 109, pp. 44–54.

Bai, Y., Y. Wang, and A. L. Stewart (2021). "Does Topographic Form Stress Impede Prograde Ocean Currents?" In: *Journal of Physical Oceanography* 51(8), pp. 2617–2638. ISSN: 0022-3670.

Baldocchi, D. D. and T. P. Meyers (1988). "A spectral and lag-correlation analysis of turbulence in a deciduous forest canopy". In: *Boundary-Layer Meteorology* 45(1-2), pp. 31–58. ISSN: 0006-8314.

Bishop, S. P., P. R. Gent, F. O. Bryan, A. F. Thompson, M. C. Long, and R. Abernathey (2016). "Southern Ocean Overturning Compensation in an Eddy-Resolving Climate Simulation". In: *Journal of Physical Oceanography* 46(5), pp. 1575–1592. ISSN: 0022-3670.

Blundell, S. and K. M Blundell (2010). *Concepts in thermal physics*. 2nd ed. Oxford University Press: Oxford. ISBN: 9780199562091.

Boashash, B. (2016). *Time-Frequency Signal Analysis and Processing - A Comprehensive Reference*. Elsevier: San Diego. ISBN: 0123984998.

Butcher, J. C. (2016). *Numerical methods for ordinary differential equations [electronic resource]*. Third edition. Ebook central. Chichester, West Sussex, England. ISBN: 9781119121510.

Charrassin, J. B., M. Hindell, S. Rintoul, F. Roquet, S. Sokolov, M. Biuw, D. Costa, L. Boehme, P. Lovell, R. Coleman, R. Timmermann, A. Meijers, M. Meredith, Y. H. Park, F. Bailleul, M. Goebel, Y. Tremblay, C. A. Bost, C. R. Mcmahon, I. C. Field, M. A. Fedak, and C. Guinet (2008). "Southern Ocean frontal structure and sea-ice formation rates revealed by elephant seals". In: *Proceedings of the National Academy of Sciences* 105(33), p. 11634. URL: http://www.pnas.org/content/105/33/11634.abstract.

Chidichimo, M. P., K. A. Donohue, D. R. Watts, and K. L. Tracey (2014). "Baroclinic Transport Time Series of the Antarctic Circumpolar Current Measured in Drake Passage". In: *Journal of Physical Oceanography* 44(7), pp. 1829–1853. ISSN: 0022-3670.

Constantinou, N. and A. Hogg (2019). “Eddy Saturation of the Southern Ocean: A Baroclinic Versus Barotropic Perspective”. In: *Geophysical Research Letters* 46(21), pp. 12202–12212.

Donohue, K., K. Tracey, D. Watts, M. Chidichimo, and T. Chereskin (2016). “Mean Antarctic Circumpolar Current transport measured in Drake Passage”. In: *Geophysical Research Letters* 43(22), pp. 11, 760–11, 767.

Eady, E. T. (1949). “Long Waves and Cyclone Waves”. In: *Tellus* 1(3), pp. 33–52.

Figuerola, B., A. M. Hancock, N. Bax, V. J. Cummings, R. Downey, H. J. Griffiths, J. Smith, and J. S. Stark (2021). “A Review and Meta-Analysis of Potential Impacts of Ocean Acidification on Marine Calcifiers From the Southern Ocean”. In: *Frontiers in Marine Science* 8. ISSN: 2296-7745.

Fox-Kemper, B., A. Adcroft, C. Böning, E. Chassignet, E. Curchitser, G. Danabasoglu, C. Eden, M. England, R. Gerdes, R. Greatbatch, S. Griffies, R. Hallberg, E. Hanert, P. Heimbach, H. Hewitt, C. Hill, Y. Komuro, S. Legg, J. Le Sommer, S. Masina, S. Marsland, S. Penny, F. Qiao, T. Ringler, A. M. Treguier, H. Tsujino, P. Uotila, and S. Yeager (2019). “Challenges and Prospects in Ocean Circulation Models”. In: *Frontiers in Marine Science* 6.

Frölicher, T. L., J. L. Sarmiento, D. J. Paynter, J. P. Dunne, J. P. Krasting, and M. Winton (2015). “Dominance of the Southern Ocean in Anthropogenic Carbon and Heat Uptake in CMIP5 Models”. In: *Journal of Climate* 28(2), pp. 862–886. ISSN: 0894-8755.

Gent, P. and J. McWilliams (1990). “Isopycnal Mixing in Ocean Circulation Models”. In: *Journal of Physical Oceanography* 20(1), pp. 150–155.

Gent, P., J. Willebrand, T. McDougall, and J. McWilliams (1995). “Parameterizing Eddy-Induced Tracer Transports in Ocean Circulation Models”. In: *Journal of Physical Oceanography* 25(4), pp. 463–474.

Gerdes, R., C. Köberle, and J. Willebrand (1991). "The influence of numerical advection schemes on the results of ocean general circulation models". In: *Climate Dynamics* 5(4), pp. 211–226. ISSN: 0930-7575.

Gnanadesikan, A. (1999). "A Simple Predictive Model for the Structure of the Oceanic Pycnocline". In: *Science* 283(5410), pp. 2077–2079. ISSN: 0036-8075.

Gould, J., B. Sloyan, and M. Visbeck (2013). "In Situ Observations: A Brief History, Present Status, and Future Directions". In: *Ocean Circulation and Climate: A 21st century perspective*. Elsevier Academic Press. Chap. 18.

Griffies, S. (1998). "The Gent-McWilliams skew flux". In: *Journal of Physical Oceanography* 28(5), pp. 831–841.

Hogg, A. and J. Blundell (2006). "Interdecadal variability of the southern ocean". In: *Journal of Physical Oceanography* 36(8), pp. 1626–1645.

Hogg, A., M. Meredith, D. Chambers, E. P. Abrahamsen, C. Hughes, and A. Morrison (2015). "Recent trends in the Southern Ocean eddy field". In: *Journal of Geophysical Research. Oceans* 120(1), pp. 257–267.

Howard, E., A. Hogg, S. Waterman, and D. Marshall (2015). "The Injection of Zonal Momentum by Buoyancy Forcing in a Southern Ocean Model". In: *Journal of Physical Oceanography* 45(1), pp. 259–271.

Hughes, C., P. Woodworth, M. Meredith, V. Stepanov, T. Whitworth, and A. Pyne (2003). "Coherence of Antarctic sea levels, Southern Hemisphere Annular Mode, and flow through Drake Passage". In: *Geophysical Research Letters* 30(9), 1464–n/a.

Jansen, M., A. Adcroft, R. Hallberg, and I. Held (2015). "Parameterization of eddy fluxes based on a mesoscale energy budget". In: *Ocean Modelling* 92, pp. 28–41.

Johnson, G. C. and H. L. Bryden (1989). "On the size of the Antarctic Circumpolar Current". In: *Deep-Sea Research. Part A. Oceanographic Research Papers* 36(1), pp. 39–53. ISSN: 0198-0149.

Khatiwala, S., T. Tanhua, S. Mikaloff Fletcher, M. Gerber, S. C. Doney, H. D. Graven, N. Gruber, G. A. McKinley, A. Murata, A. F. Ríos, and C. L. Sabine (2013). "Global ocean storage of anthropogenic carbon". In: *Biogeosciences* 10(4), p. 2169.

Kong, H. and M. F. Jansen (2021). "The Impact of Topography and Eddy Parameterization on the Simulated Southern Ocean Circulation Response to Changes in Surface Wind Stress". In: *Journal of Physical Oceanography* 51(3), pp. 825–843. ISSN: 0022-3670.

Le Bars, D., J. Viebahn, and H. Dijkstra (2016). "A Southern Ocean mode of multidecadal variability". In: *Geophysical Research Letters* 43(5), pp2102–2110.

Livermore, Roy, Adrian Nankivell, Graeme Eagles, and Peter Morris (2005). "Paleogene opening of Drake Passage". In: *Earth and Planetary science letters* 236(1), pp. 459–470.

Lumpkin, R. and K. Speer (2007). "Global ocean meridional overturning". In: *Journal of Physical Oceanography* 37(10), pp. 2550–2562. ISSN: 0022-3670.

Maddison, J. R., D.P. Marshall, J. Mak, and K. Maurer-Song (2023). "A two dimensional reduced order model for eddy saturation". In: in prep.

Mak, J., J. Maddison, D. Marshall, and D. Munday (2018). "Implementation of a Geometrically Informed and Energetically Constrained Mesoscale Eddy Parameterization in an Ocean Circulation Model". In: *Journal of Physical Oceanography* 48(10), pp. 2363–2382.

Mak, J., D. Marshall, J. Maddison, and S. Bachman (2017). "Emergent eddy saturation from an energy constrained eddy parameterisation". In: *Ocean Modelling* 112, pp. 125–138.

Marshall, D., J. Maddison, and P. Berloff (2012). "A Framework for Parameterizing Eddy Potential Vorticity Fluxes". In: *Journal of Physical Oceanography* 42(4), pp. 539–557.

Marshall, D. P., M. Ambaum, J. R. Maddison, D. Munday, and L. Novak (2017). "Eddy saturation and frictional control of the Antarctic Circumpolar Current: Eddy Saturation of the ACC". In: *Geophysical Research Letters* 44(1), pp. 286–292.

Marshall, J., A. Adcroft, C. Hill, L. Perelman, and C. Heisey (1997). "A finite-volume, incompressible Navier Stokes model for studies of the ocean on parallel computers". In: *Journal of Geophysical Research: Oceans* 102(C3), pp. 5753–5766.

Marshall, J., K. C. Armour, J. R. Scott, Y. Kostov, U. Hausmann, D. Ferreira, T. G. Shepherd, and C. M. Bitz (2014). "The ocean's role in polar climate change: asymmetric Arctic and Antarctic responses to greenhouse gas and ozone forcing". In: *Philosophical Transactions of the Royal Society of London. Series A: Mathematical, Physical, and Engineering Sciences* 372(2019), p. 20130040. ISSN: 1364-503X.

Marshall, J., C. Hill, L. Perelman, and A. Adcroft (1997). "Hydrostatic, quasi-hydrostatic, and nonhydrostatic ocean modeling". In: *Journal of Geophysical Research: Oceans* 102(C3), pp. 5733–5752.

Marshall, J. and K. Speer (2012). "Closure of the meridional overturning circulation through Southern Ocean upwelling". In: *Nature Geoscience* 5(3), p. 171.

Mazloff, M. R (2012). “On the Sensitivity of the Drake Passage Transport to Air-Sea Momentum Flux”. In: *Journal of Climate* 25(7), pp. 2279–2290. ISSN: 0894-8755.

Meredith, M. and A. Hogg (2006). “Circumpolar response of Southern Ocean eddy activity to a change in the Southern Annular Mode”. In: *Geophysical Research Letters* 33(16), L16608–n/a.

Meredith, M., M. Sommerkorn, S. Cassotta, C. Derksen, A. Ekaykin, A. Hollowed, G. Kofinas, A. Mackintosh, J. Melbourne-Thomas, M. Muelbert, G. Ottersen, H. Pritchard, and E. Schuur (2019). “2019: Polar Regions”. In: *IPCC Special Report on the Ocean and Cryosphere in a Changing Climate*. IPCC. Chap. 3.

Meredith, M. P, P. L Woodworth, T. K Chereskin, D. P. Marshall, L. C. Allison, G. R. Bigg, K. Donohue, K. J. Heywood, C. W. Hughes, A. Hibbert, A. M. Hogg, H. Johnson, L. Jullion, B. A. King, H. Leach, Y. D. Lenn, M. A. M. Maqueda, D. Munday, A. C. N. Garabato, C. Provost, J. B. Sallee, and J. Sprintall (2011). “Sustained Monitoring of the Southern Ocean at Drake Passage: Past Achievements and Future Priorities”. In: *Reviews of Geophysics* 49. ISSN: 8755-1209.

Meredith, M. P. (2016). “Understanding the structure of changes in the Southern Ocean eddy field”. In: *Geophysical Research Letters* 43(11), pp5829–5832. ISSN: 0094-8276.

Meredith, M. P., P. L. Woodworth, C. W. Hughes, and V. Stepanov (2004). “Changes in the ocean transport through Drake Passage during the 1980s and 1990s, forced by changes in the Southern Annular Mode”. In: *Geophysical Research Letters* 31(21), L21305–n/a. ISSN: 0094-8276.

Morrison, A. K. and A. M. Hogg (2013). “On the Relationship between Southern Ocean Overturning and ACC Transport”. In: *Journal of Physical Oceanography* 43(1), pp. 140–148. ISSN: 0022-3670.

Morrison, A. K., A. M. Hogg, and M. L. Ward (2011). “Sensitivity of the Southern Ocean overturning circulation to surface buoyancy forcing: Southern Ocean Overturning”. In: *Geophysical Research Letters* 38(14). ISSN: 0094-8276.

Munday, D., H. Johnson, and D. Marshall (2013). “Eddy Saturation of Equilibrated Circumpolar Currents”. In: *Journal of Physical Oceanography* 43(3), pp. 507–532.

Munday, D. R., H. L. Johnson, and D. P. Marshall (2015). “The role of ocean gateways in the dynamics and sensitivity to wind stress of the early Antarctic Circumpolar Current”. In: *Paleoceanography* 30(3), pp. 284–302. ISSN: 0883-8305.

Munk, W. and E. Palmén (1951). “Note on the Dynamics of the Antarctic Circumpolar Current”. In: *Tellus* 3(1), pp. 53–55.

Naveira Garabato, A., A. Williams, and S. Bacon (2014). “The three-dimensional overturning circulation of the Southern Ocean during the WOCE era”. In: *Progress in Oceanography* 120, pp. 41–78.

Nikurashin, M. and G. Vallis (2012). “A theory of the interhemispheric meridional overturning circulation and associated stratification”. In: *Journal of Physical Oceanography* 42(10), pp. 1652–1667.

Olbers, D. (1998). “Comments on "On the Obscurantist Physics of ’Form Drag’ in Theorizing about the Circumpolar Current”. In: *Journal of Physical Oceanography* 28(8), pp. 1647–1654.

Orsi, A. H. and T. III Whitworth (2005). *Hydrographic atlas of the World Ocean Circulation Experiment (WOCE): Volume 1:Southern Ocean*. International WOCE Project Office: Southampton. ISBN: 9780904175493.

Park, Y. H., T. Park, T. W. Kim, S. H. Lee, C. S. Hong, J. H. Lee, M. H. Rio, M. I. Pujol, M. Ballarotta, I. Durand, and C. Provost (2019). “Observations of the Antarctic Circumpolar Current Over the Udintsev Fracture Zone, the Narrowest Choke Point in the Southern Ocean”. In: *Journal of Geophysical Research. Oceans* 124(7), pp. 4511–4528. ISSN: 2169-9275.

Patara, L., C. W. Böning, and A. Biastoch (2016). “Variability and trends in Southern Ocean eddy activity in $1/12°$ ocean model simulations”. In: *Geophysical Research Letters* 43(9), pp. 4517–4523. ISSN: 0094-8276.

Peña-Molino, B., S. Rintoul, and M. Mazloff (2014). “Barotropic and baroclinic contributions to along-stream and across-stream transport in the Antarctic Circumpolar Current”. In: *Journal of Geophysical Research. Oceans* 119(11), pp. 8011–8028.

Poulsen, M. B., M. Jochum, and R. Nuterman (2018). “Parameterized and resolved Southern Ocean eddy compensation”. In: *Ocean Modelling* 124, pp1–15. ISSN: 1463-5003.

Qiu, B., S. Chen, P. Klein, H. Sasaki, and Y. Sasai (2014). “Seasonal Mesoscale and Submesoscale Eddy Variability along the North Pacific Subtropical Countercurrent”. In: *Journal of Physical Oceanography* 44(12), pp. 3079–3098. ISSN: 0022-3670.

Redi, M. (1982). “Oceanic Isopycnal Mixing by Coordinate Rotation”. In: *Journal of Physical Oceanography* 12(10), pp. 1154–1158.

Rintoul, S., C. Hughes, and D. J. Olbers (2001). “The Antarctic Circumpolar Current System”. In: *Ocean Circulation and Climate Observing and Modelling the Global Ocean*. Academic. Chap. 4.6.

Rintoul, S. and A. Naveira Garabato (2013). “Dynamics of the Southern Ocean Circulation”. In: *Ocean Circulation and Climate: A 21st century perspective*. Elsevier Academic Press. Chap. 18.

Rintoul, S. R, C. W Böning, M Visbeck, A Dispert, and F. U Schwarzkopf (2008). "The response of the Antarctic Circumpolar Current to recent climate change". In: *Nature Geoscience* 1(12), pp. 864–869. ISSN: 1752-0894.

Russell, J. L., I. Kamenkovich, C. Bitz, R. Ferrari, S. T. Gille, P. J. Goodman, R. Hallberg, K. Johnson, K. Khazmutdinova, I. Marinov, M. Mazloff, S. Riser, J. L. Sarmiento, K. Speer, L. D. Talley, and R. Wanninkhof (2018). "Metrics for the Evaluation of the Southern Ocean in Coupled Climate Models and Earth System Models". In: *Journal of Geophysical Research. Oceans* 123(5), pp. 3120–3143. ISSN: 2169-9275.

Screen, J., N. Gillet, D. Stevens, G. Marshall, and H. Roscoe (2009). "The Role of Eddies in the Southern Ocean Temperature Response to the Southern Annular Mode". In: *Journal of Climate* 22(3), pp. 806–818.

Scripps Institution of Oceanography (accessed 2023). *How well is Argo able to observe the global ocean?* https://argo.ucsd.edu/science/global-phenomenon/, Last accessed on 2023-04-03.

Shi, J. R., S. P. Xie, and L. D. Talley (2018). "Evolving Relative Importance of the Southern Ocean and North Atlantic in Anthropogenic Ocean Heat Uptake". In: *Journal of Climate* 31(18), pp. 7459–7479. ISSN: 0894-8755.

Sinha, A. and R. P. Abernathey (2016). "Time Scales of Southern Ocean Eddy Equilibration". In: *Journal of Physical Oceanography* 46(9), pp. 2785–2805. ISSN: 0022-3670.

Stewart, A. L., N. K. Neumann, and A. Solodoch (2023). ""Eddy" Saturation of the Antarctic Circumpolar Current by Standing Waves". In: *Journal of Physical Oceanography*. ISSN: 0022-3670.

Stewart, K. D., A. McC. Hogg, M. H. England, D. W. Waugh, and A. E. Kiss (2021). "The Ekman Streamfunction and the Eulerian and Residual Overturning Circulations of the Southern Ocean". In: *Geophysical Research Letters* 48(17). ISSN: 0094-8276.

Straub, D. (1993). "On the Transport and Angular Momentum Balance of Channel Models of the Antarctic Circumpolar Current". In: *Journal of Physical Oceanography* 23(4), pp. 776–782.

Swart, N. C. and J. C. Fyfe (2012). "Observed and simulated changes in the Southern Hemisphere surface westerly wind-stress". In: *Geophysical Research Letters* 39(16), n/a. ISSN: 0094-8276.

Swart, N. C., J. C. Fyfe, N. Gillett, and G. J. Marshall (2015). "Comparing Trends in the Southern Annular Mode and Surface Westerly Jet". In: *Journal of Climate* 28(22), pp. 8840–8859. ISSN: 0894-8755.

Swart, N. C., S. T. Gille, J. C. Fyfe, and N. P. Gillett (2018). "Recent Southern Ocean warming and freshening driven by greenhouse gas emissions and ozone depletion". In: *Nature Geoscience* 11(11), pp. 836–841. ISSN: 1752-0894.

Thompson, A. and A. Naveira Garabato (2014). "Equilibration of the Antarctic Circumpolar Current by Standing Meanders". In: *Journal of Physical Oceanography* 44(7), pp. 1811–1828.

Toggweiler, J. R and H. Bjornsson (2000). "Drake Passage and palaeoclimate". In: *Journal of Quaternary Science* 15(4), pp. 319–328.

Vallis, G. K. (2006). *Atmospheric and oceanic fluid dynamics: fundamentals and large-scale circulation*. Cambridge University Press: Cambridge.

Vaughan, D. G., G. J. Marshall, W. M. Connolley, C. Parkinson, R. Mulvaney, D. A. Hodgson, J. C. King, C. J. Pudsey, and J. Turner (2003). "Recent rapid regional climate warming on the Antarctic Peninsula". In: *Climatic Change* 60(3), pp. 243–274. ISSN: 0165-0009.

Wang, Y. (1994). “A linear homogeneous model for topographic control of the Antarctic Circumpolar Current”. In: *Journal of Marine Research* 52(4), pp. 649–685.

Williams, R. and M. Follows (2011). *Ocean dynamics and the carbon cycle: principles and mechanisms*. Cambridge University Press: Cambridge.

Wunsch, C. (2015). *Modern observational physical oceanography: understanding the global ocean*. Princeton. ISBN: 9780691158822 (hardback).

Xu, X., E. P. Chassignet, Y. L. Firing, and K. Donohue (2020). “Antarctic Circumpolar Current Transport Through Drake Passage: What Can We Learn From Comparing High-Resolution Model Results to Observations?” In: *Journal of Geophysical Research. Oceans* 125(7), n/a. ISSN: 2169-9275.

Young, W (2012). “An Exact Thickness-Weighted Average Formulation of the Boussinesq Equations”. In: *Journal of Physical Oceanography* 42(5), pp. 692–707.

Youngs, M., G. Flierl, and R. Ferrari (2019). “Role of Residual Overturning for the Sensitivity of Southern Ocean Isopycnal Slopes to Changes in Wind Forcing”. In: *Journal of Physical Oceanography* 49(11), pp. 2867–2881.

Youngs, M., A. Thompson, A. Lazar, and K. Richards (2017). “ACC Meanders, Energy Transfer, and Mixed Barotropic-Baroclinic Instability”. In: *Journal of Physical Oceanography* 47(6), pp. 1291–1305.

Zika, J., J. Le Sommer, C. Dufour, A. Naveira Garabato, and A. Blaker (2013). “Acceleration of the Antarctic Circumpolar Current by Wind Stress along the Coast of Antarctica”. In: *Journal of Physical Oceanography* 43(12), pp. 2772–2784.